



HAL
open science

Electrolyzer and Catalyst Engineering for Acidic CO₂ Reduction

Alessandro Perazio

► **To cite this version:**

Alessandro Perazio. Electrolyzer and Catalyst Engineering for Acidic CO₂ Reduction. Catalysis. Sorbonne Université, 2023. English. NNT : 2023SORUS438 . tel-04515342

HAL Id: tel-04515342

<https://theses.hal.science/tel-04515342>

Submitted on 21 Mar 2024

HAL is a multi-disciplinary open access archive for the deposit and dissemination of scientific research documents, whether they are published or not. The documents may come from teaching and research institutions in France or abroad, or from public or private research centers.

L'archive ouverte pluridisciplinaire **HAL**, est destinée au dépôt et à la diffusion de documents scientifiques de niveau recherche, publiés ou non, émanant des établissements d'enseignement et de recherche français ou étrangers, des laboratoires publics ou privés.



Sorbonne Université

Ecole doctorale 406 – Chimie Moléculaire Paris Centre

Laboratoire de Chimie de Processus Biologiques
CNRS UMR 8229 - Collège de France

Electrolyzer and Catalyst Engineering for Acidic CO₂ Reduction

Par Alessandro Perazio

Thèse de Doctorat de Chimie

Dirigée par Professeur Marc Fontecave

Présentée et soutenue publiquement le 18 décembre 2023 à Paris

Devant un jury composé de :

Pr Franck Launay, Sorbonne Université	Président
Dr Christine Cachet-Vivier, Université de Paris-Est Créteil	Rapporteuse
Dr Corinne Lagrost, Université de Rennes	Rapporteuse
Dr David Portehault, Sorbonne Université	Examineur
Dr Charles Creissen, Keele University	Examineur
Pr Marc Fontecave, Collège de France	Directeur de thèse

*Non ci si deve arrendere alla materia incomprensibile,
non ci si deve sedere.*

Primo Levi

Acknowledgements

First, I would like to thank Prof. Marc Fontecave, my thesis director, for giving me the opportunity to work at the Laboratoire de Chimie de Processus Biologiques. Despite his busy schedule, he always found the time to have regular meetings, which prompted valuable discussions with insights that greatly enriched the research project. His support and encouragement, along with the relaxed atmosphere of the lab, have been instrumental in the success of my work.

My sincerest thanks go to Charlie, without whom I could have not come this far. More than just a colleague, Charlie guided me through the complicated journey of the PhD with his incredible knowledge and friendliness. When he left to start his own group, in the middle of my second year, I thought that my academic career was going to plummet. Instead, Charlie kept supporting and motivating me, always ready to answer the most desperate questions. His mentorship has shaped me as a chemist and helped me achieve significant milestones.

I also want to thank Moritz Schreiber for offering a valuable industrial perspective to the project, a reminder to always consider the applicability of academic research.

I have had the pleasure to share three years with amazing colleagues and friends. Yutzil, Amanda, Phong, Florian, Greta, Ellie, Maria, Silvia, Youven, Hongmei, Diep, Iulia, Paolo, Sam, Francesc, Raphael, Hamid, Dilan, Adèle, Guillermo, Jessica, Johnny, Bruno, Yun and Philippe made the days more pleasant. Thank you for the daily trips to the canteen and the long chats at lunch. In particular, I thank Ellie and Huan for the fruitful collaboration.

My gratitude also goes to the incredible friends that I have made during this period. Jessica, Travis, David, Esther, Cameron, Cristian, Marie, Rafael, Gigi, Raphael, Marco and Idann, with whom I made everlasting memories and had a lot of fun. A special thanks to Sophie, who helped with the thesis revision.

Even though I moved 600 km away, when I go back home to see my old friends it feels like not a day has gone by. Edoardo, Alessandra, Marta, Francesco, Sara, Laura, Lorenzo, Anna, Annalisa e Davide, thank you for always being there.

A heartfelt thank you goes to Jan. I do not think that I could have gotten to this point without his constant affection and support. Thank you for being a fundamental presence in my life.

My family has always given me the encouragement and support that I needed, for which I consider myself very lucky. I would like to thank my uncle and aunts Piero, Lorella, and Osanna, my cousins Daniele, Elisa, Silvia, Edoardo and Licia, my grandmothers Antonietta and Gina. A special thought goes to grandfather Rigo, who is now deeply missed.

Finally, I thank my parents and sister, Katia, Fulvio and Arianna, whose love was fundamental to get through these challenging years and arrive where I am now.

Contents

1	Introduction	1
1.1	Energy crisis.....	1
1.2	CO ₂ electroreduction	6
1.2.1	CO ₂ R products	6
1.2.2	Electrocatalysis	7
1.2.3	Reactions on Cu.....	11
1.2.4	Oxygen evolution reaction	15
1.2.5	CO ₂ R parameters.....	16
1.3	CO ₂ R electrolyzer.....	16
1.3.1	Membranes	20
1.4	Local environment.....	22
1.4.1	Electrode/electrolyte interface	22
1.4.2	Current density effects	23
1.4.3	Electrolyte and pH effects	25
1.5	Commercial CO ₂ conversion	27
1.5.1	Industrial requirements.....	27
1.5.2	Prototype systems.....	28

1.6	Aim of the thesis.....	28
2	CO₂ Recycling from Carbonate	31
2.1	Introduction	31
2.2	Results	35
2.2.1	Catalyst synthesis and characterization.....	36
2.2.2	Catholyte selection.....	37
2.2.3	Single-pass conversion	40
2.2.4	Physical model.....	46
2.2.5	CO ₂ utilization and recycling.....	48
2.3	Discussion.....	52
2.4	Conclusions.....	56
3	Cell Voltage Optimization	59
3.1	Introduction	59
3.2	Results	62
3.2.1	Gas-fed flow cell.....	62
3.2.2	Membrane contribution.....	64
3.2.3	Electrolyte considerations	66
3.2.4	Zirfon optimization	70
3.2.5	Electrolyte mixing	72
3.2.6	Temperature	77
3.2.7	Voltage optimization summary	80
3.3	Discussion.....	82

3.4	Conclusions.....	85
4	Surface Modification	87
4.1	Introduction	87
4.2	Results: ionic liquid modification.....	91
4.2.1	Cathode modification with EMIMBF ₄	92
4.2.2	CO ₂ R with the IL-modified electrode.....	94
4.2.3	Characterization of the EMIM-modified electrode	96
4.2.4	Potassium-free CO ₂ R	100
4.3	Results: phosphonic acid modification.....	102
4.3.1	Influence of TDPA on CO ₂ R selectivity	102
4.4	Discussion.....	104
4.5	Conclusions.....	107
5	Conclusions and Perspectives.....	109
5.1	General conclusions.....	109
5.2	Future perspectives.....	112
6	Experimental Procedures	115
6.1	Materials	115
6.2	Synthesis and preparations	116
6.3	Physical characterization.....	117
6.4	Electrochemical procedures	118
6.4.1	ECSA	119
6.5	Operational parameters.....	119

6.5.1	IL deposition.....	120
6.6	Quantification	121
6.6.1	Product analysis.....	121
6.6.2	Figures of merit	122
6.6.3	Electrolyte Analysis	123
6.6.4	Outlet Stream Analysis.....	123
6.7	Physical model.....	124
6.7.1	Governing equations	127
	Bibliography	129
	Appendix.....	147

List of Abbreviations

Acronym	Definition
AEM	Anion exchange membrane
ATR-FTIR	Attenuated total reflectance-Fourier transform infrared
BPM	Bipolar membrane
C ₁	Monocarbon (products)
C ₂₊	Multicarbon (products)
CCS	Carbon capture and storage
CCU	Carbon capture and utilization
CDR	Carbon dioxide removal
CE	Counter electrode
CEM	Cation exchange membrane
CL	Catalyst layer
CO ₂ R	CO ₂ reduction
CP	Chronopotentiometry
d _{ab}	Distance between anode and back plate
DAC	Direct air capture
d _{am}	Distance between anode and membrane
d _{cg}	Distance between cathode and gas-flow plate
d _{cm}	Distance between cathode and membrane
DFT	Density functional theory
e ⁻	Electron
E ^o , E ^o _{red}	Standard reduction potential

E°_{cell}	Standard cell voltage
E°_{ox}	Standard oxidation potential
E_{anol}	Anolyte voltage drop
E_{cath}	Catholyte voltage drop
E_{cell}	Measured cell voltage
ECSA	Electrochemical surface area
EDX	Energy dispersive x-ray spectroscopy
EE	Energy efficiency
E_{m}	Membrane voltage drop
EMIMBF ₄	1-ethyl-3-methylimidazolium tetrafluoroborate
EOR	Enhanced oil recovery
E_{ox}	Measured oxidation potential
E_{red}	Measured reduction potential
FE	Faradaic efficiency
GC	Gas chromatograph
GDE	Gas-diffusion electrode
GDL	Gas-diffusion layer
GHG	Greenhouse gas
HER	Hydrogen evolution reaction
ICP-MS	Inductively coupled plasma-mass spectroscopy
IEM	Ionic exchange membrane
IHP	Inner Helmholtz plane
IL	Interlayer
j	Current density
LSV	Linear sweep voltammogram
MEA	Membrane-electrode assembly
NMR	Nuclear magnetic resonance

NP	Nanoparticle
OER	Oxygen evolution reaction
OHP	Outer Helmholtz plane
PTFE	Polytetrafluoroethylene
r-CO ₂	Regenerated CO ₂
RE	Reference electrode
RHE	Reversible hydrogen electrode
SEM	Scanning electron microscopy
SPC	Single-pass conversion
TDPA	Tetradecylphosphonic acid
TEM	Transmission electron microscopy
VE	Voltage efficiency
WCA	Water contact angle
WE	Working electrode
XPS	X-ray photoelectron spectrometry
XRD	X-ray diffraction
η	Overpotential

Chapter 1

Introduction

1.1 Energy crisis

Throughout history, energy in its various forms has been pivotal in driving humanity's progress and sustaining thriving civilizations. The twenty-first century represents a defining period in the paradigm of energy utilization, where the methods of production and consumption will shape the future of the entire planet. Since the advent of the industrial revolution, many resources have been employed to sustain an ever-increasing need for energy at such a rate that the Earth's natural cycles cannot adapt or recover, leading to profound disruptions in the entire biosphere. A fundamental change is urgently needed in the paradigm of producing and consuming resources, and the supply of secure, clean, sustainable energy is likely the most critical challenge that we, as a species, will have to face in the years to come.¹

In 2022, the overall energy consumption of the world was ca. 179,000 TWh. A diverse pool of resources was employed to draw this enormous amount of energy (Figure 1.1)² with oil, coal, and natural gas accounting for the majority of the sources (76.6%), followed by an array of renewables (19.6%) and nuclear power (3.8%). The intensive exploitation of fossil fuels (oil, coal, and gas) for the energy mix poses a problem due to their limited availability and the gaseous waste associated with their utilization. Such fossil fuels are formed from organic matter derived from prehistoric plants and animals buried under layers of sediments and rock

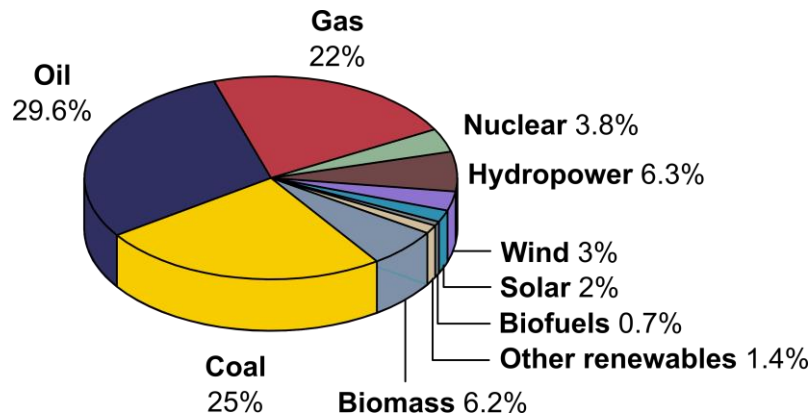


Figure 1.1 Global primary energy consumption by source in 2022. Data from ref. 2.

over the course of millions of years.³ The rate at which they are extracted and used today will see depletion occur at a much faster timescale than formation, making them a non-renewable energy source. In addition, combustion of fossil fuels leads to the release of carbon dioxide (CO₂) that has been stored in the Earth's crust for millions of years, thereby disrupting the natural carbon cycle. CO₂ is a greenhouse gas (GHG) partially responsible for what is known as the greenhouse effect, a natural phenomenon keeping the global average temperature at a value of 15 °C. Part of the solar irradiation that reaches Earth is absorbed by the surface and reemitted toward space, but the majority of this energy is reabsorbed by the atmosphere instead of being dispersed and it is converted to heat, which warms the surface of the planet.⁴ This is possible thanks to the GHGs present in the atmosphere, able to absorb infrared radiation. The main GHGs are water vapor, CO₂, methane (CH₄), and nitrous oxide (N₂O). Except water vapor, these gases are emitted at an alarming rate as a result of anthropogenic activities, and by accumulating in the atmosphere they enhance the greenhouse effect, leading to an increase in the Earth's surface temperature. Among these, CO₂ is by far the most relevant emitted GHG, owing to its relatively large concentration and long permanence time in the atmosphere.⁵ CO₂ emissions are closely related to fossil fuels consumption and they are undoubtedly linked to the increase in global temperature. The atmospheric concentration of CO₂ has been stable for at least the last 650,000 years, oscillating between 200 and 300 ppm.⁶ Then, from the beginning of the industrial revolution (around the 19th century), CO₂ started accumulating and since the '50s the increase became exponential, reaching an average value

of 417 ppm in 2022.⁷ As a result, the average temperature nowadays is 1.1 ± 0.2 °C higher than pre-industrial times.⁸ This seemingly small increase is already enough to have a strong impact on the whole ecosystem, being the cause of extreme weather events (hurricanes, heatwaves, wildfires) that cause victims and damages for billions of dollars.⁹ If GHGs continue to be emitted according to the current climate policies, the temperature increase by 2100 will be of 2.5 - 2.9 °C,¹⁰ while 2 °C is already enough to cause devastating effects on a global scale.

In the effort of limiting climate change, 196 parties adopted The Paris Agreement in 2015 during the UN Climate Change Conference, with the goal of containing the temperature increase to 1.5 °C by the end of the century. To achieve this ambitious goal, CO₂ emissions need to be halved by 2030 and reach net zero no later than 2050. At the same time, population and energy demand are expected to increase in the next decades, which further complicates the challenges ahead. In 2019, a total of 51.1 Gt of carbon dioxide equivalents (CO₂e, a parameter used to compare GHG emissions with different global warming potential to that of CO₂) were emitted from a wide range of human activities, from electricity production and industry to transportation and agriculture (Figure 1.2).¹¹ Therefore, strategies to limit emissions across all the different sectors of modern life are imperative. The International Energy Agency (IEA) recently assessed the latest developments across various components of the energy

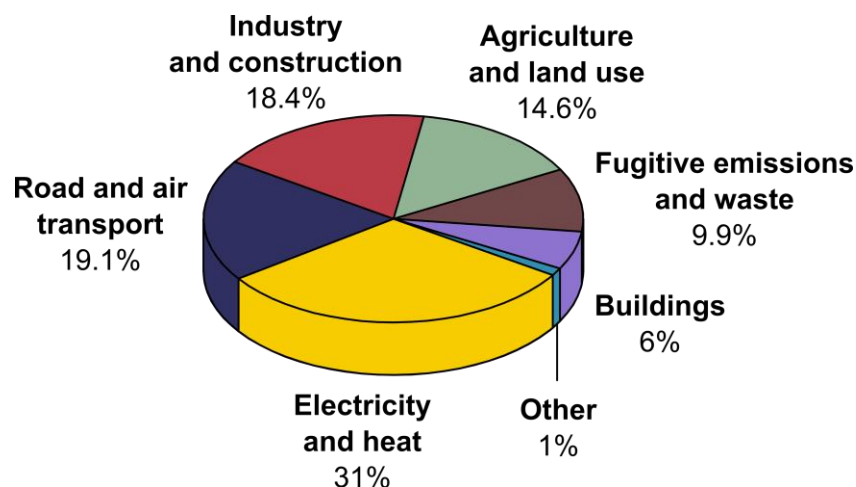


Figure 1.2 Greenhouse gas emissions by sector in 2019 expressed in % of the total (51.1 Gt of CO₂e). Data from ref. 11.

system that are pivotal for the transition to clean and renewable energy.¹² Out of the more than 50 components evaluated, only 3 (solar photovoltaics, electric vehicles, and lightning) are considered on the right path to achieve the goals set by the Paris Agreement, while a few others are experiencing rapid advancement (nuclear, heat pumps, and water electrolyzers). These findings depict a picture where progress towards a clean energy economy is gaining momentum, but the development of current technologies and emergence of new ones is fundamental to significantly limit global warming.

The general idea associated with the strategies aimed at cutting emissions is that the carbon economy needs to shift from linear to circular. To do so, three main paths can be followed: (i) decarbonization, (ii) carbon removal, and (iii) carbon recycling.¹³ (i) Decarbonation consists in avoiding the use of resources that eventually result in CO₂ emissions, thereby decoupling energy production from fossil fuels. Instead, renewable sources like photovoltaics, wind energy, and hydropower can be used as clean alternatives. However, sun and wind are intrinsically intermittent and the electrical energy that can be produced through solar panels and wind turbines has to be used immediately or stored. (ii) Carbon dioxide removal (CDR) is considered necessary to limit global warming at 1.5 °C.¹⁴ CO₂ can be captured either from the air (direct air capture, DAC)¹⁵ or from point sources such as industries working with coal, cement, iron, and steel¹⁶, which could be done by employing alkaline aqueous solutions or solid sorbents.¹⁵ After capture, CO₂ can be permanently stored underground (carbon capture and storage, CCS) in its gaseous form or mineralized into carbonates¹⁷. At present, a few large-scale CCS plants are operative, but they are all associated with enhanced oil recovery (EOR), where CO₂ pressure is used to extract additional oil from the wells.¹⁸ CCS is a promising strategy for net-zero or even net-negative emissions;¹⁹ however, the high capture costs and the lack of policies and economic incentives greatly limit the market for this technology, which will not be viable as long as CCS costs more than emitting CO₂.²⁰ (iii) Instead of being stored, captured CO₂ can be used as a feedstock for the production of high-value fuels and chemicals (carbon capture and utilization, CCU), which could be achieved via

biological, photochemical, thermochemical, and electrochemical approaches. In nature, photosynthetic organisms present an elegant way to transform CO₂ in complex organic molecules, albeit with a low efficiency (< 1% of solar energy is stored in the final products).²¹ By genetically modifying some of these organisms, natural pathways can be improved and tuned to yield products such as bio-plastics, bio-alcohols, and bio-diesel.²² A second strategy that finds inspiration in nature is artificial photosynthesis, where molecules (metal complexes, photosensitizers) and materials (semiconductors) make use of solar irradiation to photochemically convert CO₂ to carbon monoxide, methane, and formic acid in abiotic processes.^{23,24} At high temperatures, CO₂ can be transformed into carbon monoxide via the reverse water gas shift reaction, which can then be mixed with H₂ to form syngas. This reactive mixture is subsequently used to obtain hydrocarbons within the Fischer-Tropsch process or to produce methanol.^{25,26} Lastly, electrochemical conversion involves the use of electric power to transform CO₂ in high added value products like fuels and feedstock for the chemical industry. This approach is particularly interesting because it can be directly coupled with the power generated from renewable sources with the possibility of storing the surplus energy in chemical bonds for later use, thereby solving the problem of intermittent electricity production. Electrochemical CO₂ conversion is the focus of the present work, and will be discussed in detail in the next sections.

It is likely that a combination of the three strategies presented here (decarbonization, CCS, and CCU) will be needed to significantly reduce emissions and achieve net-zero by 2050. Moreover, strong policies will be necessary to discourage the extraction and consumption of fossil fuels and endorse the rapid development of technologies for an economy based on renewable energy.

1.2 CO₂ electroreduction

Electrochemical CO₂ reduction (CO₂R) offers a sustainable route to generate valuable chemical products from CO₂, H₂O and renewable electricity sources.^{27,28} However, many challenges hinder the commercial-scale implementation of this technology.

CO₂ is the final product of combustion and represents the most oxidized state of carbon. As such, it is a thermodynamically stable molecule ($\Delta G_f^\circ = -396 \text{ kJ mol}^{-1}$) that requires a significant energy input to reach lower and less stable oxidation states.²⁹ Electricity can be used as the energy source to transform CO₂ into reduced products, a process that necessitates electrons and protons to form chemical bonds in which the electric energy is stored. The first comprehensive study of CO₂ reduction on metallic surfaces was reported in 1985 by Hori and coworkers,³⁰ and since then scientific interest concerning CO₂R has seen continued growth.

1.2.1 CO₂R products

A wide range of relevant carbon products can be obtained from CO₂ including carbon monoxide (CO), formic acid/formate (HCOOH/HCOO⁻), methanol (CH₃OH), methane (CH₄), ethylene (C₂H₄), ethanol (C₂H₅OH), and propanol (C₃H₇OH). Among these, multicarbon products (species containing more than one carbon atom, C₂₊) are more appealing due to their high market price and considerable annual production (Table 1.1).³¹ In addition, the volumetric energy density increases with the number of carbon atoms (e.g. ethanol has a higher energy content than methanol, 21.2 MJ L⁻¹ and 15.8 MJ L⁻¹, respectively).³² Therefore, ethylene and ethanol could represent the best products to target in a CO₂ reduction system. Ethylene is widely employed as a plastic precursor and its current production involves energy-intensive processes like steam cracking of petroleum and natural gas (~ 850 °C) and separation techniques (distillation, compression).^{33,34} Ethanol can be used in the transport sector as an energy-dense drop-in fuel and today it is mainly obtained through fermentation of biomass.³⁵ Even though a renewable source is used in this case, the feedstocks employed are starch-

based crops such as corn, which raises ethical concerns over using a food source for fuel production.³⁶

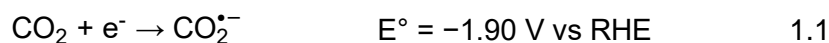
CO₂ electrochemical conversion offers a pathway to obtain these crucial products for the economy in a sustainable way, by using waste CO₂ and renewable energy. However, the industrial feasibility of CO₂-derived fuel production will heavily depend on cost-efficient processes and cheap, low-carbon electricity in order to compete with the low market prices that fossil fuels have today.

Table 1.1 Market price and production of relevant CO₂R products. Data from ref. 31.

Product	Market price / \$ kg ⁻¹	Annual production / Mt
CO	0.6	0.8
HCOOH	0.74	0.6
CH ₃ OH	0.58	110.0
CH ₄	0.22	2350
C ₂ H ₄	1.30	140.0
C ₂ H ₅ OH	1.00	77.0
C ₃ H ₇ OH	1.43	0.2

1.2.2 Electrocatalysis

The injection of electrons (e⁻) into the molecule is required for CO₂ activation and subsequent reaction. When electricity is used as the driving force to reduce CO₂, it is useful to consider the standard reduction potentials (E°) for each product (Table 1.2),¹³ a parameter indicating the energy needed to overcome the thermodynamic barrier separating the stable reactant from the more energetic products. CO₂ activation can be achieved with a first electron transfer to obtain the radical anion CO₂^{•-}, a reaction with a very negative E° (-1.90 V vs RHE) indicating the thermodynamic stability of the reactant (Equation 1.1).³⁷



However, usually the reduction is accompanied by proton (H^+) transfers that lower the energy requirement of the reaction and consequently the standard potentials become more favorable, with more positive values for all the products of interest. Nevertheless, the multiple electron and proton transfers needed to obtain the products raise the kinetic barrier for the reaction, increasing the energy input needed to drive the process.³⁸ Therefore, the resulting overall potential can be divided in thermodynamic contribution (E°) and kinetic contribution (termed overpotential, see Section 1.2.5).

Table 1.2 Standard reduction potentials for common CO_2R products (aqueous solution, pH 7). Data from ref. 13.

Reductive half-reactions	$E^\circ / \text{V vs RHE}$
$\text{CO}_2 + 2\text{H}^+ + 2\text{e}^- \rightarrow \text{CO} + \text{H}_2\text{O}$	-0.10
$\text{CO}_2 + 2\text{H}^+ + 2\text{e}^- \rightarrow \text{HCOOH}$	-0.12
$\text{CO}_2 + 6\text{H}^+ + 6\text{e}^- \rightarrow \text{CH}_3\text{OH} + \text{H}_2\text{O}$	0.03
$\text{CO}_2 + 8\text{H}^+ + 8\text{e}^- \rightarrow \text{CH}_4 + 2\text{H}_2\text{O}$	0.17
$2\text{CO}_2 + 12\text{H}^+ + 12\text{e}^- \rightarrow \text{C}_2\text{H}_4 + 4\text{H}_2\text{O}$	0.08
$2\text{CO}_2 + 12\text{H}^+ + 12\text{e}^- \rightarrow \text{C}_2\text{H}_5\text{OH} + 3\text{H}_2\text{O}$	0.09
$3\text{CO}_2 + 18\text{H}^+ + 18\text{e}^- \rightarrow \text{C}_3\text{H}_7\text{OH} + 5\text{H}_2\text{O}$	0.10

Electrocatalysis for CO_2R can be distinguished according to the type of electrocatalyst used to overcome the energetic barrier of the reaction. Homogeneous catalysis has been thoroughly studied over the years and involves the use of molecular catalysts (namely metal complexes with organic ligands) that bind and convert CO_2 .³⁹ These systems provide valuable mechanistic insights for the reduction pathways and also benefit from easy tuning and high product selectivity.⁴⁰ However, their low stability, high cost and poor recovery do not make them attractive for industrial applications for the time being. Instead, heterogeneous catalysis is

better suited for large-scale CO₂R owing to the long term activity and robustness of the catalysts.^{41,42} From here, only heterogeneous catalysis will be discussed.

Heterogeneous catalysts are sorted into two main groups: metallic and non-metallic. Among the metallic, some are monometallic (Au, Cu, Fe, In), some bimetallic (AuCu, PdPt), and others are ion-modified (Ag-Cl) or oxide (Ag-O) catalysts, while the non-metallic group includes mainly carbon-based catalysts (N-doped carbon, carbon nanofibers, B-doped diamond).⁴³ In particular, metal catalysts have attracted great interest and have been the subject of many investigations, either as flat surfaces,^{41,44} or nanostructured materials.^{42,45} Many challenges still hinder the development of electrocatalysts with activity, stability and selectivity compatible with industrial requirements. Importantly, the active sites and reaction mechanisms of heterogeneous catalysts are not easy to elucidate due to the not yet complete understanding of the surface-mediated electrochemical processes.⁴³

Selectivity

In order to obtain the desired products from CO₂ reduction, the Sabatier principle provides the basis to identify the best catalysts by connecting the chemical structure with the catalytic activity. The principle states that the binding energy between a catalyst and the reactant should be neither too strong nor too weak, since if the affinity is too low the reactant will not interact with the catalyst surface, while if the bond is too strong the product will not desorb from the surface, inhibiting further reaction.⁴⁶ CO₂R usual products span from carbon monoxide (2-electron transfer) to propanol (18-electron transfer), but even more reduced species such as butanol can be formed. Given the wide range of possibilities, it is important to select the right catalyst in order to obtain the targeted compounds. Metallic materials can be classified according to their product selectivity. Au, Ag, Zn, Pd, and Ga produce mainly CO; Pb, Hg, In, Sn, Cd, and Tl are selective towards HCOO⁻; Ni, Fe, Pt, and Ti do not reduce CO₂ and yield H₂ as the major product.⁴⁷ Cu is unique among transition metals, as it is the only one capable of forming multicarbon products (C₂H₄, C₂H₅OH, and C₃H₇OH) at significant activity alongside

monocarbon products (CH_4 , CO , and HCOO^-).^{47,48} The different selectivity is ascribed to the binding affinity of the various metals towards key reaction intermediates (Figure 1.3): adsorbed CO (CO^*) for CO_2R and adsorbed H (H^*) for hydrogen production.⁴⁹ CO^- and HCOO^- -forming elements have slightly negative adsorption energies for CO^* , which allows them to release the carbon product upon formation (affinity for another intermediate, $^*\text{OCHO}$, is important for the selectivity of formate, see next section). Conversely, H_2 -producing metals have a binding affinity for H^* close to zero, allowing to form and release H_2 , but they have a strong adsorption energy for CO^* , which remains bound to the surface and poisons the catalyst. Cu exhibits an intermediate combination of a slightly positive affinity for H^* and a negative binding energy for CO^* . In this situation, CO^* might stay bound just enough time for it to react with other adsorbed CO intermediates, thereby forming multicarbon products.^{49,50}

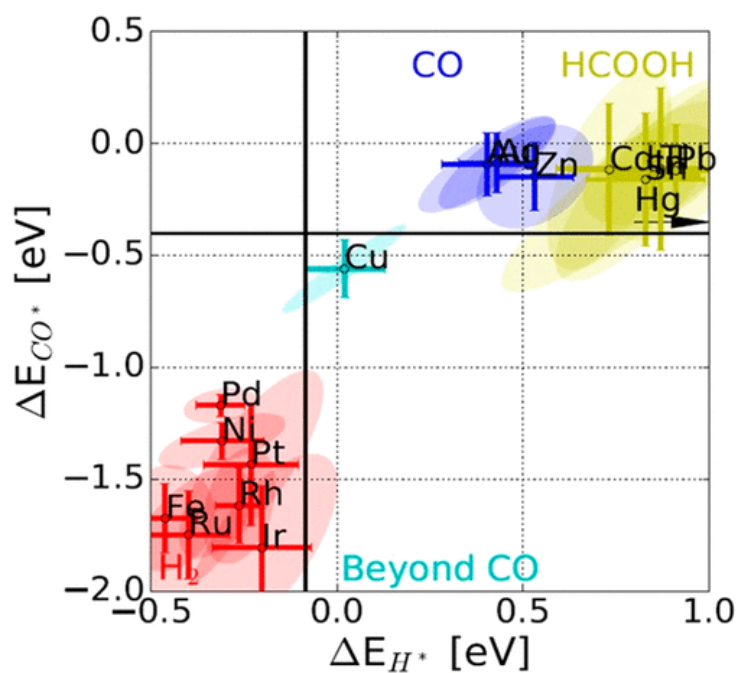


Figure 1.3 Metal catalyst classification according to the major CO_2R product. The binding energy of CO^* (ΔE_{CO^*}) and H^* (ΔE_{H^*}) are reported to rationalize the difference in selectivity. Reproduced from ref. 13.

1.2.3 Reactions on Cu

Copper is a highly abundant element in the Earth's crust, with excellent thermal and electrical conductivity.⁵¹ As such, it represents an optimal candidate for scalable CO₂R. However, given its widespread use in the electrical grid, copper is thought to become a critical resource for the energy transition and its demand is expected to double by 2035, which would result in higher prices and possibly limited availability.⁵² As Cu will likely be one of the most popular catalysts for CO₂ conversion, it is important to assess and understand the underlying mechanisms of the reaction. In addition, the environment in which CO₂R takes place (described in more detail in the next sections) influences the process and may also lead to unwanted side-reactions, such as H₂ evolution; therefore, the variables that determine the reaction conditions must be understood in order to control the activity and the selectivity of the conversion.

Selectivity-controlling parameters

In the context of CO₂R, Cu stands out due to its ability to facilitate C-C coupling, resulting in high added-value hydrocarbons and alcohols formation. However, copper displays low selectivity for individual products as several carbon species are formed simultaneously. The interactions between the catalyst and its environment are complex and many parameters play a role in the selectivity including Cu facets,^{53,54} defective sites,^{55,56} oxidation states,⁵⁷⁻⁵⁹ doping elements,⁶⁰⁻⁶² pH,⁶³⁻⁶⁵ applied potential,⁶⁶ and electrolyte.⁶⁷ The intrinsic characteristic of the Cu catalyst directly affect the product distribution. De Gregorio et al. showed that precise control of the facets exposed by Cu nanoparticles (NPs) leads to a drastic change in selectivity, with nanocubes exposing the (100) crystal plane being more selective towards ethylene, while nanooctahedra presenting the (111) crystal plane favor methane production.⁵³ By introducing a high degree of defective sites on a Cu surface, Gu et al. reported a catalyst with a marked selectivity towards ethanol and propanol, showing the benefits of having a stepped catalyst surface for oxygenated products formation.⁵⁵ De Luna et al. presented a study in which Cu⁺ species are stabilized within the structure of the catalyst thanks to copper dissolution/electro-redeposition techniques, allowing to favor ethylene production at fast reaction rates while

suppressing methane formation.⁵⁹ The introduction of heteroatoms can also steer the selectivity, as shown by Liang et al. with a copper nitride catalyst that affords an enhanced selectivity for multicarbon products as a result of a modified surface electronic structure.⁶⁰ Other than the catalyst nature, the conditions in which CO₂R is carried out also strongly influence the product distribution. The influence of the pH is exemplified by Kas et al. in a report that showed how the methane/ethylene production can be tuned by varying the pH at the electrode surface, with a preference for ethylene at high pH values.⁶³ Kuhl et al. provided insights into the potential-dependent product formation, reporting 16 CO₂R products encompassing alcohols, aldehydes, and carboxylic acids, indicating how the chosen cathodic potential can direct the selectivity.⁶⁶ The product selectivity is also affected by the electrolyte composition, as described by Bui et al. in a study reporting favored C₂₊ product formation with large cations (Cs⁺) present in solution, while buffering anions (HCO₃⁻, HPO₄²⁻) boost methane production at the expense of multicarbon products.⁶⁷ Taken together, all these different effects influencing the catalyst selectivity complicate the understanding of the pathways leading from CO₂ to a specific product. Theoretical methods can prove useful in this context, as they shed some light on the reaction mechanisms that might suggest catalyst designs to improve the selectivity.

Reaction pathways

Theoretical and computational approaches provide helpful insights to rationalize reaction pathways, but they too are hindered by the extreme complexity of the reactions on an atomic scale (for example, ethylene and ethanol formation are 12-electron/12-proton processes that involve many steps and intermediates).⁶⁸ Even if modeling cannot yet suggest rational catalyst design to target specific products, important advancements have been made (Figure 1.4). Experimental and computational investigations identified the formation of *CO₂⁻ as the first step of reduction on Cu, a reaction in which the linear CO₂ assumes a bent, active configuration.^{69,70} CO and HCOO⁻ are the first products to form after CO₂ activation, each requiring two electrons. After one-electron and one-proton transfer steps to CO₂, the resulting

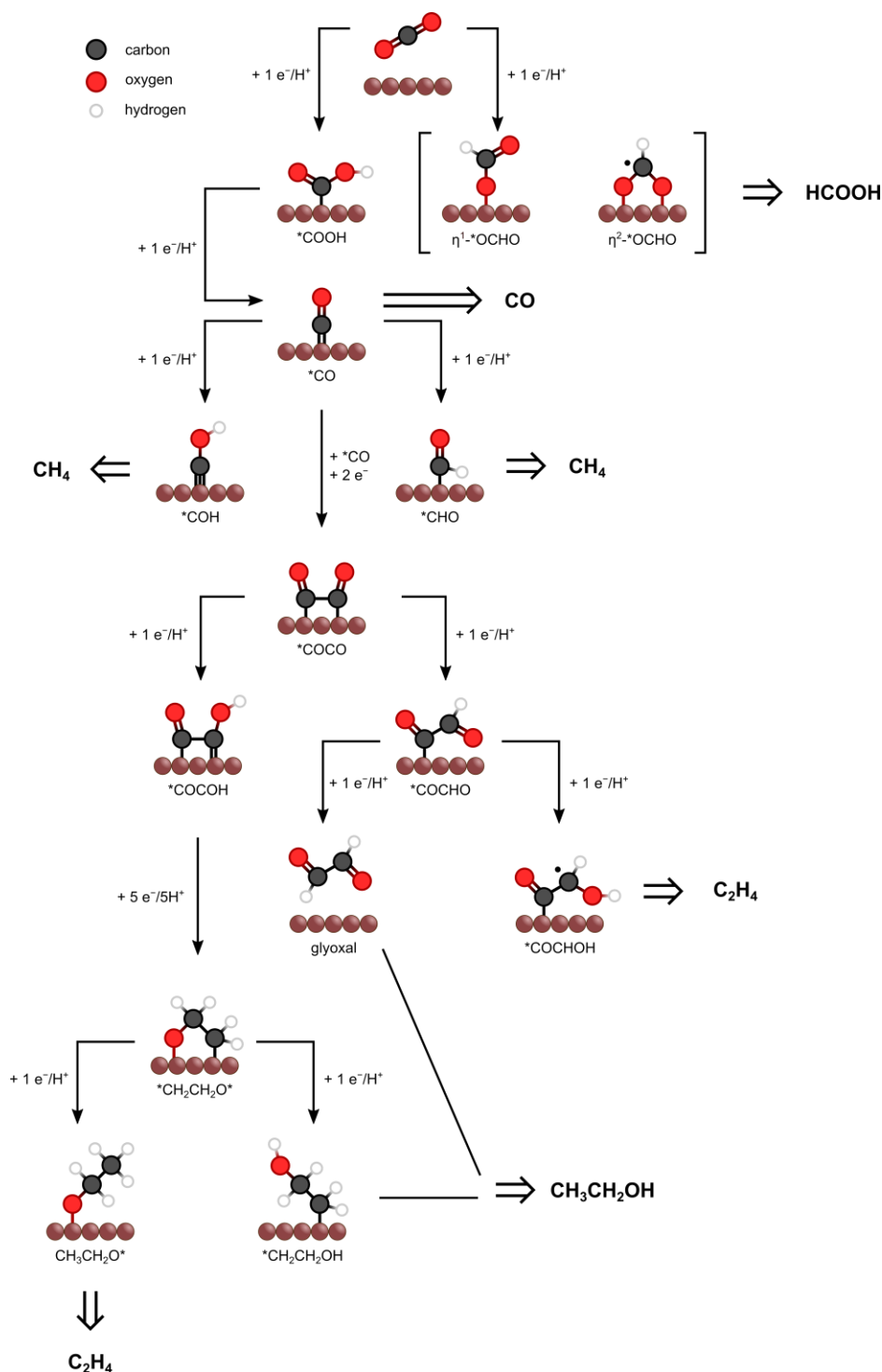


Figure 1.4 Illustration of some suggested pathways for CO_2R . Adapted from ref. 68.

intermediate is bound to the surface either via the carbon atom or the oxygen atoms, a difference that very likely determines the subsequent product formation.⁷¹ Evidence suggests that a *COOH intermediate (bound through the C atom) leads to CO production, while *OCHO (bound through one or two O atom(s)) results in HCOO^- formation. Importantly, heterolytic

C–O bond cleavage of $^*\text{COOH}$ generates the $^*\text{CO}$ species, which is the precursor of all further reduced products (C_1 and C_{2+} species requiring $> 2 e^-$),⁷² whereas the $^*\text{OCHO}$ pathway leads only to formate, which does not participate in subsequent reduction reactions.⁷³ Further H^+ - and e^- -transfers to $^*\text{CO}$ form $^*\text{COH}$ and $^*\text{CHO}$ intermediates, which continue down the CH_4 formation pathway.⁶⁸ There is general consensus on the fact that surface-bound $^*\text{CO}$ is a key intermediate to obtain C_{2+} products through C–C coupling, given that its surface coverage is thought to be high compared to other intermediates that could result in multicarbon products formation (like $^*\text{COH}$ and $^*\text{CHO}$).^{72,74–76} Dimerization of two $^*\text{CO}$ species leads to $^*\text{COCO}$, which can then be reduced and protonated on an O atom or on a C atom, forming $^*\text{COCOH}$ and $^*\text{COCHO}$, respectively. The relative stability of these two intermediates is under debate, with some groups favoring $^*\text{COCOH}$,^{77,78} and others preferring $^*\text{COCHO}$.^{79,80} While the steps described until now have been the object of thorough investigations, less work has been dedicated to the competition between ethylene and ethanol, and consensus regarding the pathways leading to one product or the other is still lacking. The differences in the various suggested mechanisms to C_2 products concern mainly the first intermediate ($^*\text{COCOH}$ or $^*\text{COCHO}$), the dehydration step (where one O atom of the initial CO_2 is lost as water), and the steps where the bifurcation between the ethylene and ethanol pathways occurs.⁶⁸ To give an idea of the wide range of proposed mechanisms, the bifurcation is thought to happen as early as the reduction/protonation step after $^*\text{COCHO}$ ($5 e^-$ -reduced intermediate), forming glyoxal and $^*\text{COCHOH}$ which ultimately result in ethanol and ethylene, respectively.⁸¹ Alternatively, the separation point could concern a late and almost completely reduced intermediate, $^*\text{CH}_2\text{CH}_2\text{O}^*$ ($10 e^-$ -reduced intermediate), which upon one H^+ - and one e^- -transfer produces $\text{CH}_3\text{CH}_2\text{O}^*$ and $^*\text{CH}_2\text{CH}_2\text{OH}$, eventually leading to ethylene and ethanol formation, respectively.⁸² Although efforts are still needed to uncover the precise mechanisms of CO_2 reduction, future developments of theoretical and computational techniques might be able to provide valuable insights allowing to target specific products.

Competitive hydrogen evolution

As CO₂R reduction is often carried out in aqueous environment, the hydrogen evolution reaction (HER) becomes a major challenge. The ever-present HER competes for the available electrons with CO₂R, which may lower the selectivity for carbon products in favor of hydrogen production. HER can occur either through the reduction of protons (Equation 1.2) or through water reduction (Equation 1.3).⁸³ The importance of this distinction is discussed in Section 1.4.



1.2.4 Oxygen evolution reaction

Reduction processes are always coupled with oxidation reactions that provide the electrons needed for the reductive conversion. The oxidation half-reaction that typically accompanies CO₂R is the oxygen evolution reaction (OER, Equation 1.4). This process requires a large energy input to overcome the unfavorable standard reduction potential and sluggish kinetics resulting from the several steps needed to form oxygen, which is often viewed as a bottleneck for the development of CO₂R technologies. Despite this, water is considered the only viable source of renewable electrons that is suitable for large-scale applications.⁸⁴



Considering the reductive and oxidative processes described in these sections, the complete reaction leading to the production of renewable carbon-based feedstock and fuels is identical to the one happening during natural photosynthesis, where CO₂ and H₂O are combined to form organic molecules and O₂ (Table A.1). Phototrophic organisms use solar energy to drive the process and, ideally, photon will be used to generate sustainable electricity to power CO₂R devices.

1.2.5 CO₂R parameters

Among the many variables that describe an electrocatalytic system, some fundamental parameters are used to generally evaluate the performance of a specific electrolyzer: (i) current density, (ii) overpotential, and (iii) Faradaic efficiency.²⁰

(i) The current density (j) of an electrode is defined as the electron flux per unit area (mA cm^{-2}) and it reflects the rate of reaction. (ii) The overpotential (η) is the difference between the experimentally measured potential and the standard potential for a specific reaction. This additional voltage is due to the energy losses within the system caused by mass transfer limitations, ohmic resistance, and activation barriers. It is important to reduce the overpotentials as much as possible in order to lower the operating energy costs. The full cell voltage (E_{cell}) is an indicator of the energy needed to make the electrolyzer work, which accounts for thermodynamic voltage, overpotentials, and resistive losses. (iii) The Faradaic efficiency (FE) indicates the fraction of the total electrons supplied to the system that is used to form a specific product. Ideally, a reactor should have unit FE for a single product, but often the electrons are also used for unwanted side reactions (like HER) or for other carbon products formation.

Other necessary considerations such as single-pass conversion and reactant utilization will be described later in Chapter 2.

1.3 CO₂R electrolyzer

CO₂ reduction is carried out by applying a voltage across a pair of electrodes in an electrolytic cell, also called electrolyzer.³⁸ When performing heterogeneous catalysis, the catalyst is part the electrode itself. The design of the cell is important as it influences the CO₂ reduction process and the overall performance of the device. Four main components usually make up the CO₂R electrolyzer: a cathode, where the CO₂R (reductive half-reaction) takes place; an

anode, where OER (oxidative half-reaction) occurs; an aqueous electrolyte solution, which allows reactant and products mass transport as well as charge conductivity; and a membrane, used to divide the cathodic and the anodic environments.⁸⁵ Depending on their configuration, different setups can be obtained. Some common reactor architectures, depicted in Figure 1.5, are H-cells, gas-fed flow cells (or flow cells), and membrane-electrode assembly (MEAs).⁸⁶

H-cells

H-cells (Figure 1.5a) have been extensively employed to evaluate CO₂R catalysts performance.^{54,66,85,87,88} Both electrodes consist in a piece of metallic catalyst submerged in the electrolyte solution (catholyte and anolyte for cathode and anode, respectively) and the reactor is separated in two half-cells by an ionic-exchange membrane (IEM) to avoid product crossover between the cell compartments. A three-electrode configuration is typically employed for electrochemical measurements, comprising a working electrode (WE), a counter electrode (CE) and a reference electrode (RE). In this setup the current flows between the WE and CE, while the potential of the WE is measured against the RE. The reaction of interest takes place at the WE, therefore in CO₂R the cathode is usually the WE, while the anode is the CE. The RE is often a Ag/AgCl electrode, which is inserted in the catholyte. During electrolysis, CO₂ is constantly bubbled in the catholyte through a frit and the solution is stirred to enhance the transport of the dissolved CO₂ to the cathode for reduction.⁸⁹ Even though H-cells constitute a relatively simple system where CO₂R can be tested on different catalysts and in various conditions, the low aqueous solubility of CO₂ results in low current densities. Since the diluted reactant has to diffuse from the bulk of the solution to the electrode, mass transport limitations arise due to the low concentration. Industrial settings require high current densities to be economically viable, therefore H-cells should be avoided when investigating CO₂R for practical applications.⁹⁰

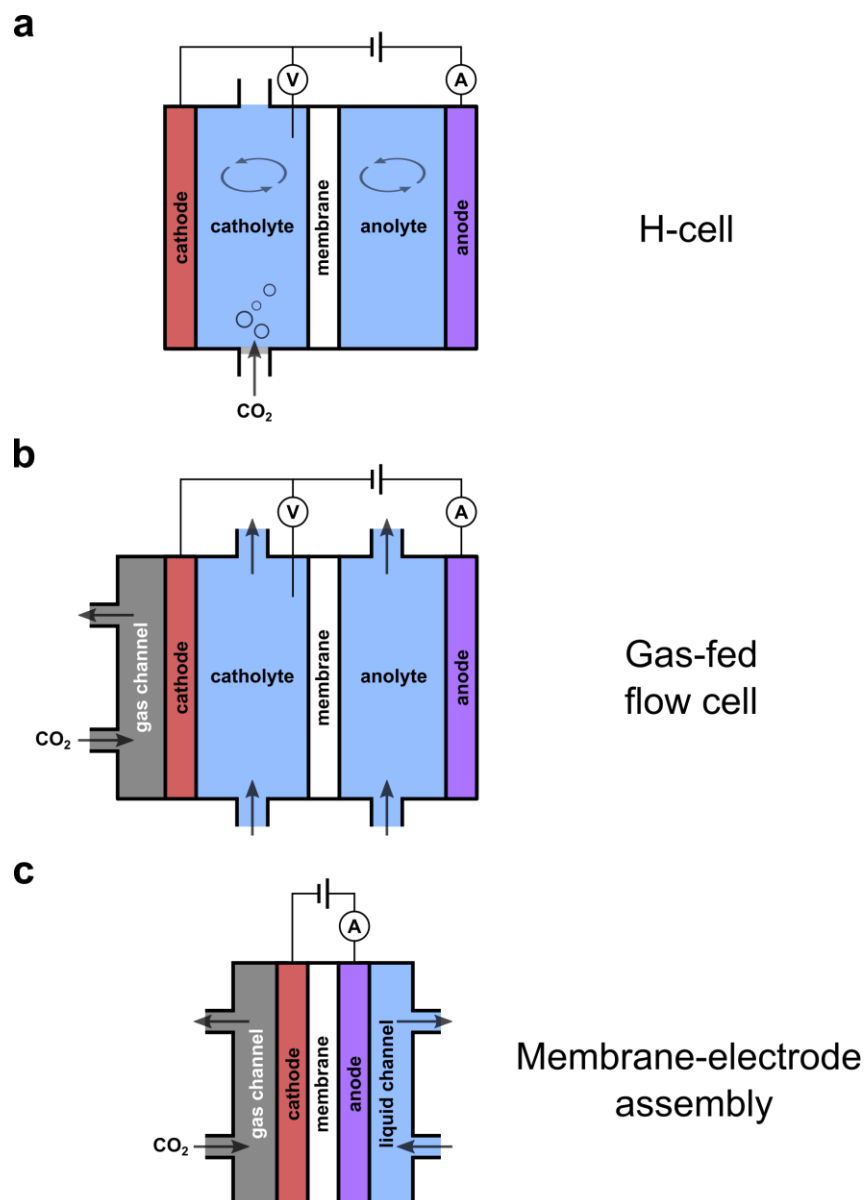


Figure 1.5 Common CO₂ electrolyzer architectures: (a) H-cell, (b) gas-fed flow cell, and (c) membrane-electrode assembly. The CO₂ supply method is shown for each configuration.

Gas-fed flow cells

Gas-fed flow cells (Figure 1.5b) are inspired by fuel cells and water electrolyzers, and have gained much attention in the past years owing to their efficient mass transport that overcomes limitations of H-cells.^{85,91–93} Similarly to H-cells, a three-electrode configuration can be used with both cathode and anode in contact with the respective electrolyte solution. However, two key differences characterize the gas-fed flow cell setup. First, catholyte and anolyte are continuously circulated through the cell in a closed loop involving external liquid reservoirs (one

for the catholyte and one for the anolyte). This causes the diffuse layer surrounding the catalyst to shrink compared to H-cells, which benefits the mass transport.⁹⁴ In addition, liquid products are quickly removed from the electrode environment, thereby favoring the reaction equilibrium. The second important feature is the nature of the cathode, which in this case is a gas-diffusion electrode (GDE). With a GDE, a flow of gaseous CO₂ provides continuous reactant supply to the catalyst by diffusing through the porous GDE, thus establishing a three-phase interface (catalyst, electrolyte, CO₂) where the catalyst is covered by a thin layer of electrolyte in equilibrium with CO₂.⁹⁵ This results in a much shorter diffusion distance for CO₂ to reach the active catalyst and a greater local CO₂ concentration, overcoming the mass transport limitations found in H-cells and allowing these configurations to attain current densities in the order of hundreds of mA cm⁻².²⁸ As shown in Figure 1.5b, the CO₂ is usually supplied through a gas channel positioned at the back of the gas-diffusion cathode. The most common GDE structure (Figure 1.6) found in the literature comprises a catalyst layer (CL), in contact with the electrolyte, deposited on a gas-diffusion layer (GDL), facing the CO₂ channel.⁹⁶ In the CL, an ionomer or polymer (e.g. Nafion, polytetrafluoroethylene) is added to the catalyst (usually

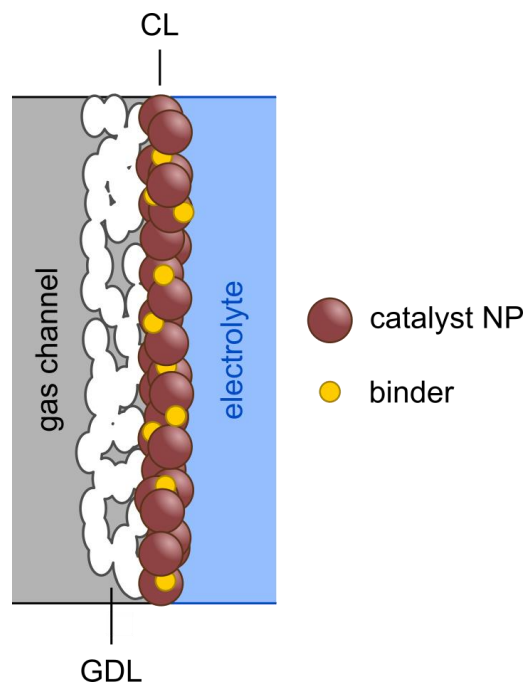


Figure 1.6 Illustration of the gas-diffusion electrode structure comprising a nanostructured catalyst layer deposited on a gas-diffusion layer.

nanoparticles and other nanostructures) acting as a binder to provide adhesion to the GDL. The gas-diffusion layer needs to be hydrophobic to prevent the electrolyte from entering the gas channel and is usually made of carbon fibers, polytetrafluoroethylene (PTFE), or a combination of the two. Deposition of the catalyst on the GDL can be achieved with different methods, divided in ink-based and ink-free approaches. When employing an ink (a dispersion of the catalyst nanopowder, solvent, and binder), air-brushing, drop-casting and hand-painting are viable deposition approaches that influence the resulting CL depending on parameters such as solvent evaporation rate and ink composition.^{95,97} On the other hand, ink-free methods encompass electrodeposition, sputtering, and ion-beam deposition.^{95,98–100}

Membrane-electrode assembly

A widespread reactor architecture derived from the gas-fed flow cell is the membrane-electrode assembly (MEA, Figure 1.5c), where both the cathode and the anode are porous electrodes pressed against the membrane without any liquid electrolyte separating them.⁹⁵ Instead, the membrane acts as a solid electrolyte for ionic transport, while the liquid environment for CO₂ dissolution and reaction is provided by a solution flowing behind the anode. This design results in compact electrolyzers benefiting from a reduced ohmic resistance and improved current densities.^{101,102}

1.3.1 Membranes

The ionic exchange membrane separating the two cell compartments plays a central role in the electrolyzer performance. The primary functions of the membrane are (i) to act as a barrier to avoid short-circuiting between the two electrodes, (ii) to prevent product crossover between the cell compartments, and (iii) to maintain the current flow in solution via selective ionic transport.¹⁰³ Polymeric IEMs feature fixed ion exchange groups interacting with counterion free to move within the matrix of the membrane, and they can be divided in two categories depending on the fixed functional groups: cation exchange membranes (CEMs) and anion exchange membranes (AEMs). CEMs (Figure 1.7a) are based on polymers bearing negatively

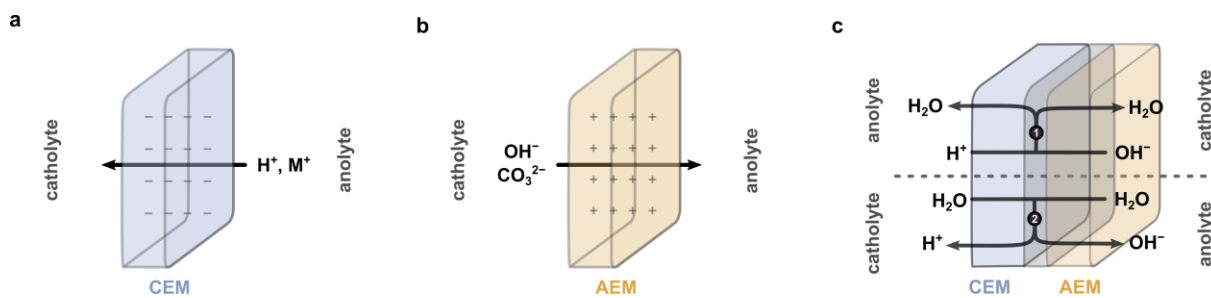


Figure 1.7 Illustration of some common membranes. (a) Cation exchange membrane, (b) anion exchange membrane, and (c) bipolar membrane. The BPM can be employed in forward bias (1) or reverse bias (2).

charged groups such as sulfonates and phosphonates, which allow the transport of cations (usually electrolyte species like protons and alkali metal ions). Conversely, AEMs (Figure 1.7b) present positively charged groups such as unsubstituted and substituted ammonium, allowing the transport of anionic species (hydroxyl, carbonates). In addition, CEMs and AEMs can be combined to form bipolar membranes (BPMs, Figure 1.7c), which greatly restrict crossover between the two compartments, while charge conduction is maintained by water formation (forward bias) or water dissociation (reverse bias).¹⁰³ The specific combination of membrane and electrolyte solution chosen for the system will influence the CO₂R performance. CEMs provide a good charge conductivity, but if too many H⁺ are transferred from anode to cathode they might favor HER over CO₂R. AEMs avoid this problem and are suited to be employed in alkaline electrolytes, however they might transfer CO₂-derived carbonate species to the anode, negatively impacting the conversion (see Chapter 2). Finally, BPMs provide the advantage of blocking any crossover, but they are not yet as developed as the other two kinds of IEM. All three membranes can potentially be employed in each of the reactor architectures described earlier.

CO₂ electrolyzer configurations are varied and each provides insights to design reactors with a better reduction performance. However, as already mentioned, H-cells should be avoided during optimization for industrial applications, since they do not provide a good representation

of the conditions required in larger electrolyzers. Instead, gas-fed flow cells and MEAs are more suitable platforms to test catalysts, since by enabling high current densities at moderate overpotentials they provide the right conditions for reaction scale-up.

1.4 Local environment

1.4.1 Electrode/electrolyte interface

Electrocatalytic CO₂ reduction takes place at the cathode/electrolyte interface. Hence, a precise understanding of this region is needed to elucidate how the different variables influence the conversion. The voltage applied between the two electrodes results in the accumulation of positive charges present in solution at the cathode surface, which strongly affects the interactions between the solvent and the solute species with the electrode. This leads to the establishment of a region called the electrical double layer.³⁸ The cathode/double layer structure is usually divided in five sections: the electrode surface, the inner Helmholtz plane (IHP), the outer Helmholtz plane (OHP), the diffuse layer, and the bulk solution (Figure 1.8). Closest to the cathode, the IHP can contain specifically adsorbed species, solvent molecules, solvated ions, reaction intermediates, reactants and products. The OHP is adjacent to the IHP and mainly encompasses solvated ions with a charge opposite to that of the electrode (positive, in this case) which are not adsorbed and interact with the surface through electrostatic forces. The diffuse layer is characterized by concentration gradients of solution species (ions or electroactive molecules) that decrease from their bulk value to almost zero at the electrode surface. The combination of Helmholtz and diffuse layers form the electrical double layer, holding a total charge density that is equal and opposite to that of the cathode, whose structure influences surface electrochemical processes.^{38,104} As CO₂R is an inner sphere process, the activation and proton- and electron-transfer steps take place within the IHP.^{38,105,106}

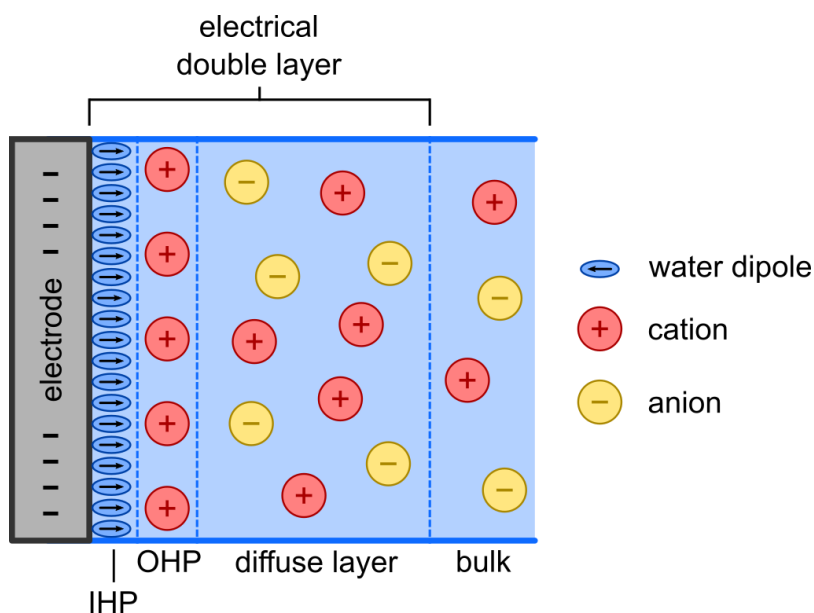


Figure 1.8 Electrical double layer structure with simplified electrolyte species distribution across the different regions. Adapted from ref. 38.

1.4.2 Current density effects

The local environment at the cathode changes depending on the current density (i.e. reaction rate), and while it is not perturbed at very low current densities, small increases heavily alter the conditions at the electrode surface. Therefore, CO_2R itself modifies key parameters such as the local pH, CO_2 concentration and proton donor.

At very low current densities, the protons needed for the reduction can be supplied from the hydronium ions present in the electrolyte. However, as the current increases, depletion of hydronium ions quickly occurs and water becomes the main proton donor for the reaction (Figure 1.9a), leading to hydroxide generation as a byproduct, which sharply increases the local pH independently of the bulk pH value (Figure 1.9b).⁹⁴ The pH increase is very sharp and starts at low current densities ($1\text{-}2\text{ mA cm}^{-2}$) even in neutral electrolytes owing to the relatively slow diffusion of OH^- away from the cathode and towards the bulk. It has been reported that a high local pH favors CO and C_{2+} products, while H_2 and CH_4 are suppressed.^{107,108} It is possible that this selectivity arises from the fact that water dissociation and H^* binding energy (both important for HER) are not favored in alkaline conditions, resulting in suppressed HER.

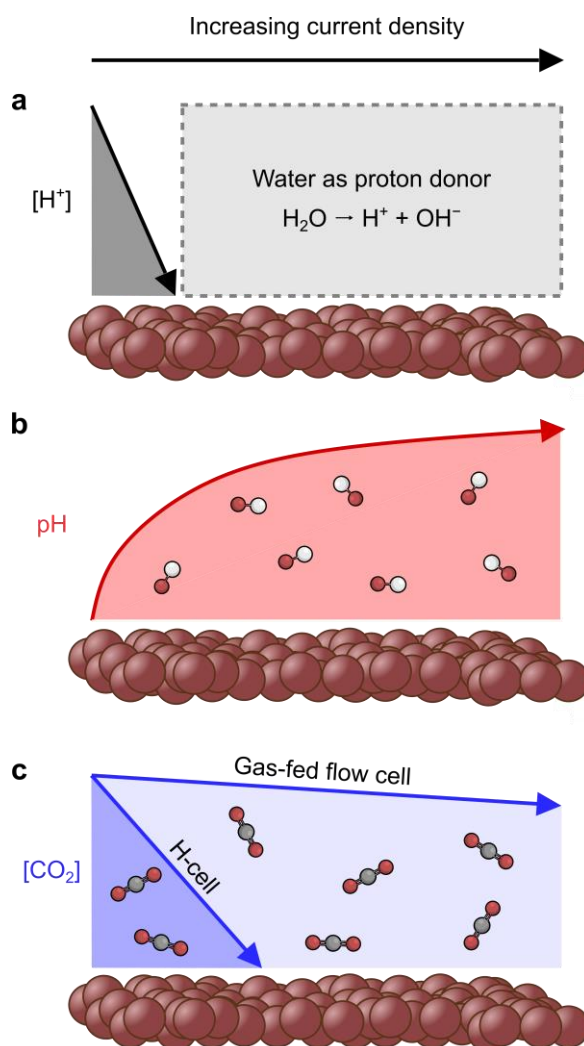


Figure 1.9 Effects of the current density on the local environment of the cathode. (a) Proton source for CO_2R (and HER), (b) surface pH, and (c) local CO_2 concentration. Adapted from ref. 94.

Concerning the increased selectivity for multicarbon products, it could be the result of a combination of factors such as improved CO onset potentials, modification of CO^* binding energy and of the energetics of the C-C coupling step. CO_2 concentration at the electrode decreases due to the conversion to products and the reaction with OH^- with subsequent (bi)carbonate formation (see Section 1.4.3), two processes enhanced at high current densities. Nevertheless, the gas-fed flow cell setup benefits from a more efficient CO_2 mass transport that limits the concentration drop and assures a constant reactant supply (Figure 1.9c).⁹⁴ As already mentioned, gas-fed flow cells allow the formation of a three-phase environment between catalyst, electrolyte and CO_2 . However, it is worth noting that experimental evidence

points towards a two-phase reaction, where CO_2 first dissolves in the electrolyte solution and then diffuses to react at the electrode surface, rather than reacting from the gas phase. Metallic catalysts tend to be hydrophilic when a negative potential is applied, thus the entire catalyst layer is likely wetted by the electrolyte during electrolysis. Moreover, it has been shown that CO_2R takes place mainly in a thin layer within the catalyst, at the backside of the catalyst layer, a region closer to the flow of CO_2 .⁹⁴

The hydrogen evolution reaction will also be influenced by the different conditions set by high current densities. A preference for HER to follow the water reduction pathway (Equation 1.3) over the proton reduction pathway (Equation 1.2) is expected in alkaline conditions when the proton concentration is low. However, even at lower pH values this might be the favored reaction since the H^+ concentration at the electrode decreases during electrolysis due to slow mass transport.^{109,110} It is important to differentiate between water and proton reduction, because it has been reported that on copper HER competes with CO_2 by following the water reduction pathway, even in acidic solutions. In addition, water reduction is partially inhibited by CO_2R via adsorbed CO species that block active sites on the surface, thereby promoting CO_2 reduction over HER.⁸³ Despite this, HER activity can become predominant due to other factors such as the insufficient supply of CO_2 and catalyst deactivation.

1.4.3 Electrolyte and pH effects

The composition and concentration of the electrolyte solution has an important impact on the CO_2R process, as it affects electrostatic interactions, buffer ability, pH, and availability of proton donors.¹³

CO_2 can exist in solution in equilibrium between three different forms, depending on the pH of the electrolyte (Figure 1.10).¹¹¹ For a pH lower than 6.4 (i.e. pK_a of CO_2 , formation of H_2CO_3 is neglected due to its low concentrations, as the equilibrium is considerably shifted towards CO_2) solvated CO_2 is the predominant form; between pH 6.4 and 10.3 (pK_a of bicarbonate, HCO_3^-) HCO_3^- is the species with the highest concentration; at pH values above 10.3 the equilibrium

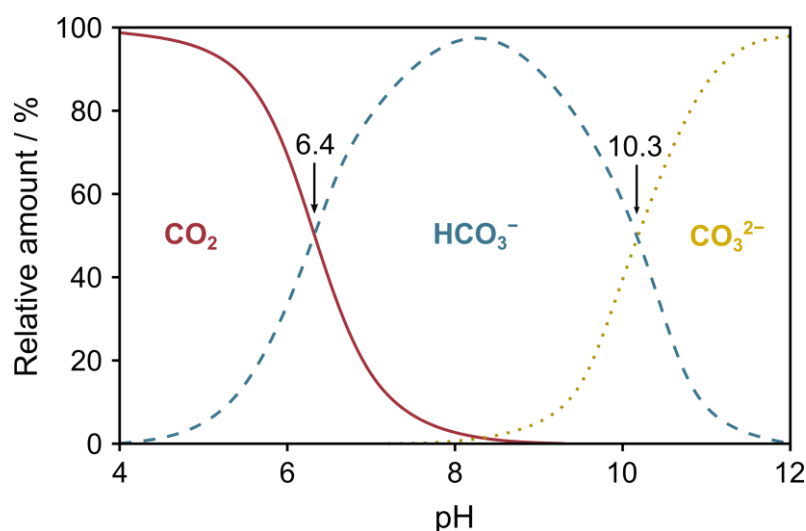


Figure 1.10 CO_2 pH-dependent equilibrium in solution. Adapted from ref. 111.

is shifted towards carbonate (CO_3^{2-}). Hence, the pH is extremely important in determining the reaction pathways preferred at the electrode surface, where CO_2R and HER are in competition for electrons and protons. As already mentioned, a higher pH suppresses HER and favors C_{2+} products, but it also causes CO_2 to be consumed in (bi)carbonate production, which might lead to selectivity and reactant utilization issues (discussed later in Chapter 2).¹³

Ionic solutes are fundamental to provide current flow in solution and thus closing the cell circuit, but they also affect catalytic CO_2R . Alkali metal cations (Na^+ , K^+ , Cs^+) have been reported to influence activity and selectivity at the electrode. Solvated cations are expected to accumulate at the cathode surface (either via specific adsorption or nonspecific interactions) during electrolysis, which can lead to active site blockage, modification of the energy barrier for reaction steps, or influence of the binding affinity and coverage of reaction intermediates.¹¹² In addition, the presence of positively charged ions close to the negative cathode creates intense electric fields that further modify the cathode local environment.¹¹³ The cations interact with CO_2R intermediates through electrostatic interactions, promoting the reaction by stabilizing the intermediates on the surface, an effect that is enhanced by the size of the ions. This is due to the fact that large cations accumulate more favorably at the OHP than smaller ones (according to density functional theory, DFT, studies), leading to a more intense electric field.¹¹⁴ Anions have a minor impact on CO_2R and have been studied less compared to cations. Typical anions

are Cl^- , SO_4^{2-} , CO_3^{2-} , HPO_4^{2-} and OH^- . It has been suggested that phosphates favor HER over CO_2R , and that halides might enhance the CO_2 -to-CO process,¹¹⁵ altering the selectivity for CO_2R . However, more investigations are needed to have a better understanding of the way in which different anions influence the activity of the catalyst.¹³

1.5 Commercial CO_2 conversion

1.5.1 Industrial requirements

To be commercially competitive, CO_2R electrolyzers will have to run at high current densities (100-1000 mA cm^{-2}) to cover the reactor capital cost and have fast reaction rates providing a constant product output. At the same time, the system operating costs will be based on the electric energy consumption needed to drive the reaction, which determines the energy efficiency (EE) of the system. For a reactor forming a single carbon product (e.g. CO), the EE depends on the voltage efficiency (VE, linked to the E_{cell}) and on the FE according to Equations 1.5 and 1.6:¹¹⁶

$$\text{VE} = \frac{E_{\text{red}}^{\circ} - E_{\text{ox}}^{\circ}}{E_{\text{cell}}} \quad 1.5$$

$$\text{EE} = \text{VE} \times \text{FE}_{\text{CO}} \quad 1.6$$

Where E_{red}° is the standard potential for CO_2R to CO (cathodic half-reaction), E_{ox}° is the standard potential for OER (anodic half-reaction) and E_{cell} is the measured cell voltage. Therefore, the VE measures how high the operative voltage is compared to the thermodynamic requirement of the reactor. While commercial water-splitting electrolyzers operate at EEs above 70%, the energy efficiency for CO_2R systems is still limited by large cathodic and anodic overpotentials. In order to obtain industrially viable reactors, the overall energy requirement must be lowered while operating at high current densities.

1.5.2 Prototype systems

CO₂R processes have already been demonstrated at a pilot-plant level.¹¹⁷ Examples of purely electrochemical systems are provided by Dioxide Materials, with the development of CO- and HCOOH-producing reactors. CO₂-to-CO was performed at 500 mA cm⁻² with an |E_{cell}| of 3 V and a FE of 95% for 3000 h using a Ag catalyst,¹¹⁸ while CO₂-to-HCOOH was achieved at 160 mA cm⁻² with an |E_{cell}| of 3.5 V and a FE of 90% using a Sn catalyst.¹¹⁹ In both cases, an anion exchange membrane (Sustainion) was employed to separate the cell compartments. A collaboration between Evonik and Siemens produced a hybrid system comprising an electrolyzer coupled with a fermenter.¹²⁰ Syngas with different CO/H₂ ratios was electrochemically produced at 150 mA cm⁻² with an |E_{cell}| of 5 V. Then, the gas was fed to fermenters with different types of bacteria to obtain butanol/hexanol or acetate/ethanol mixtures.

CO₂ electroreduction is a fast-growing field. In recent years, the rapid development has been driven by the decreasing price of renewable energy, the urgent need to defossilize the economy, and the improving performance of the systems. Performant reactor designs with highly active catalysts have been fundamental for the advancements and pilot plants encourage more efforts to achieve commercialization on a large-scale.¹²¹

1.6 Aim of the thesis

The development of scalable, efficient CO₂ reduction systems must progress at a rapid pace to put CO₂ recycling and conversion technologies at the forefront of the sustainable energy transition. Electrochemical CO₂R devices are approaching commercialization, but efforts are still needed to build optimized reactors forming cheap carbon products able to compete with those derived from fossil fuels. In this thesis, strategies oriented towards the optimization of reactor performance will be presented.

The following chapters deal with key electrolysis parameters such as CO₂ utilization, cell voltage, and product selectivity. Chapter 2 focuses on improving the CO₂ utilization of the system, minimizing reactant loss by employing an acid catholyte to prevent permanent CO₂ conversion to (bi)carbonate species and by recycling the unused CO₂ bypassing the reactor with a simple recovery setup. Given the importance of reactant utilization and recycle, the acid electrolyte is featured in all of the systems described in this work. In Chapter 3, the cell voltage is addressed through the modification of the electrolyte composition and the type of compartment separator. In addition, the idea of using a single electrolyte solution for both cell compartments is assessed with the goal of improving the system stability over time. Finally, Chapter 4 presents ways to modify the surface of copper nanoparticles with an ionic liquid and a phosphonic acid in the effort of directing the catalyst selectivity towards multicarbon products.

Chapter 2

CO₂ Recycling from Carbonate

This chapter was written on the basis of the following paper: *Acidic Electroreduction of CO₂ to Multi-Carbon Products with CO₂ Recovery and Recycling from Carbonate*, by Alessandro Perazio, Charles E. Creissen, Jose Guillermo Rivera de la Cruz, Moritz W. Schreiber, and Marc Fontecave, *ACS Energy Lett.* **8**, 2979–2985 (2023).¹²²

2.1 Introduction

The development of devices such as gas-fed flow cells (here termed flow cells) have made CO₂ reduction suitable for industrial applications, scale-up and commercialization. Flow cells overcome a critical drawback of the more traditional H-cell setup, for which the low solubility of CO₂ in water (ca. 33 mM) gives rise to mass transport limitations,¹²³ limiting the maximum current density achievable to less than 50 mA cm⁻².¹²⁴ On the other hand, in flow cells the CO₂ is not bubbled in solution but rather the gas is supplied through the back of a gas diffusion electrode (GDE). The difference between the two supply methods is the effective diffusion length for CO₂ to reach the electrode surface following depletion from reaction. After reaching equilibrium under applied current, in H-cells there is an establishment of a thick diffuse layer that limits mass transport of CO₂ to the electrode, while in flow cells the diffuse layer thickness under working conditions is much smaller due to the enhanced convection given by the liquid

flow.⁹⁴ In addition, having a direct feed of gas means that a high concentration is present close to the catalyst, enabling to attain high current densities (hundreds of mA cm⁻²) at low overpotentials (<1 V).^{125–129} Flow cells are commonly operated with alkaline or neutral pH electrolyte solutions. Basic conditions have been preferred because they effectively inhibit HER by maintaining a low H⁺ concentration in solution while also boosting the current density and C₂₊ product selectivity.^{124,130} However, alkaline conditions prohibit high conversion yields due to the unwanted side reaction of CO₂ with hydroxide ions, which results in reactant loss through the formation of (bi)carbonate. Additionally, this process leads to changing electrolyte compositions and pH shifts over time, since OH⁻ ions are ultimately replaced by CO₃²⁻ (Figure 2.1a, Equations 2.1 and 2.2).^{131,132} Losing a significant amount of the reactant through (bi)carbonate formation is not economically feasible at industrial scales due to the cost associated with the regeneration of the electrolyte (i.e. reconversion of carbonate into CO₂), which accounts for more than half of the energy required for the electrolyzer in the case of an alkaline flow-cell.¹³³ The problem can be partially addressed by decreasing the electrolyte pH below the pK_a of bicarbonate formation^{134–136} (pK_a CO₂ = 6.4)¹³⁷ so that the thermodynamic equilibrium is almost quantitatively shifted towards CO₂. In practice, this means employing solutions with a pH equal or below 5.5 to ensure a CO₂/HCO₃⁻ ratio > 90%. In such acidic systems it is important to distinguish the local environment at the electrode surface from the

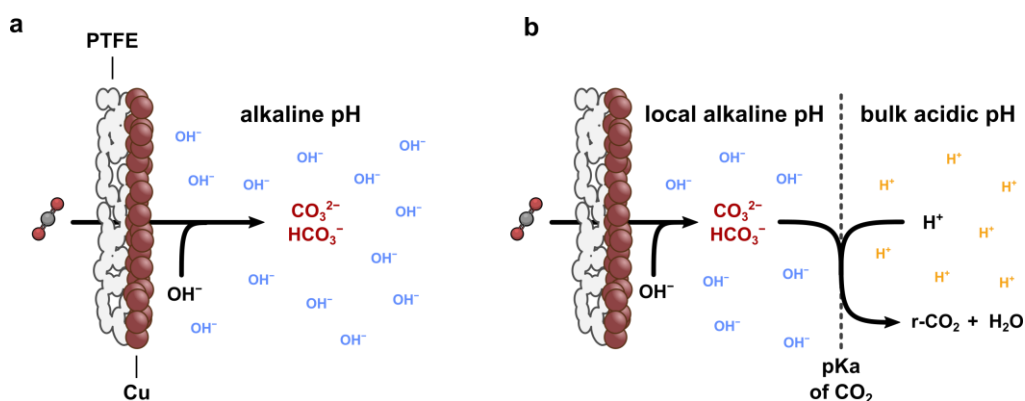
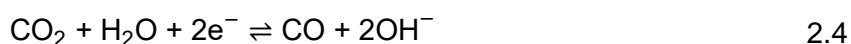


Figure 2.1 Schematic comparison of pH-related effects. (a) A Cu GDE interfaced with an alkaline bulk pH electrolyte, where (bi)carbonate species form and accumulate in solution. (b) A Cu GDE interfaced with an acid bulk pH electrolyte, in which (bi)carbonate species are formed and then converted back to r-CO₂ by protonation in the bulk solution.

bulk solution, especially in terms of pH. When performing electrolysis at high current densities ($> -150 \text{ mA cm}^{-2}$) in acid solutions, the proton source for CO₂R switches from H⁺ (Equation 2.3), predominant at the beginning of the electrolysis, to water when the H⁺ supply becomes diffusion limited (Equation 2.4).⁸³ As soon as water is factored into the equation, hydroxide ion production starts at a fast rate, resulting in the build-up of a local alkaline layer close to the electrode surface. As a consequence, temporary (bi)carbonate formation cannot be avoided even in acidic electrolytes.^{135,138} However, as these species diffuse into the bulk they are immediately converted back to CO₂ (here termed r-CO₂ as this is regenerated) due to the low pH (Figure 2.1b, Equations 2.5 and 2.6). By avoiding permanent (bi)carbonate formation, all of the feed CO₂ is potentially available for reduction. Nevertheless, this is only beneficial for the overall conversion to products if the r-CO₂ is eventually made available to be reduced at the cathode, otherwise it would be simply vented from the reactor, nullifying the advantages brought by the regeneration. For this reason, it is important to understand the generation and transport of r-CO₂ in a gas-fed flow cell by analyzing the composition of the different reactor gas outlets.



Despite the advantages brought by acid electrolytes, the strong H⁺ concentration in solution leads to high selectivity for HER, even in presence of CO₂. A simple way to solve this problem is the addition of alkali metal salts to the electrolyte solution. Alkali cations are essential to suppress HER^{139,140} in acid solutions and the larger the size of the ion, the stronger the effect.¹⁴¹ This is due to the higher hydration power that small ions experience when compared with larger

ions (cation radius increases following $\text{Li}^+ < \text{Na}^+ < \text{K}^+ < \text{Cs}^+$). A lower hydration ability means fewer water molecules surrounding the cation, which in turn increases their ability for adsorption on the negatively charged cathode. Positive charges adsorbed on the cathode have the effect of repelling protons, and since the rate-limiting step for H₂ evolution is $\text{H}^+ + \text{e}^- \rightarrow \text{H}\cdot$, HER is limited. Furthermore, the adsorbed cations can stabilize the singly reduced first intermediate, $\text{CO}_2^{\cdot-}$, which is involved in the rate-limiting step of CO₂R, through ion pairing, thereby favoring the reaction.¹⁴¹

The anodic half-cell is not the focus of this work, however, the choice of the anode and the anolyte it is interfaced with is important as it also indicates the kind of membrane that can be used to separate the cell compartments. So far, most of the existing CO₂R devices with flowing acidic catholyte have employed cation exchange membranes, which require acidic anolyte solutions to provide a constant H⁺ supply to the catholyte and maintain a low pH.^{134–136} As a consequence, these systems only support the use of acid-stable oxygen evolution reaction catalysts that contain expensive precious metals such as Ir or Ru, the cost of which has been identified as a barrier to device upscaling in water electrolyzers and therefore could also prove problematic for CO₂R devices.¹⁴² Bipolar membranes avoid this issue as they enable alkaline anolyte to be used in combination with acidic catholyte by maintaining a pH gradient through the cell. A BPM is composed of a negatively charged cation exchange layer (CEL) and a positively charged anion exchange layer (AEL) pressed against each other (Figure 2.2). When the membrane is placed in the reactor so that the CEL faces the catholyte and the AEL faces the anolyte (reverse bias mode), water molecules are cleaved into H⁺ and OH⁻ at the interlayer (IL, i.e. the space between the CEL and AEL) owing to the potential difference established between the two electrodes during electrolysis.¹⁴³ Subsequently, the ions diffuse either in the catholyte (H⁺) or in the anolyte (OH⁻) through the CEL and AEL, respectively, which enables the simultaneous use of an acid catholyte and basic anolyte and guarantees that the pH gradient is maintained over time. Although water dissociation adds a voltage penalty to the cell potential, BPMs enable the use of Earth-abundant catalysts for OER, which has been

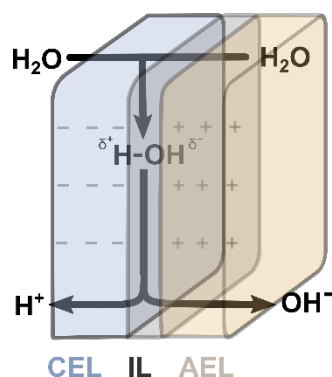


Figure 2.2 Schematic representation of a BPM used in reverse bias. Water dissociation provides protons and hydroxide ions which are supplied to the catholyte and anolyte, respectively. Cation exchange layer (CEL), anion exchange layer (AEL), interlayer (IL).

demonstrated in alkaline and neutral flow cells,^{144–146} and membrane electrode assemblies,^{147,148} but was not described in combination with an acidic catholyte at the beginning of this project. Additionally, BPMs avoids crossover of metal ions and cationic electrolyte species, which, if not prevented, can negatively impact device performance and long-term stability when CEMs are used.^{149,150}

The combination of acid electrolyte and specific cell setup used in this study highlights a route to bypass permanent carbonate formation, as confirmed by a full carbon mass balance. In addition, this reveals how r-CO₂ could be recovered as a high purity stream from one of the outlets, resulting in an easy and straightforward method to recycle and reuse CO₂, with the products being collected at a different gas outlet. Reducing the feed CO₂ flow rate was shown to enhance the selectivity towards multicarbon products like ethylene and ethanol, while increasing the CO₂-to-products conversion.

2.2 Results

The electrolyzer employed in this work (Figure 2.3) was equipped with a GDE consisting of a Cu catalyst deposited on a porous PTFE support. The CO₂ was supplied through the back of the cathode (PTFE side), while the copper was placed facing the acid catholyte. Separation of

the two half-cells with a bipolar membrane enabled the use of an alkaline anolyte (2.5 M KOH, pH 14) and a Ni foam anode, on which the OER takes place. The anodic side of the reactor was kept constant throughout all experiments, which were performed at a current density of -200 mA cm^{-2} .

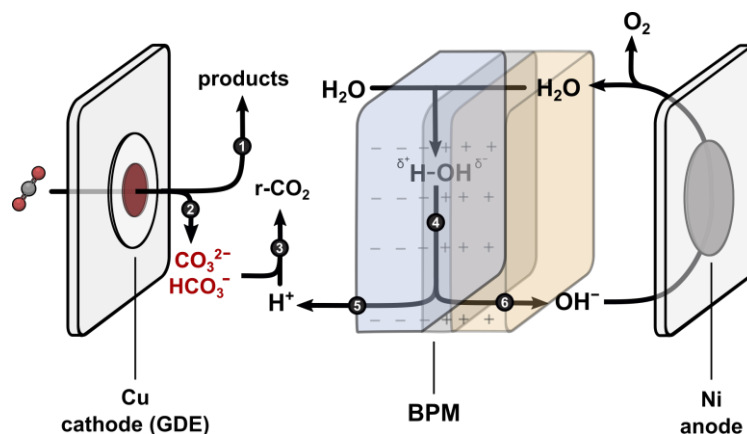


Figure 2.3 Gas-fed flow cell assembly, where (1) CO₂ is reduced to products, (2) CO₂ is converted to (bi)carbonate, (3) CO₂ is regenerated, (4) H₂O dissociates in the BPM interlayer, (5) protons diffuse through CEL into the catholyte, (6) hydroxide ions diffuse through the AEL into the anolyte.

2.2.1 Catalyst synthesis and characterization

Cu nanoparticles (NPs), the active catalyst, were prepared using a modified solvothermal procedure.¹⁵¹ In brief, an ethanolic solution of copper acetate was heated to different temperatures in a Teflon-lined autoclave for 20 h to obtain CuO NPs. The product was obtained through the alcohol-assisted thermal decomposition of copper acetate to copper oxide. Ethanol reacts with acetate in an esterification reaction to form ethyl acetate, allowing to obtain CuO at a considerably lower temperature than the one needed for the same reaction in air.^{137,151} Through this approach, various sizes of NPs could be obtained just by changing the reaction temperature: 10, 35, 50 and 80 nm (Table 2.1 and Figure A.1) determined via transmission electron microscopy (TEM). Among these, the highest selectivity for CO₂R over HER was obtained for the NPs with an average size of 50 nm (Figure 2.4), and therefore these were

Table 2.1 Sizes of CuO nanoparticles obtained with the solvothermal synthesis at different temperatures.

Temperature / °C	Size / nm
150	10
180	35
200	50
210	80

chosen for all subsequent experiments. X-ray diffraction (XRD) patterns of the as-prepared NPs displayed peaks corresponding to pure CuO (Figure 2.5, top). GDEs were prepared by spray-coating the CuO pre-catalyst dispersed in a Nafion-containing methanolic solution onto a PTFE membrane to reach a loading of around 2 mg cm^{-2} , corresponding to an approximate thickness of $6 \mu\text{m}$ (Figure 2.6). To obtain metallic Cu, the active catalyst, from the initial oxide, an activation step was required, which consisted in running consecutive linear sweep voltammograms (LSVs) from -0.5 V to -1.9 V vs. Ag/AgCl until the current response was constant (Figure A.2), followed by chronopotentiometry (CP) at -200 mA cm^{-2} for 1 h in a 3 M KCl catholyte solution. The metallic nature of the resulting active catalyst was confirmed by XRD (Figure 2.5, bottom). These activated Cu-GDEs were used for all experiments.

2.2.2 Catholyte selection

The first catholyte chosen was a 0.5 M KH₂PO₄ / 2 M KCl solution (pH 4) due to its good buffering properties. Employing buffered electrolytes could avoid the formation of an alkaline layer on the cathode surface by maintaining the local pH close to the value of the bulk,¹⁵² thereby preventing CO₂ conversion to (bi) carbonate. However a deterioration of the initially high C₂₊ product selectivity was observed over time (Figure 2.7). It can be speculated that the phosphate species could bind to Cu and alter the surface structure over time,¹⁵³ but validation of this requires additional experiments which are beyond the scope of this research. Sulfate anions represent a good alternative to phosphate species as they did not result in loss of C₂₊

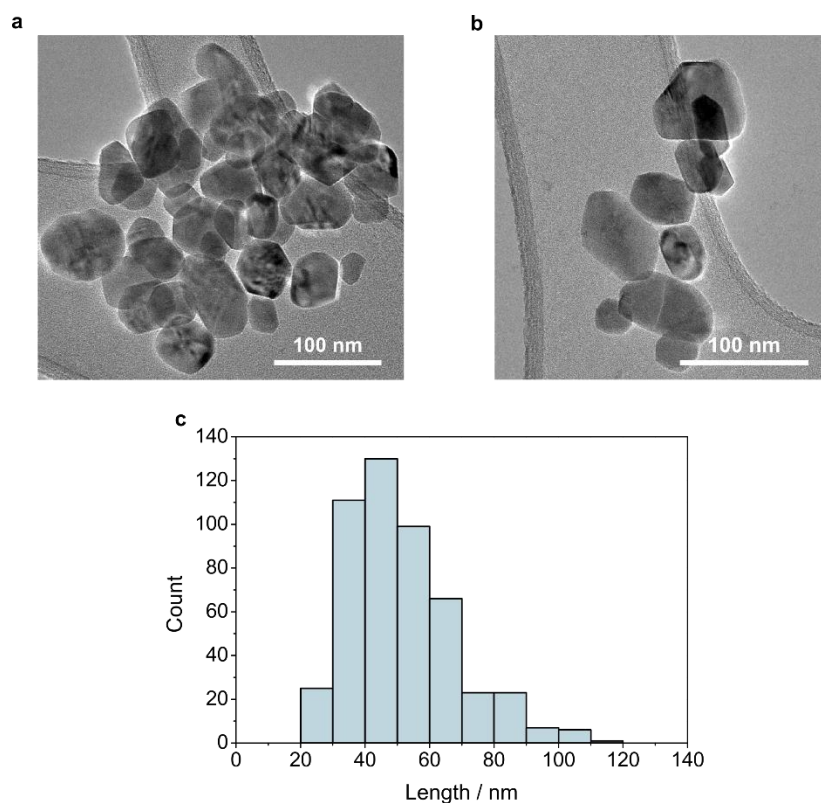


Figure 2.4 TEM images of the as-synthesized CuO NPs (a, b) and relative size distribution (c). The mean length is 50 nm.

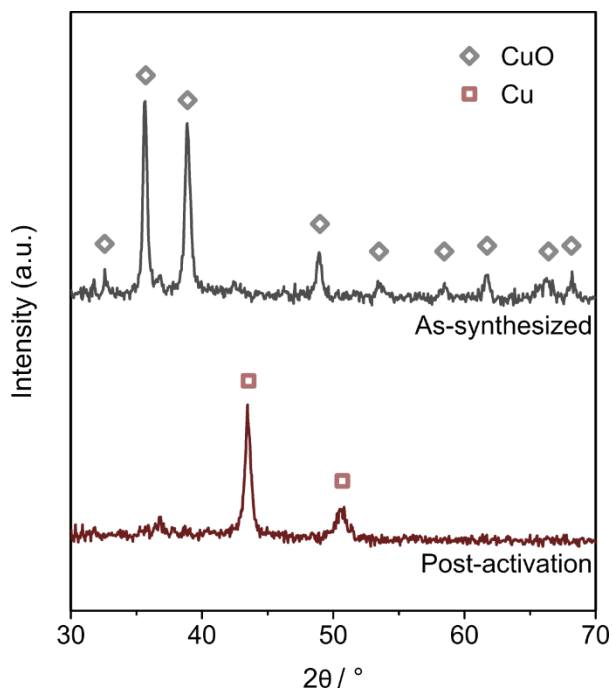


Figure 2.5 X-ray diffraction (XRD) diffractograms for the as-synthesized CuO nanoparticles (top, black) and the reduced Cu catalyst after activation (bottom, red).

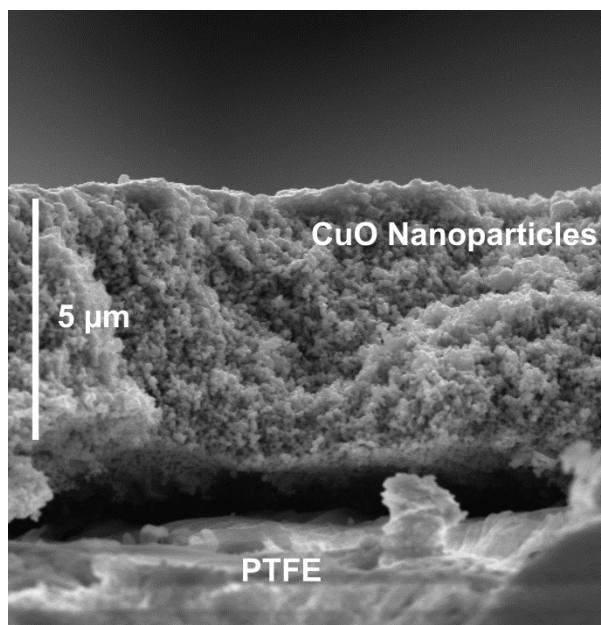


Figure 2.6 Cross-sectional SEM image of the pre-catalyst deposited on PTFE. The layer of the CuO NPs has a thickness of approximately 6 μm .

selectivity. Thus, phosphate salts were replaced with a low concentration of H₂SO₄ (0.05 M, pH 1) and the effects arising from the addition of varying amounts of KCl were explored at a current density of -200 mA cm^{-2} . As previously reported, adding KCl to an acidic solution favored CO₂R selectivity over HER (Figure 2.8).^{134,136,154,155} With a H⁺ concentration equal to 0.1 M, the addition of 0.5 M KCl was already sufficient to prevent significant H₂ evolution, but

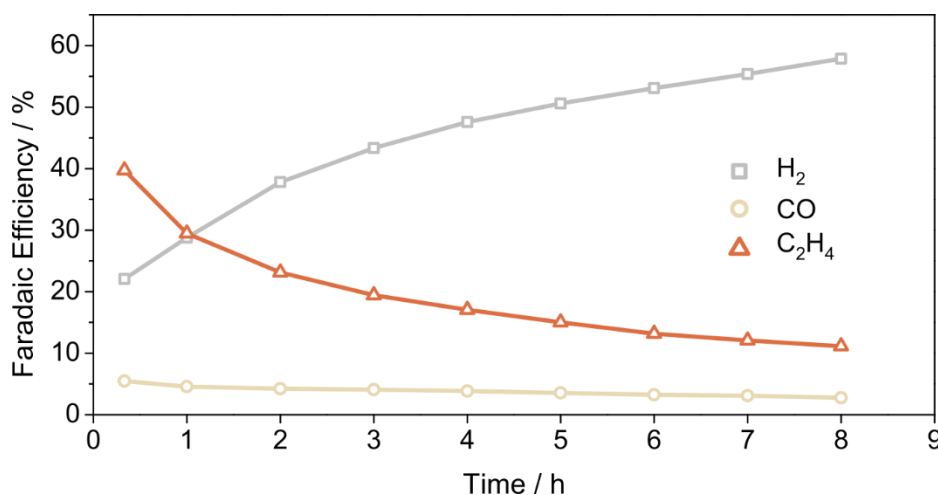


Figure 2.7 Long term electrolysis performed in 0.5 M KH₂PO₄ / 2 M KCl. The test was carried out at with a feed CO₂ flow rate of 2.5 mL min⁻¹ at -300 mA cm^{-2} ($E_{\text{cell}} = -8.5 \text{ V}$). Ethylene FE is initially high (40%) but it degrades quickly over time

the conductivity of the solution was not optimal, as indicated by the highly negative cell voltage (−5.3 V). Increasing the KCl concentration to 3 M diminished the resistance of the solution and lowered the cell voltage by 600 mV (−4.7 V) while the high selectivity for multicarbon products (52%) was maintained. A catholyte consisting of 0.05 M H₂SO₄ and 3 M KCl was used for all further experiments.

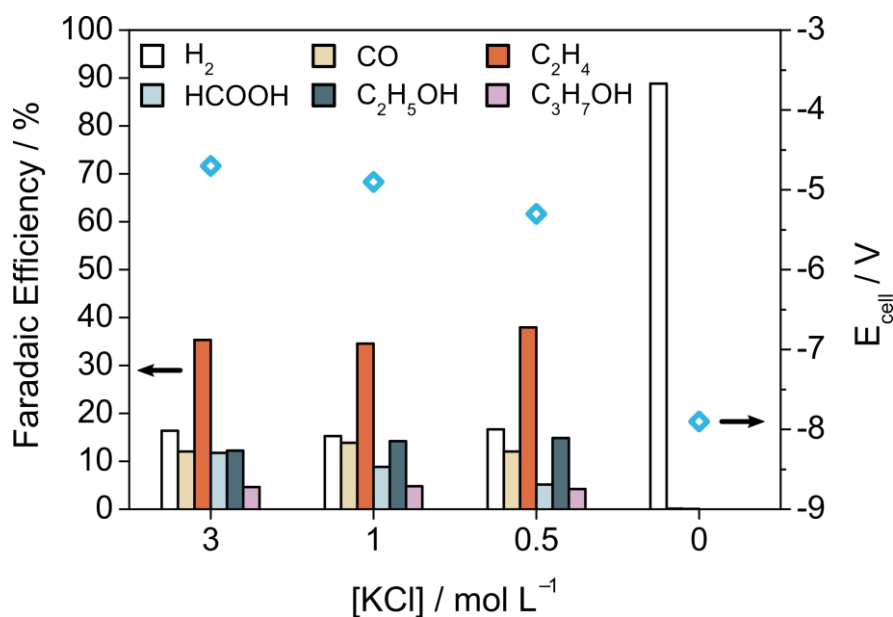


Figure 2.8 Effects of varying the KCl concentration in a 0.05 M H₂SO₄ electrolyte with a 10 mL min⁻¹ CO₂ feed flow rate at −200 mA cm⁻². In absence of KCl, CO₂R does not occur and HER is the only catalytic reaction happening at the cathode. 0.5 M of KCl is already enough to suppress H₂O reduction, but 3 M yields the same product distribution with a less negative E_{cell}.

2.2.3 Single-pass conversion

Once the acidic catholyte composition was optimized, efforts were focused on achieving the maximum conversion for CO₂ to CO₂R products. To evaluate this, a parameter termed the single-pass CO₂ conversion to CO₂R products (SPC) was defined, which describes the yield of CO₂R products with respect to the amount of CO₂ supplied (Equation 2.7).

$$\text{SPC (\%)} = \sum \left\{ \left[\left(\frac{j_{\text{product}} \times 60 \text{ s}}{n_{\text{electrons}} \times F} \right) \div \left(\frac{\text{flow rate}}{24.05} \right) \right] \times \text{carbon atoms} \times 100 \right\} \quad 2.7$$

In order to obtain the total SPC, the single pass conversion values for each carbon product were summed. In Equation 2.7, j_{product} is the partial current density (mA cm^{-2}) for a specific product, $n_{\text{electrons}}$ is the number of electrons needed for its production, F is the Faraday constant, the flow rate is the one chosen for the feed CO₂ (mL min^{-1}), and 24.05 is the molar volume of a gas (L) at normal temperature and pressure. In addition, a second parameter called CO₂ utilization was defined as the ratio of CO₂ used for reaction to the CO₂ available, calculated according to Equation 2.8, in which $\dot{n}_{\text{CO}_2\text{total}}$ (nmol s^{-1}) is the molar flow of CO₂ available for reaction (including r-CO₂ in the case of recycling, see below) and $\dot{n}_{\text{CO}_2\text{unused}}$ (nmol s^{-1}) is the molar flow of CO₂ that does not contribute to products and is vented from the system. It is important to note that the utilization is equivalent to the SPC when r-CO₂ is lost through the reactor outlets after regeneration, while they differ for a system equipped for r-CO₂ recovery and recycle.

$$\text{utilization (\%)} = \frac{\dot{n}_{\text{CO}_2\text{total}} - \dot{n}_{\text{CO}_2\text{unused}}}{\dot{n}_{\text{CO}_2\text{total}}} \times 100 \quad 2.8$$

First, the system single-pass conversion to CO₂R products was optimized by altering the CO₂ feed flow rate at a constant current density of -200 mA cm^{-2} . The idea is that by limiting the amount of CO₂ supplied to the cell while keeping constant the amount of electrons available for reduction (i.e. fixed current density), a greater proportion of the feed CO₂ is used to form products instead of bypassing the cell without being reduced (for more details see Section 2.3). As expected, decreasing the flow rate from 10 mL min^{-1} to 1.25 mL min^{-1} increased the SPC to reach a value of $(29 \pm 3)\%$ at 1.25 mL min^{-1} (Figure 2.9a), which is consistent with the fact that a higher proportion of the feed CO₂ is reacting at lower flow rates. However, surprisingly, decreasing the flow rate to 1 mL min^{-1} did not lead to a higher SPC, which instead plateaued around 29%. This was ascribed to the insufficient amount of CO₂ available for reaction at the

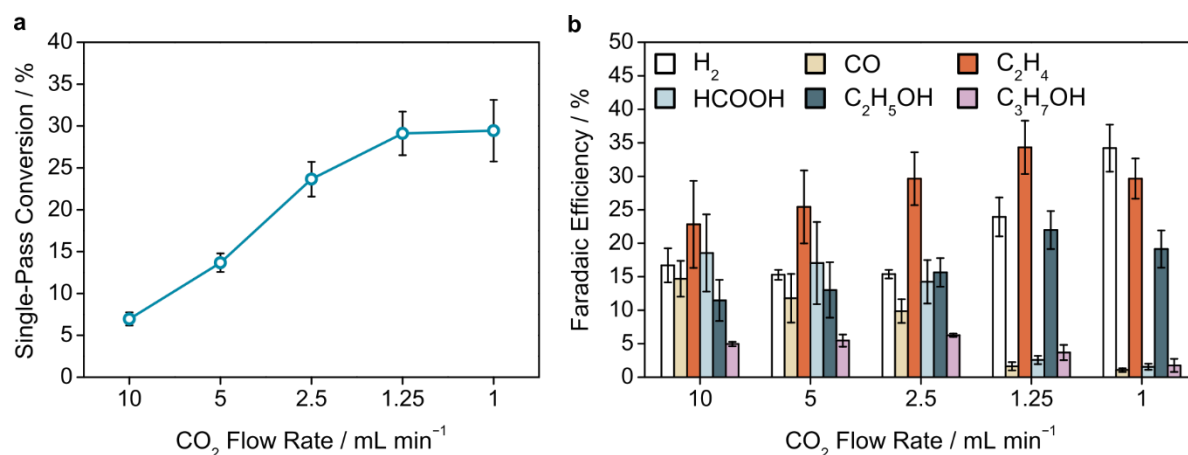


Figure 2.9 Effects of varying the CO₂ flow rate on (a) single-pass conversion, and (b) selectivity. The data were obtained after performing each electrolysis for 30 min at -200 mA cm^{-2} with a $0.05 \text{ M H}_2\text{SO}_4 / 3 \text{ M KCl}$ catholyte. The error bars represent the standard deviation from the mean for three different electrodes.

electrode surface, resulting in surplus electrons being used to drive H₂ evolution instead of CO₂ reduction. An interesting dependence of selectivity on the CO₂ flow rate was also observed. When decreasing the flow rate, the selectivity for C₂₊ products increased at the expenses of C₁ product formation (Figure 2.9b). The highest FEs for ethylene, (34 ± 4)%, and ethanol, (22 ± 3)%, were obtained at 1.25 mL min^{-1} , with a C₂₊/C₁ ratio of 14, while at 10 mL min^{-1} this ratio has a value of 1. In addition, the predominance of HER over CO₂R starts to be evident at 1 mL min^{-1} , supporting the hypothesis of a threshold flow rate below which the low availability of CO₂ cannot support an efficient CO₂R. To help rationalize the change in selectivity with the decreasing CO₂ flow rate, the CO₂, CO and C₂H₄ concentrations were plotted as a function of conversion (Figure 2.10). The trend showed that as the concentration of CO₂ was lowered (i.e. decreasing flow rate/increasing conversion), the concentration of CO decreased after reaching a maximum around 15% SPC, while the concentration of C₂H₄ increased progressively. This concentration profile is typical for a series reaction (i.e. a process in which the formation of the final product, ethylene, depends on the previous accumulation of an intermediate, CO) and is in line with the conversion of CO₂ to C₂ products via CO as an intermediate.⁶⁸ A second important factor to consider when varying the feed CO₂ flow rate is the trade-off between conversion and productivity of the system, where the productivity is

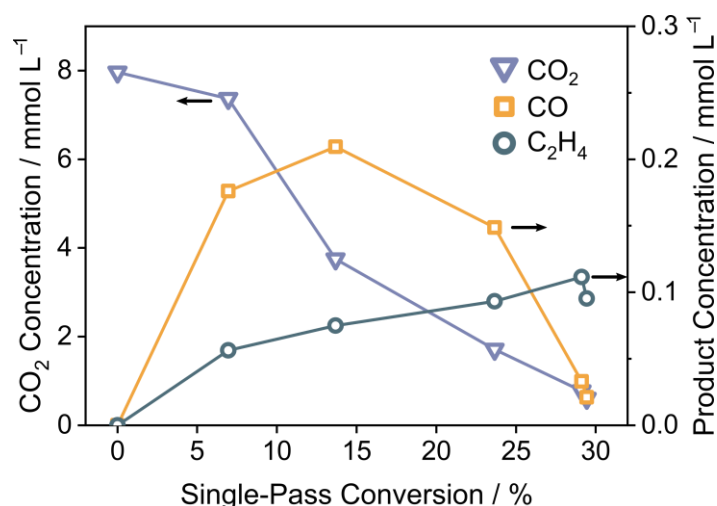


Figure 2.10 Concentration of reactant (CO₂), intermediate (CO) and product (C₂H₄) as a function of single-pass conversion for an electrolysis at -200 mA cm^{-2} . [CO] decreases while [C₂H₄] increases with increasing SPC, which is in line with a series reaction that has CO as the intermediate. The concentration values refer to the amount of each species in the gas volume injected into the gas chromatograph (GC) for analysis. See Chapter 6 for more details on gas product quantification.

defined as the amount of CO₂ reduced to CO₂R products per minute for a given geometric catalyst area.¹⁵⁶ The results (Figure 2.11) showed that the maximum productivity ($1.3 \text{ mg CO}_2 \text{ min}^{-1} \text{ cm}^{-2}$) was achieved at the lowest conversion point (7%), while when the conversion increased to the highest value (29%), the productivity more than halved ($0.54 \text{ mg CO}_2 \text{ min}^{-1} \text{ cm}^{-2}$). This tendency of decreasing productivity with the concomitant increase in conversion is in line with previous reports.^{157,158} This consideration identifies an optimal feed flow rate for a CO₂R electrolyzer to target a specific productivity-conversion point and therefore reaching a maximum SPC is not always the best option if productivity is significantly lowered.

Long term electrolysis

The electrolyzer's ability to operate at the highest conversion point over long periods was assessed (Figure 2.12). For the entire duration of the experiment (8 h) the FEs for all products were stable (Figure 2.12a) and by analyzing analyte samples with protonic nuclear magnetic resonance (¹H NMR) the absence of crossover of any liquid products to the anodic compartment was confirmed, supporting the compartmentalization ability of the BPM. The

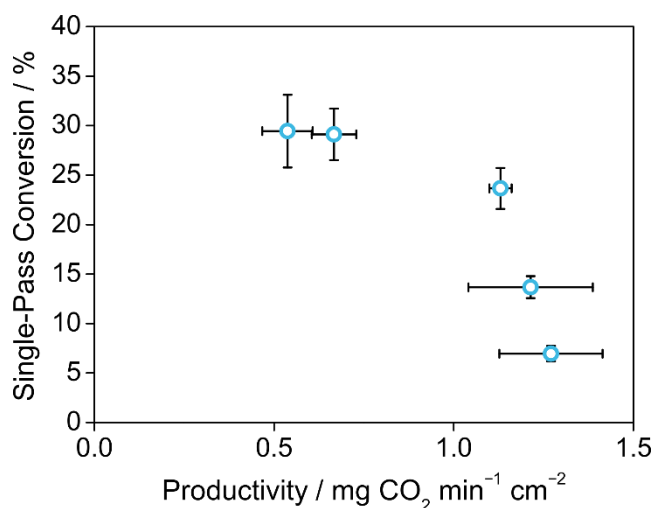


Figure 2.11 Single-pass conversion as a function of the productivity of the reactor. The 30 min electrolysis experiments were carried out in 0.05 M H₂SO₄ / 3 M KCl at -200 mA cm^{-2} with increasing CO₂ feed flow rate (from 1 to 10 mL min⁻¹, from left to right). The correlation shows a clear trade-off between conversion and productivity. All measurements were for 1 cm² geometric area electrodes. The error bars represent the standard deviation from the mean for three different electrodes.

positive effects of employing a bipolar membrane are also shown through pH and K⁺ concentration monitoring. It is noteworthy that the acidity of the catholyte (pH 1) could be maintained for the whole duration of the test simultaneously with an extremely basic anolyte (pH 14, Figure 2.12b). In addition, inductively coupled plasma-mass spectroscopy (ICP-MS) enabled precise [K⁺] measurement in both compartments showing that there was no significant potassium crossover (Figure 2.12c). The reactor could maintain a cell potential of -5.4 V with an average SPC of 26% with respect to carbon products (Figure 2.12d).

The BPM-based electrolyzer was compared with an equivalent reactor equipped with a CEM (Nafion), acid anolyte (1 M H₂SO₄) and an acid-stable IrO_x anode to prove that the results presented in this chapter are applicable to acidic catholytes, irrespective of the membrane/anolyte/anode used (Figure 2.13). As the catholyte composition was kept constant, the CO₂ regeneration took place in both cases, but the cell voltage of the CEM system was significantly lower than that of the BPM system ($|E_{\text{cell}}|$ equal to 3.8 V and 4.7 V, respectively). This large voltage penalty can be mainly ascribed to the water dissociation taking place at the

interlayer of the membrane, which is typical for most commercially-available BPMs, and partially to Ohmic losses due to other resistive components.¹⁵⁹

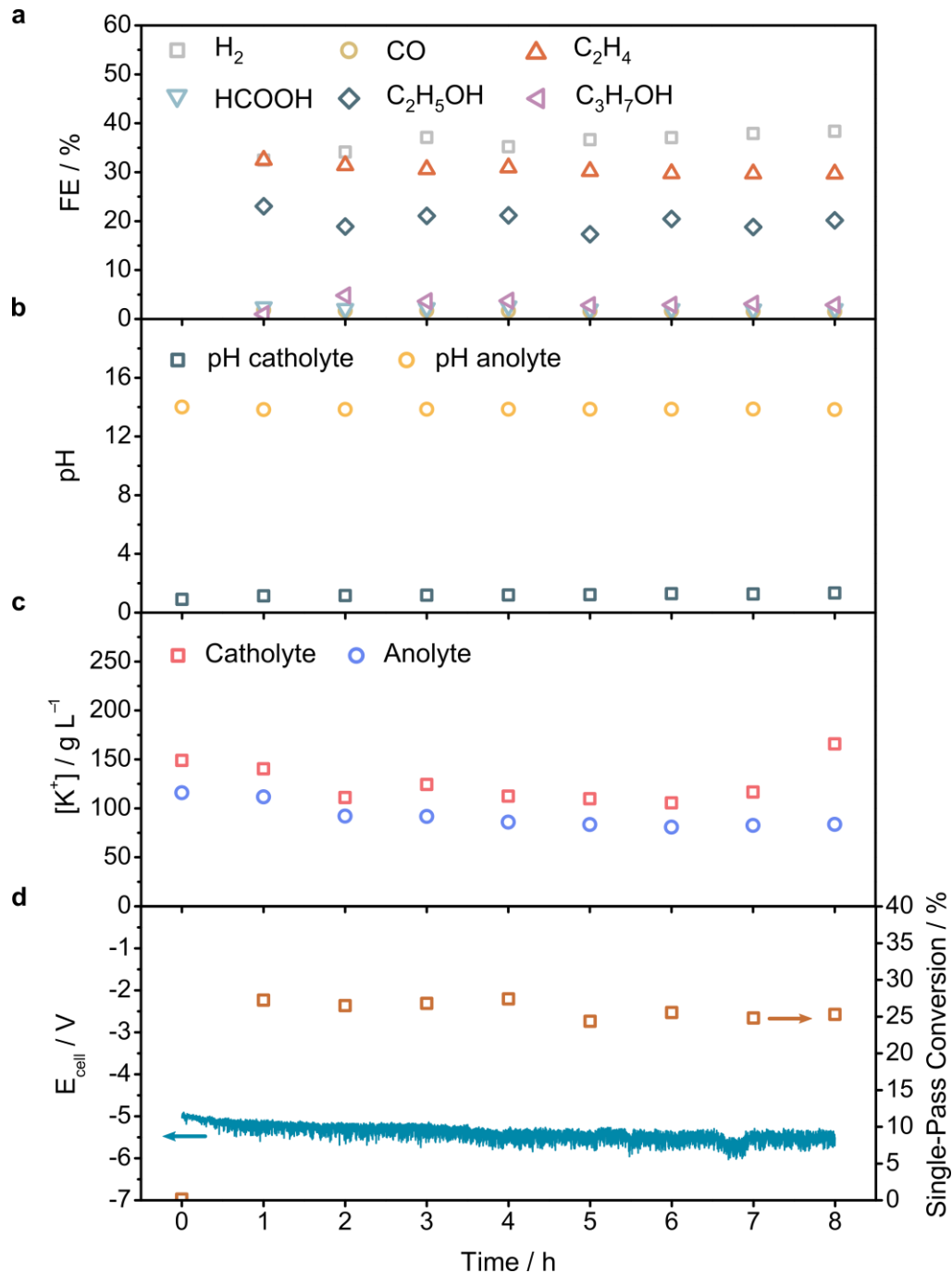


Figure 2.12. Stability test performed at -200 mA cm^{-2} with a feed CO₂ flow rate of 1.25 mL min^{-1} , a $0.05 \text{ M H}_2\text{SO}_4 / 3 \text{ M KCl}$ catholyte (100 mL) and a 2.5 M KOH anolyte (100 mL). (a) FE changes for each product; (b) pH stability in catholyte and anolyte; (c) K⁺ concentration in each compartment; (d) cell voltage and SPC values.

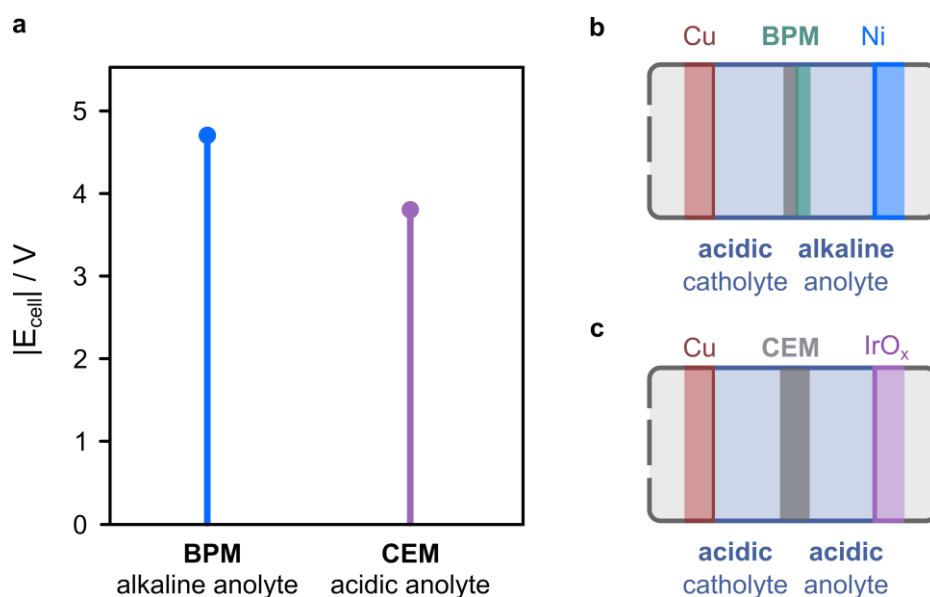


Figure 2.13 (a) Comparison of the cell potential for two different configurations employing either a BPM with alkaline anolyte and a Ni foam catalyst shown in (b) or a Nafion system with acidic anolyte and an IrO_x catalyst shown in (c). In each case the catholyte (0.05 M H₂SO₄ / 3 M KCl) and cathode (Cu NPs) were the same. The CEM system employed 1 M H₂SO₄ as the anolyte seeing as K⁺ ions cannot be used as they will cross the membrane and change the catholyte composition over time.

2.2.4 Physical model

After establishing a robust acidic system able to operate at good selectivity and conversion values over extended periods, efforts were made to obtain a better understanding of the different paths followed by feed CO₂ and r-CO₂ that lead to either reaction at the cathode and/or release from the electrolyzer. Even though previous reports studying acidic CO₂R suggest that re-reaction of r-CO₂ can take place,¹³⁴ consequently increasing the SPC, the experimental data gathered here indicated that re-reaction of r-CO₂ was not dominant, as suggested by the plateau reached by the SPC at low flow rates due to insufficient CO₂ supply. If r-CO₂ was able to reach the cathode and react, the amount of CO₂ would be enough to consume most of the available electrons resulting in efficient CO₂R even at flow rates lower than 1.25 mL min⁻¹ and the SPC would keep increasing. Consequently, in this case, the lower limit of flow rates would be attained only when the feed CO₂ is not enough to actively sustain CO₂R. A one-dimensional

diffusion-reaction model based on previous reports was built to estimate the pH and resulting CO₂ concentration profiles under reaction conditions (Figure 2.14, details in Section 6.7).^{134–}

¹³⁶ Within the 100 μm-thick diffuse layer the pH varies from a value of almost pH 14 at the cathode surface to less than pH 1 at the boundary with the bulk. Simultaneously, the CO₂ concentration profile follows a similar and opposite trend: [CO₂] is almost zero at the cathode surface (equilibrium completely shifted towards carbonate) and then it increases concomitantly with the gradual decrease in pH until the bulk concentration value is attained at the outer edge of the diffuse layer (aqueous saturation value corrected for the ionic strength). This clearly shows that the strongly alkaline environment close to the catalyst is responsible for the transient (bi)carbonate formation and that CO₂ regeneration occurs within the diffuse layer, approximately 35 μm from the surface. The results evidence that although r-CO₂ diffusion towards the cathode for reduction could be possible, this is in competition with reaction with OH⁻ to form (bi)carbonate once more. The hydroxide concentration is high close to the cathode surface, acting as a barrier that prevents r-CO₂ reduction, therefore it is more likely for the r-

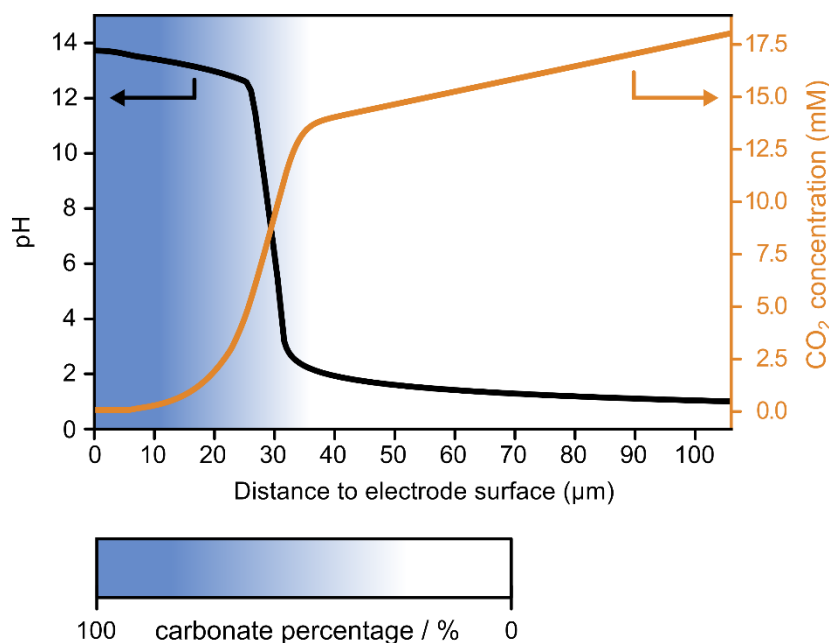


Figure 2.14 Results of the one-dimensional diffusion-reaction model estimating the pH and CO₂ concentration profiles within the 100 μm-thick diffuse layer at -200 mA cm^{-2} in a 0.05 M H₂SO₄ / 3 M KCl catholyte. The blue gradient is a visual guide to show how the percentage of CO₂ converted to carbonate species varies with the distance from the electrode.

CO₂ to degas from the catholyte solution instead. In order to validate this hypothesis and gain a more comprehensive picture of the conversion efficiency of the reactor, a series of tests was developed to analyze the composition of the gas outlets of the electrolyzer.

2.2.5 CO₂ utilization and recycling

The electrolyzer features two gas outlets. The first, termed as the direct outlet, is located at the back of the GDE and collects unreacted feed CO₂ and gas products, while the second, identified as the indirect outlet, is contained within the flowing catholyte solution coming out of the cell (catholyte outlet) and gathers r-CO₂ together with any gas product that degases from the electrolyte (Figure 2.15). The composition of the gas streams vented from each outlet were analyzed in absence of current and under catalytic conditions to determine the distribution of CO₂ and gas products among them (Figure 2.16).

First, the amount of CO₂ coming out from each outlet was monitored under idle conditions (0 mA cm⁻²) and under working conditions (-200 mA cm⁻²) while keeping constant the feed CO₂ flow rate at 1.25 mL min⁻¹, the value associated with the highest SPC (Figure 2.16a). Without current passing through the system, the majority of the feed CO₂ was found at the direct outlet (93%), while the rest crossed through the GDE and was vented from the indirect outlet (7%). Instead, under catalytic conditions, the situation is completely different. At -200 mA cm⁻² only a small portion of the feed CO₂ was retrieved at the direct outlet (2%), an indication that reactant bypassing of the cell was low, while the rest was obtained at the indirect outlet (66%). The missing portion of the total feed CO₂ (32%) corresponds to the fraction reduced to carbon products (i.e. CO₂ utilization), which is in agreement with the SPC value (29%) found during the flow rate study in Section 2.2.3. It is worth noting that, in both cases, the combined amounts of CO₂ retrieved at the outlets and CO₂R products accounted for all the carbon atoms injected as feed CO₂ into the cell, therefore providing a closed carbon mass balance. Moreover, the composition of the two streams under catalytic conditions (Figure

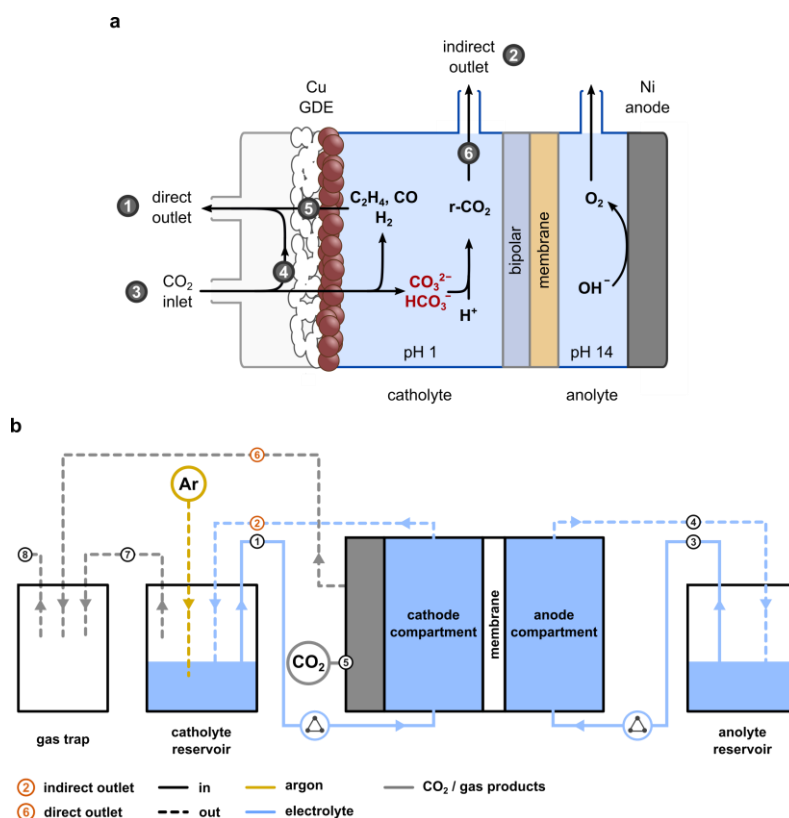


Figure 2.15 (a) Schematic representation of the cell (cross section) showing the outlets of the reactor, with the different pathways for the feed CO₂ and r-CO₂ – (1) direct outlet, (2) indirect outlet, (3) CO₂ inlet, (4) CO₂ that bypasses the cell without crossing the GDE, (5) products release, (6) r-CO₂ release. (b) Gas-fed flow cell setup: (1) catholyte inlet, (2) catholyte outlet containing the indirect gas outlet, (3) anolyte inlet, (4) anolyte outlet, (5) CO₂ inlet, (6) direct outlet, (7) catholyte reservoir outlet transferring the gases carried by the indirect outlet to the gas trap, (8) path to GC.

2.16b) showed that the carbon gas products (CO and C₂H₄) were exclusively vented from the direct outlet, together with the majority of the evolved H₂ and a small amount of CO₂, while the liquid products accumulated in the catholyte. Instead, the output of the indirect outlet was a high purity r-CO₂ stream with only small quantities of hydrogen (2%). This is ideal as the indirect CO₂ stream is suited to be directly reinjected into the electrolyzer for reduction, since separation from CO₂R products and H₂ is not necessary. The ability of the system to recycle and re-use the r-CO₂ was tested by modifying the setup configuration (Figure 2.17a). Essentially, instead of having the feed CO₂ going directly from the gas bottle to the CO₂ inlet of the cell, the gas was first bubbled in the catholyte reservoir, then the gas outlet of the reservoir was connected to the CO₂ inlet of the reactor instead of going into the gas trap. In

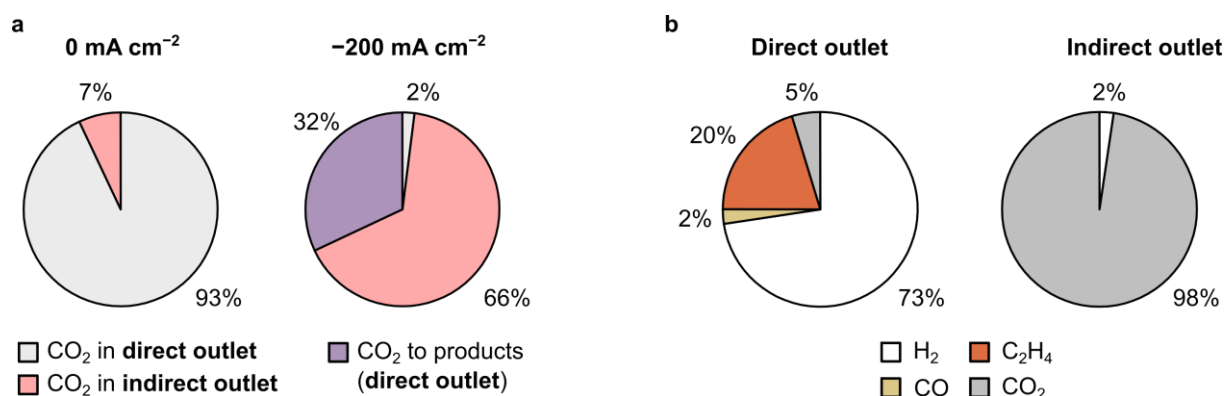


Figure 2.16 (a) The CO₂ distribution under working and idle conditions, the whole pie represents the feed CO₂ supplied to the cell. Conditions: 30 min electrolysis, CO₂ flow rate of 1.25 mL min⁻¹, electrolyte solution of 0.05 M H₂SO₄ / 3 M KCl. (b) Stream composition (concentrations) of the direct outlet (left) and indirect outlet (right) under electrocatalytic conditions (1.25 mL min⁻¹ CO₂ flow rate, -200 mA cm⁻²). The percentages are given as molar fractions.

this way, the output of the indirect outlet was effectively re-injected into the cell. With no applied current, the feed CO₂ saturated the headspace of the catholyte reservoir before being injected into the cell through the CO₂ inlet (Figure 2.17b). Under working conditions, r-CO₂ was regenerated in the electrolyte close to the cathode, which was then transported to the catholyte reservoir where it degassed and mixed with the feed CO₂ (Figure 2.17b). With flowing current, the molar flow of the CO₂ vented from the direct outlet ($\dot{n}_{\text{CO}_2\text{unused}}$) was monitored as a function of the feed flow rate, initially set at 1.25 mL min⁻¹, since $\dot{n}_{\text{CO}_2\text{unused}}$ is directly linked to the CO₂ utilization (Figure 2.18a, Equation 2.8). The first point of the graph (time = 0) is representative of the conditions after CO₂ saturation of the system with no applied current ($\dot{n}_{\text{CO}_2\text{total}} \equiv \dot{n}_{\text{CO}_2\text{unused}} = 743 \text{ nmol s}^{-1}$, 0% CO₂ utilization). After starting the electrolysis with a constant feed flow rate, $\dot{n}_{\text{CO}_2\text{unused}}$ saw a sharp decrease as CO₂ was reduced to products; however, over time, an increase could be seen due to a gradual accumulation of r-CO₂ in the system, which added to the feed CO₂ and increased the amount of unused reactant, as the fraction reduced to products does not vary because of the constant current density. This resulted in a stable CO₂ utilization of ~60% at 1.25 mL min⁻¹. Remarkably, lowering the feed CO₂ flow rate lead to a decrease in $\dot{n}_{\text{CO}_2\text{unused}}$ and an increase in CO₂ utilization, meaning that the recycling

setup allows to push the system past the previous CO₂ flow rate limit of 1.25 mL min⁻¹ shown in Figure 2.9 without losing selectivity for CO₂R (Figure 2.18b). This was possible thanks to the additional flow provided by the r-CO₂, which maintained a constant effective inlet flow rate of CO₂ for reaction even if the feed CO₂ was lowered. The CO₂ utilization could be maximized to a remarkable value of 88% ($\dot{n}_{\text{CO}_2\text{unused}} = 40 \text{ nmol s}^{-1}$) with a feed flow rate of 0.4 mL min⁻¹, demonstrating that r-CO₂ recycling could be used to increase the overall utilization of CO₂.

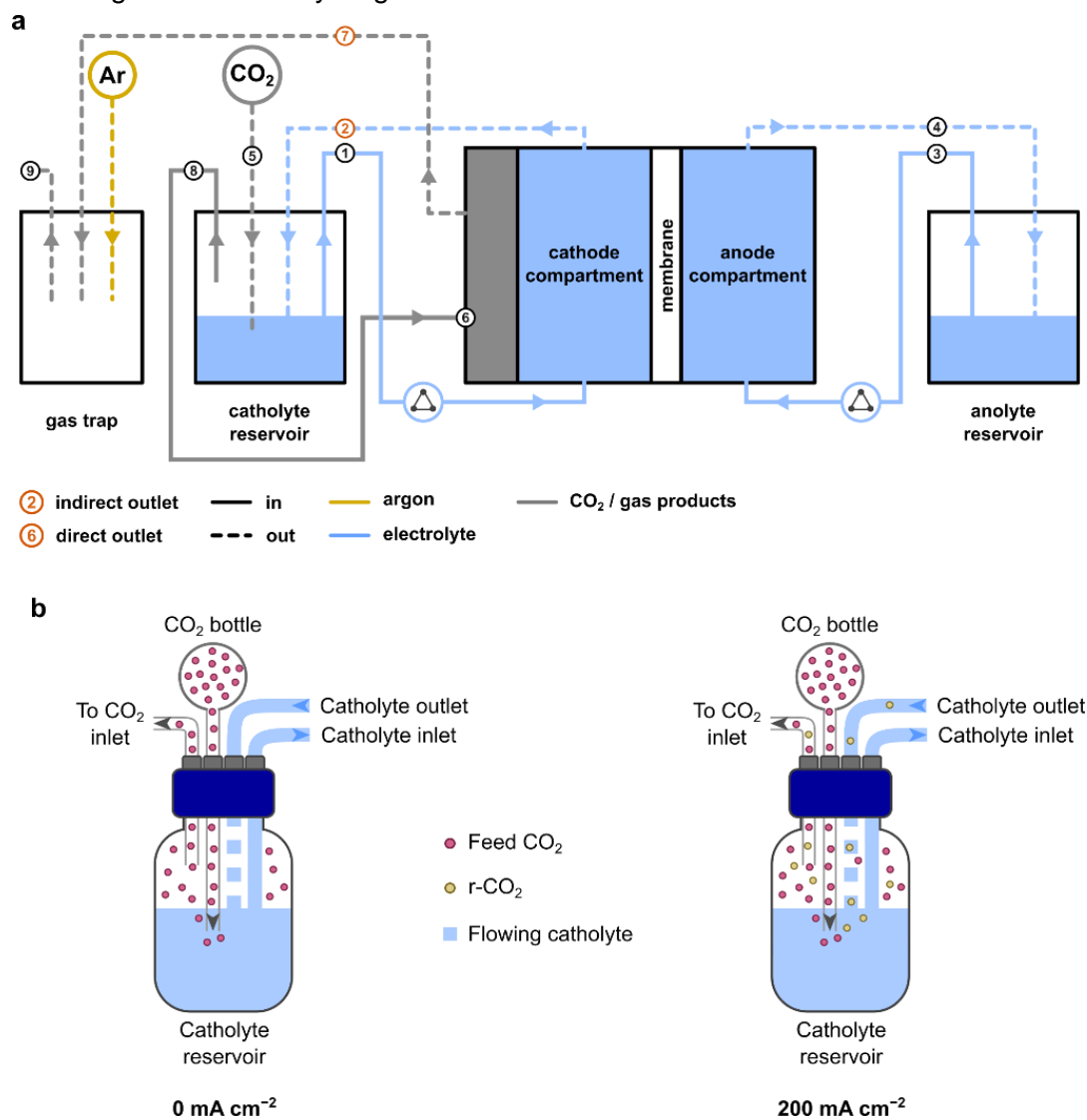


Figure 2.17 (a) Gas-fed flow cell in recycling configuration: (1) catholyte inlet, (2) catholyte outlet containing the indirect gas outlet, (3) anolyte inlet, (4) anolyte outlet, (5) feed CO₂, (6) CO₂ inlet, (7) direct outlet, (8) catholyte reservoir outlet transferring the feed CO₂ and the gases carried by the indirect outlet to the CO₂ inlet, (9) path to GC. (b) CO₂ pathways inside the catholyte reservoir in the recycling configuration under idle (0 mA cm⁻²) and working (-200 mA cm⁻²) conditions.

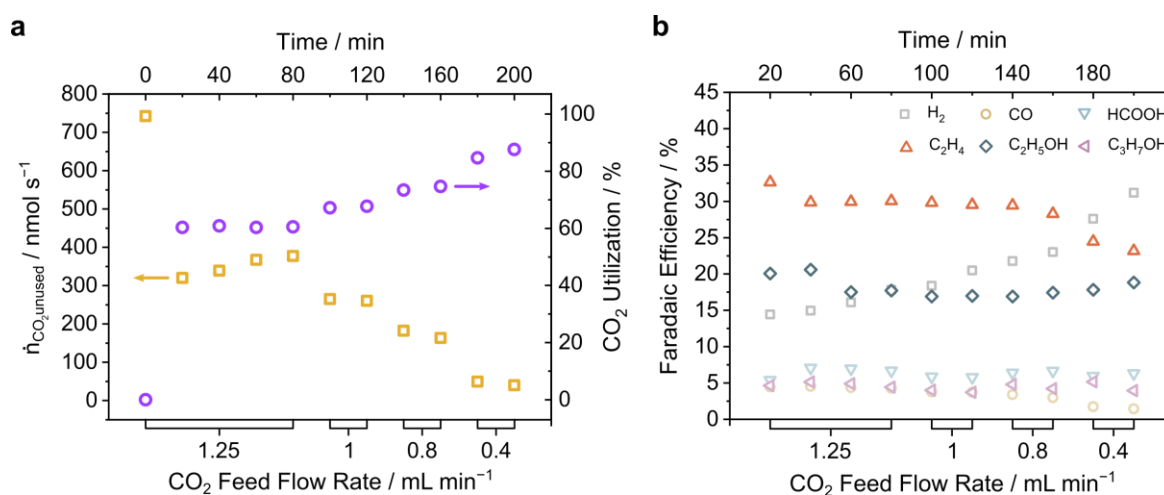


Figure 2.18 (a) Results of the recycling test: the CO₂ molar flow leaving the cell through the direct outlet (yellow squares) and the CO₂ utilization (purple circles) were monitored over time during electrolysis at -200 mA cm^{-2} with the recycling configuration. (b) The product selectivity for the CO₂ recycling test was constant for the duration of the experiment and only deviated slightly at 0.4 mL min^{-1} , which was attributed to a limit with instrumentation accuracy at this flow rate.

2.3 Discussion

In the previous sections, CO₂ utilization was improved in an acidic system by avoiding permanent reactant loss through simple CO₂ recovery and recycling.

Compared to bipolar membranes, cation and anion exchange membranes are more developed and their application in CO₂R is well-established. However, the characteristics of the former make them attractive components for CO₂ electrolysis. The stability of the electrolyte over time is crucial to not alter the reaction conditions that might modify the performance of the reactor, and BPMs effectively seal one cell compartment from the other by not allowing any species to cross.¹⁴⁶ Here, employing a BPM as compartment separator resulted in a constant pH and electrolyte composition on both sides of the cell for at least 8 h, leading to stable product selectivity, cell voltage, and SPC. The membrane also allowed to couple the acid catholyte with an alkaline anolyte, which is usually preferred because OER is favored at high pH^{116,160} and Ni-foam could be used as an inexpensive anode catalyst. The most important drawback

of implementing a BPM is the high voltage penalty introduced by the water dissociation reaction taking place between the CEL and the AEL, which resulted in a very negative cell potential of -4.7 V. Despite this, it has been shown recently that the overpotential required for the water dissociation can be significantly reduced by introducing a catalyst in the interlayer of the membrane, which could limit voltage penalties in the near future.^{143,161,162}

The SPC is one of the parameters that can be evaluated when considering the conversion efficiency of a flow reactor. It is a sensible variable that can be altered by several factors such as (i) the reaction rate (i.e. current density), (ii) the flow rate of feed CO₂ and (iii) the type and quantity of generated products. (i) Increasing the applied current density while keeping the feed CO₂ flow rate constant has the effect of boosting the SPC because more available electrons result in a larger fraction of the feed CO₂ that is converted to products (assuming constant selectivity), leading to higher conversions and less unused CO₂. (ii) For a given product distribution at constant current density, lowering the flow rate increases the SPC. As the SPC represents the fraction of the total feed CO₂ converted to products, if the CO₂ supplied to the cell diminishes while the amount reduced remains the same (due to constant current density), the CO₂-to-products portion increases with respect with the total available CO₂, boosting the SPC (Figure 2.19). In the situation analyzed in Section 2.2.3, H₂ formation increases significantly at 1 mL min⁻¹, suggesting that the supplied CO₂ was not sufficient to consume all of the available electrons and that it was entirely converted to either CO₂R products or (bi)carbonate, while the excess current was used to reduce water into H₂. Increasing CO₂ availability at the electrode, which would result in higher CO₂R selectivity and SPC, requires reduction of r-CO₂ and/or a lower degree of (bi)carbonate formation, two pathways that do not seem viable in the presented system. (iii) The influence of the product distribution is a consequence of the different amount of hydroxide ions formed for each product during CO₂R, which will determine how much CO₂ is converted to transient (bi)carbonate species. For example, in the case of a reactor completely selective towards CO, two OH⁻ ions are formed per molecule of CO generated, meaning that for every CO₂ that gets reduced to

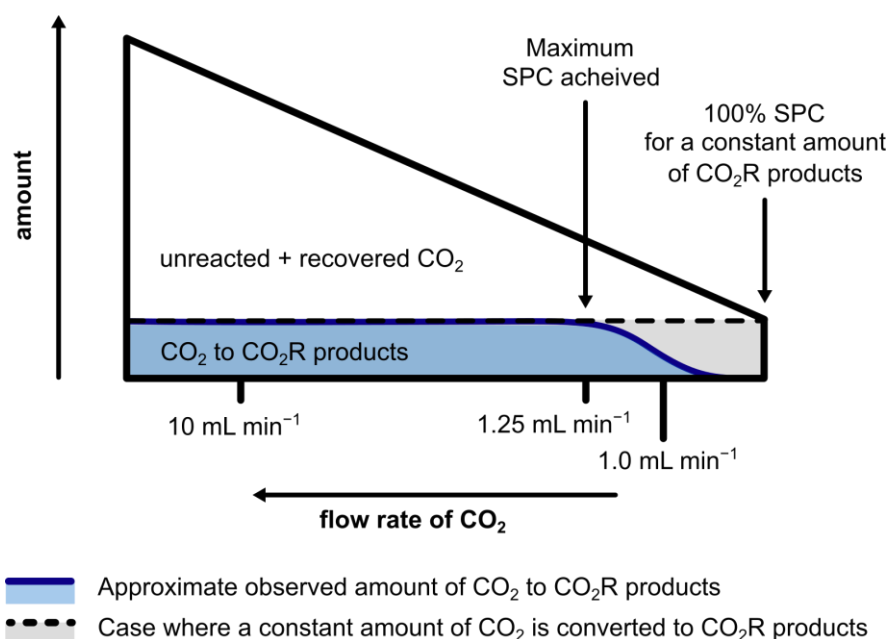


Figure 2.19 Visualization of the SPC at different feed CO₂ flow rates. As the amount of CO₂ converted to products decreases at low flow rates due to the increasing H₂ production, the SPC does not increase as it theoretically would for a constant product distribution.

CO, another one is transformed to CO₃²⁻ (a reaction that requires two hydroxide ions). Therefore, the maximum SPC that can be attained in this scenario (where it is assumed that r-CO₂ does not re-react at the cathode) is 50%, with half of the feed CO₂ being reduced to CO and the other half being transformed into carbonate. When considering multicarbon products the situation becomes even more unfavorable. For an electrolyzer having unit selectivity towards ethylene, the highest achievable SPC is only 25%, due to the fact that generating one ethylene molecule (which requires two CO₂ molecules) is accompanied by twelve OH⁻ ions formation. Thus, for every two CO₂ molecules fixed into ethylene, six others will form carbonate. Acidic conditions open the possibility to go past these limits thanks to CO₂ regeneration from carbonate, but this benefits the SPC only if the r-CO₂ is able to re-react at the cathode to give CO₂R products. Considering the case in exam, the SPC calculated values reflect how the selectivity is spread among several carbon products and that the product distribution changes when the feed flow rate is modified. However, using SPC as the only variable describing the conversion efficiency of the reactant would be misleading because it does not provide a complete overview of the reactor performance. For example, it was shown

that an important compromise exists between SPC and productivity of a system, therefore the findings presented here highlight that aiming at 100% SPC is not a prerogative, especially if a low productivity negatively affects the output of a specific reactor. In addition, when the r-CO₂ is recycled, an overall high reactant utilization (88%) could be achieved with an SPC of 29%, highlighting that high conversions can be attained even when the SPC is not maximized.

The feed CO₂ flow rate, other than affecting conversion and productivity, has a strong influence on the product distribution: the selectivity can be switched from monocarbon (CO, HCOOH) to multicarbon products (C₂H₄, C₂H₅OH) by lowering the flow rate. Having an electrolyzer selective towards C₂₊ products is preferred due to the higher added value of chemicals like ethylene, ethanol and propanol. For the case presented in Figure 2.9, highest formation of C₂₊ products (60%) was obtained at a flow rate of 1.25 mL min⁻¹, which is concomitant with the maximum SPC achieved for the system. Establishing a r-CO₂ recycling setup would be beneficial as the SPC value can then be adapted to obtain the highest productivity and/or best product distribution, while all of the feed CO₂ will be eventually utilized.

Analyzing the gas outputs of the reactor is fundamental to obtain a global overview of the system and should be performed in every CO₂R-related study. The distribution of CO₂ among the direct and indirect outlets during electrolysis at 1.25 mL min⁻¹ evidenced that almost all of the feed CO₂ crosses the GDE and is converted to either (bi)carbonate species or reduction products. With the recycling setup in place, the r-CO₂ generated from the carbonate species is reinjected into the cell for reduction, hence the output of the indirect outlet is looped in the system instead of being lost to the environment. This means that during recycling, the direct outlet is the only gas exit point of the electrolyzer, collecting unused feed CO₂, unused r-CO₂ and reaction products. As the feed flow rate is lowered it is simultaneously compensated by the flow of r-CO₂ accumulating in the system, leading to higher utilization since the r-CO₂ is not additional reactant but rather feed CO₂ that is recirculating in the system. Moreover, as utilization increased, less unused CO₂ exited from the direct outlet, resulting in a concentrated stream of gas products. This solution elegantly avoids downstream CO₂/product separation

through processes such as amine-based capture, which typically dominates the energy consumption of the product purification.¹⁶³ A proposed scheme showing how the recycling setup could be implemented in a larger system is illustrated in Figure 2.20. Here the feed CO₂ is constantly mixed with r-CO₂ in a mixing unit, then the resulting stream is injected into the cell stack through the CO₂ inlet. The inlet flow rate can be modulated using a feedback loop relying on a flow detector positioned at the direct outlet to maintain an operational inlet flow rate for optimal productivity/SPC/utilization conditions.

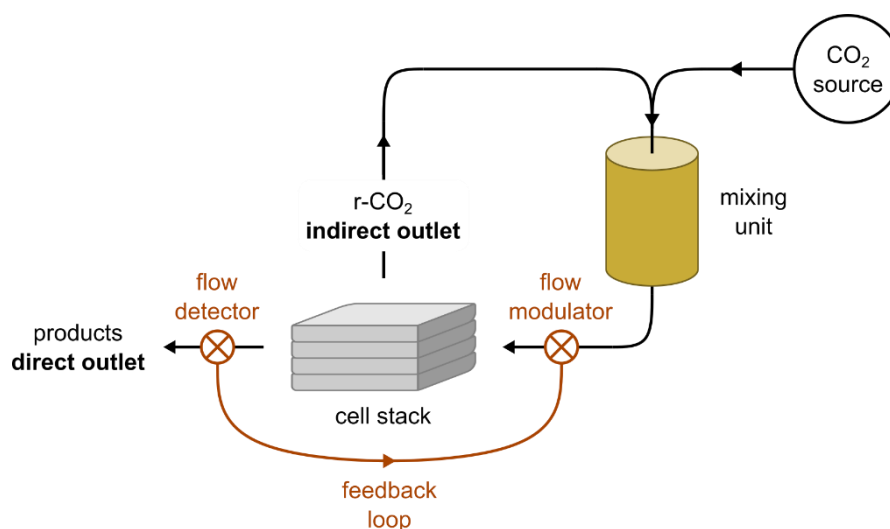


Figure 2.20 Schematic of the potential r-CO₂ recycle in a cell stack setup.

2.4 Conclusions

The acidic CO₂R system presented here displayed a high C₂₊ selectivity with continuous internal CO₂ regeneration and recycling. Employing a BPM enabled long term stability and robustness of the setup, evidenced by the absence of product and contaminant crossover and the pH gradient that could be maintained across the cell even with an acidic catholyte and an alkaline anolyte. With low flow rates of CO₂ at the cathode, the selectivity for C₂₊ products was above 60%, leading to a single-pass conversion efficiency to CO₂R products of (29 ± 3)%. Importantly, the CO₂ regenerated from (bi)carbonate (r-CO₂) could be recovered as an almost product-free stream at the indirect outlet and effectively recycled to achieve a high overall

utilization (> 85%), with an almost pure product stream being obtained at the direct outlet. It was shown that the recycling is possible independently of the membrane used, making it compatible with the more established CEM-based systems. Furthermore, even with non-unity single-pass conversion, the overall utilization of CO₂ could be maximized through recycling of r-CO₂ and flow rate modulation, reducing the need for energy-intensive downstream separation procedures, observations that will prove useful in the future development of CO₂R reactors. As devices move towards operation at high conversions, cell modifications to improve gas management, CO₂ recovery and recycling will become more important. In particular, careful evaluation of crucial parameter trade-offs, like that between conversion and productivity, will be significant.

The presented system still suffers from a high cell voltage that would not be suitable for industrial scale-up and even the energy requirements of more common CEM-based electrolyzers are too high for a cost-efficient process. In the next chapter, a strategy to lower the overall cell voltage will be analyzed.

Chapter 3

Cell Voltage Optimization

3.1 Introduction

Industrial application of CO₂ electrolysis requires efficient, high-rate generation of carbon products. Critical parameters to consider for the scale-up of CO₂ electrolyzers are the current density, selectivity towards C₂₊ products, CO₂ utilization, and the cell potential. In the previous chapter, the FE_{C₂₊} and the CO₂ utilization were optimized in acidic conditions, but the cell voltage remained an important obstacle in the way of cheap CO₂ electrolysis. The electricity input has been identified as the largest barrier to implementation of CO₂ conversion at large scale.^{164,165} Therefore, improving the cell voltage has the potential to reduce cost and improve access to renewable fuels able to compete with fossil-derived ones. As previously described, CO₂R has been traditionally carried out in H-cells where the low solubility of CO₂ in water (ca. 33 mM)¹⁶⁶ results in mass transport limitations that restrict operations to low current densities (< -50 mA cm⁻²).¹⁶⁷ Gas-fed flow cells provided a marked performance improvement by allowing to achieve higher current densities (> -150 mA cm⁻²) at moderate cell voltages by reducing the length that CO₂ has to diffuse to reach the cathode.^{167,168} To be suitable for commercialization, CO₂R electrolyzers have to operate with an E_{cell} lower than 3 V at industrially relevant current densities (> -200 mA cm⁻²).^{169,170} However, there are not many examples of systems able to attain these conditions. A notable exception is a zero-gap

electrolyzer for CO₂-to-CO conversion coupled with anodic OER (3 V at -300 mA cm⁻²).¹⁷⁰ Another article reports a reactor carrying out bicarbonate-to-CO at the cathode and H₂ oxidation at the anode (2.3 V at -220 mA cm⁻²).¹⁷¹ However, if the energy spent to produce H₂ via water electrolysis is accounted for, the efficiency of this process diminishes. In Chapter 2, acidic CO₂R coupled with alkaline OER was carried out in a gas-fed flow cell electrolyzer equipped with a bipolar membrane with a high |E_{cell}| of 4.7 V (-200 mA cm⁻²). The BPM introduced a significant voltage penalty to the system, but even when it was replaced with a relatively less resistive Nafion membrane the cell voltage remained high (3.8 V at -200 mA cm⁻²). Nafion-based flow cells are commonly used to carry out acidic CO₂ electrolysis^{134–136} and to improve the E_{cell} it is imperative to understand which reactor components participate in the overall cell voltage.

The cell potential of a gas-fed flow cell accounts for the voltage contributions required to carry out the cathodic (E_{red}) and anodic (E_{ox}) half-reactions and the voltage drops caused by the presence of catholyte, anolyte (E_{cath} and E_{anol}, respectively) and the membrane (E_m). In general, the electrolyte is needed for charge conduction and as a medium for the electrochemical reactions, but it also introduces a solution resistance from which the E_{cath} and E_{anol} arise.¹⁷² An ion exchange membrane is usually present to avoid mixing of the cathodic-generated H₂ and the anodic-evolved O₂ and also to prevent the CO₂R products from reaching the anode, yet this establishes another resistance leading to a voltage drop across the membrane, E_m.¹⁰³ E_{red} and E_{ox} are dictated by the overpotential required by the respective half-reactions on the specific catalyst employed¹⁰³ and even though they can be optimized to decrease the energy input of the reactor, they will not be discussed as the electrodes will not be modified in the following description. The E_{cell} of such a device can then be optimized by lowering E_{cath}, E_{anol} and E_m (i.e. reducing their resistance), which can be done through alteration of four parameters: (1) type of membrane, (2) electrolyte solution composition, (3) distance between the electrodes, and (4) temperature of the electrolyte solution. (1) Cation exchange membranes allow the transport of cations through electrostatic interactions with the negatively

charged functional groups within their structures (sulfonic acid groups in the case of Nafion).¹⁷³ Depending on the nature of the cation, the ionic bond with the groups varies in intensity and if the interaction is strong a higher voltage is needed to transport the charges, resulting in a high membrane resistance (high E_m).¹⁷⁴ To decrease the voltage drop associated with the membrane, Nafion can be replaced by a separator that offers less resistance to the passage of ions or the membrane can be directly removed from the cell. (2) The concentration and type of the species dissolved in solution influence the resistance of the electrolyte. The nature of the dissolved salts and acids can then be manipulated to decrease E_{cath} and E_{anol} by selecting ions with high molar conductivities and maximizing the ionic strength of the solution. (3) The distance separating the cathode from the anode influences the weight that E_{cath} and E_{anol} have on the overall E_{cell} , because thick layers of electrolyte between the electrodes results in a higher solution resistance and thus an increased voltage drop. Therefore, thin catholyte and anolyte layers would benefit the E_{cell} . Moreover, the benefit is maximized if one or both of the electrolytes are removed from the space between the electrodes, which can be placed directly on the membrane to form membrane electrode assemblies.¹⁷⁵ (4) From a thermodynamic point of view, increasing the electrolyte temperature lowers the cell voltage according to the Nernst equation (Equation 3.1), where E_{cell}^0 is the thermodynamic (or standard) cell voltage, R is the universal gas constant, T is the temperature, n is the number of exchanged electrons, F is the Faraday constant and Q is the reaction quotient. In addition, the conductivity of ionic solutions increases with increasing temperature,⁹⁶ which also contributes to decrease the cell voltage.

$$E_{\text{cell}} = E_{\text{cell}}^0 - \frac{RT}{nF} \ln Q \quad 3.1$$

The following sections describe a strategy to lower the overall cell voltage by modifying the device setup, components, and conditions. By understanding of the sources of voltage drops within the cell, an optimized CO_2R device is presented, able to operate at an industrially relevant current density of -200 mA cm^{-2} with an $|E_{\text{cell}}|$ as low as 2.9 V, one amongst the lowest

reported values to date. The modulus of E_{cell} ($|E_{\text{cell}}|$) is often used to avoid confusion by comparing only positive cell voltage values.

3.2 Results

3.2.1 Gas-fed flow cell

The reported gas-fed flow cell systems that carry out CO_2R in acid generally employ a cation exchange membrane (namely Nafion), an acid catholyte containing alkali metal cations (typically K^+ and Cs^+) and an acid anolyte that can also contain metal salts.^{134–136} A model reactor for this kind of configuration is shown in Figure 3.1. The cell is divided in three compartments: gas channel, cathodic chamber and anodic chamber (Figure 3.1a). CO_2 is supplied through the gas channel and passes through the cathode that is composed of a hydrophobic gas diffusion layer, preventing liquids from entering the gas channel, and a catalyst layer. The CO_2R catalyst is interfaced with the catholyte flowing between the cathode and the Nafion membrane separating the two electrolyte compartments. In the other half-cell, the anolyte flows between the membrane and the anode, which is composed of a catalyst layer deposited on a porous support. The anode is in contact with a back plate that closes the device. Figure 3.1b depicts the full setup of the electrolyzer featuring two separate reservoirs for catholyte and anolyte and a gas trap, which is identical to the setup previously shown in Figure 2.15.

Having established the principal components of a gas-fed flow cell and the possible modifications that can reduce the cell voltage, the next sections will describe the optimization of an acidic CO_2R electrolyzer by adjusting each parameter step by step. The starting configuration of the reactor was the following: a gas-diffusion cathode composed of a polytetrafluoroethylene GDL on which commercial Cu NPs were deposited, a 3 M KCl / 0.05

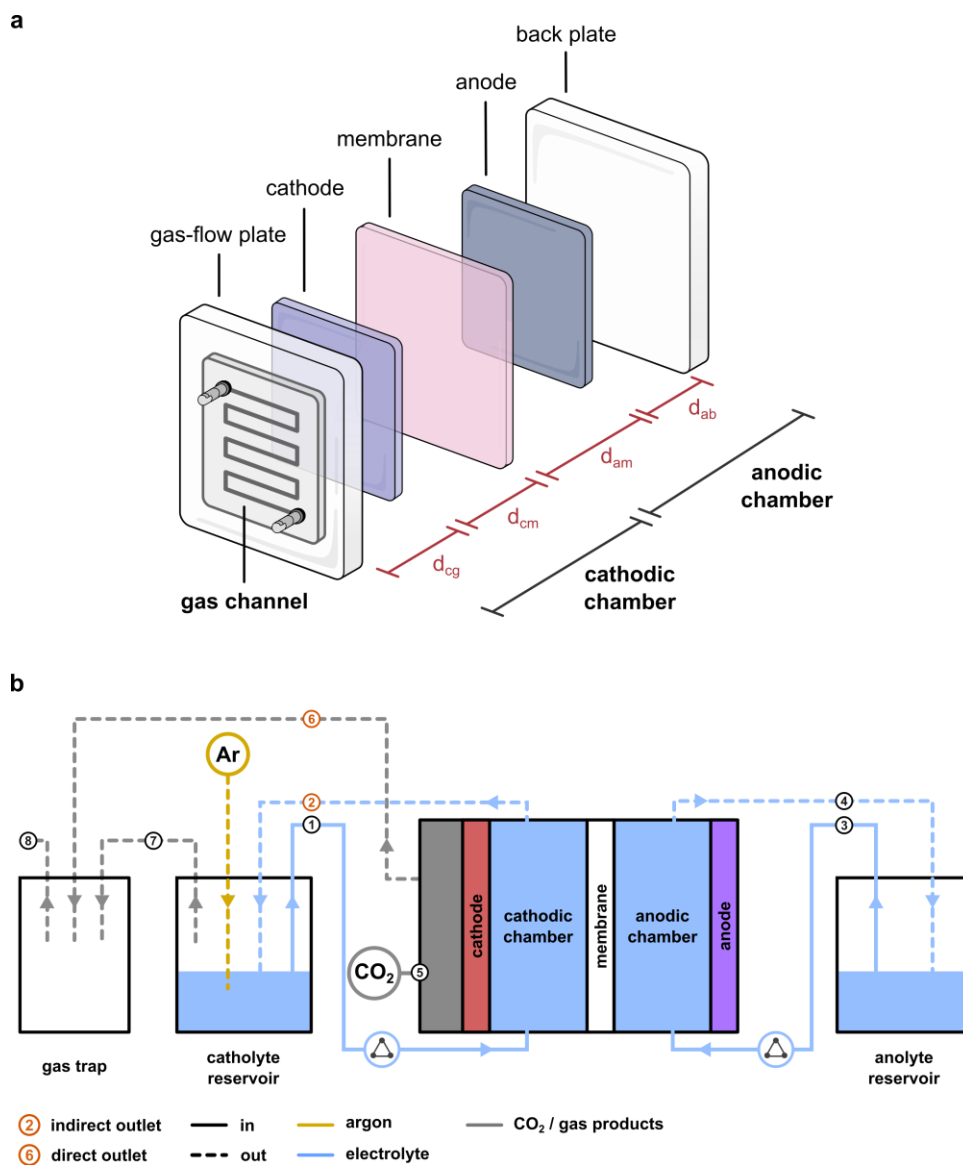


Figure 3.1 (a) Illustration of the main elements composing a gas-fed flow cell. d_{cg} : distance between cathode and gas-flow plate; d_{cm} : distance between cathode and membrane; d_{am} : distance between anode and membrane; d_{ab} : distance between anode and back plate. (b) Gas-fed flow cell full setup: (1) catholyte inlet, (2) catholyte outlet containing the indirect gas outlet, (3) anolyte inlet, (4) anolyte outlet, (5) CO₂ inlet, (6) direct outlet, (7) catholyte reservoir outlet transferring the gases carried by the indirect outlet to the gas trap, (8) path to GC.

M H₂SO₄ catholyte (pH 1), a CEM (Nafion), a 1 M H₂SO₄ anolyte, and an anode composed of a IrO_x layer deposited on porous carbon paper GDL. Activation of the cathode was performed before electrolysis as described in Section 2.2.1. The distances separating the various elements were: 0 mm from cathode to gas-flow plate (d_{cg}), 4 mm from cathode to membrane (d_{cm}), 4 mm from anode to membrane (d_{am}), and 0 mm from anode to back plate (d_{ab}). In this

configuration, denoted as C | 1 | CEM | 1 | A (C = cathode, 1 = gap filled with electrolyte, A = anode; the symbol | represents a solid-liquid interface), the distance separating the electrodes was 8.5 mm, considering that the membrane was 0.5 mm thick (this includes the two o-rings that keep the membrane in place). A three electrode setup was used to measure the potentials, with the cathode as the working electrode, the anode as the counter electrode and the Ag/AgCl reference electrode inserted in the catholyte compartment. The measured $|E_{\text{cell}}|$ for the C | 1 | CEM | 1 | A configuration was 3.61 V at an applied j of -200 mA cm^{-2} , while the product selectivity showed that CO production was favored over C_2H_4 , alongside minor H_2 formation (Figure 3.2). Only gas products were quantified at this stage. From here, the cell voltage can be decreased by starting to reduce the voltage drop at membrane.

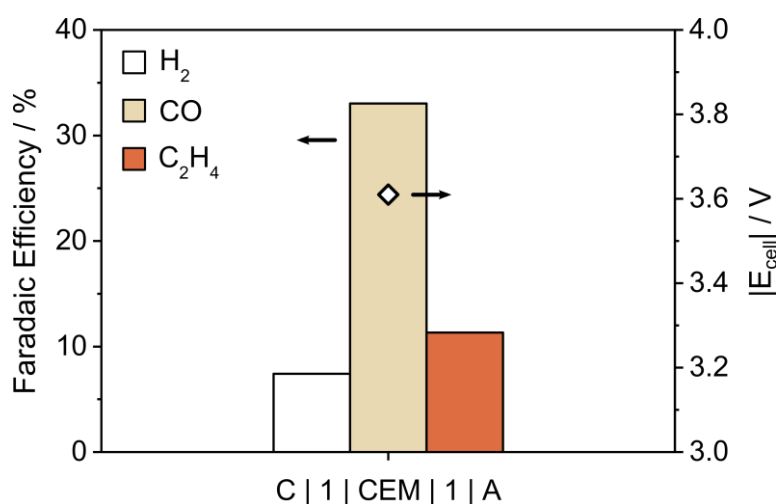


Figure 3.2 Performance of the electrolyte in the C | 1 | CEM | 1 | A configuration in terms of product selectivity and cell voltage. The electrolysis was carried out at -200 mA cm^{-2} for 30 min with an inlet flow of CO_2 of 10 mL min^{-1} .

3.2.2 Membrane contribution

Choosing to implement a Nafion membrane dictates what kind of electrolyte can be used on both sides of the cell. While the catholyte is rather flexible and can be tuned to obtain the desired performance, the choice of the anolyte is more restricted, because the only way to maintain a stable system over time is to keep the anolyte salt-free. If metal cations are present,

they will migrate towards the cathode in competition with protons, and if their concentration is high enough they will be the major charge carrier through the membrane, leading to an accumulation in the catholyte.¹⁶⁸ This would also result in protons depletion in the catholyte, where the H^+ consumed in the reaction with the OH^- generated at the cathode are not replenished with the protons produced at the anode. Experimental evidence of this phenomenon is provided in Figure 3.3, where an anolyte containing 0.5 M of K_2SO_4 and 0.05 M of H_2SO_4 was compared to one containing only the acid (0.05 M of H_2SO_4). When the ratio $[\text{K}^+] / [\text{H}^+]$ was unbalanced towards potassium ($1 \text{ M} / 8 \times 10^{-2} \text{ M}$ in this case), the latter carried most of the charge through the Nafion membrane and, over a short time, this led to a dramatic increase in the catholyte pH (Figure 3.3a). Instead, when the only positively charged species in the anolyte was H^+ ($5.6 \times 10^{-2} \text{ M}$), the protons depleted at the cathode were constantly replenished by those coming from the anolyte, where the H^+ concentration was kept constant by the protons coming from the OER (Figure 3.3b). In this way, both electrolytes can be stable during long term electrolysis. However, the incompatibility of metal cation-rich anolytes with Nafion constitutes a disadvantage for the system, as the anolyte composition cannot be optimized to lower the $|E_{\text{cell}}|$. In addition, as already mentioned, CEMs introduce a voltage drop

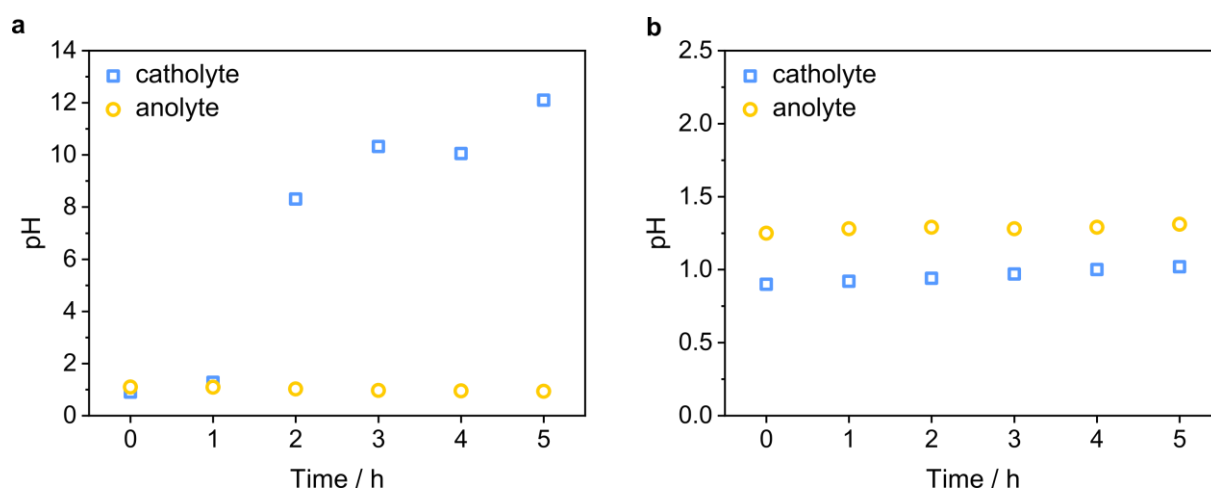


Figure 3.3 Effect of alkali metal cations in the anolyte. (a) Anolyte composition: 0.05 M H_2SO_4 / 0.5 M K_2SO_4 ; (b) Anolyte composition: 0.05 M H_2SO_4 . The catholyte composition is the same for both cases: 3 M KCl + 0.05 M H_2SO_4 .

that negatively affects the E_{cell} ,¹⁷⁶ with the intensity of the resistance that opposes the passage of charged species depending on the nature of the cation.

To reduce the E_m and enable a wider variety of anolyte-compatible ions, Nafion can be replaced by a diaphragm as compartment separator. Zirfon is an example of separator widely used for alkaline water electrolysis applications.^{177–179} It is a hydrophilic composite diaphragm consisting of a combination of a polysulfone matrix and a zirconium oxide inorganic filler.¹⁸⁰ With no charged groups, Zirfon is a non-ion selective separator and its conductivity is only determined by the electrolyte used.¹⁸¹ Therefore, any solution-phase species, charged or neutral, is able to cross from one side of the cell to the other, while gases crossover is prevented. For this reason, the electrolyte solution should be the same for both anode and cathode compartments. Implementing Zirfon in a system with the C | 1 | CEM | 1 | A configuration required a re-evaluation of the electrolyte species, especially because the KCl used in the catholyte solution could not be implemented at the anode, since Cl^- anions would oxidize and generate toxic Cl_2 gas.

3.2.3 Electrolyte considerations

Choosing alternative ions to employ as solutes is not straightforward due to the wide range of possible cation-anion combinations, but molar ionic conductivity tables can be used to find suitable candidates that will provide low resistance solutions (Table 3.1).^{182,183} The previously described C | 1 | CEM | 1 | A system employed 3 M KCl as the major cathodic solute. Although very soluble (340 g L^{-1} , $20 \text{ }^\circ\text{C}$), K^+ and Cl^- do not provide very high ionic conductivity values ($73.5 \text{ S cm}^2 \text{ mol}^{-1}$ and $76.3 \text{ S cm}^2 \text{ mol}^{-1}$, respectively), and, since at a concentration of 3 M the solution is close to the saturation point, the salt content cannot be increased to improve the conductivity. A different salt able to provide a higher ionic strength would therefore increase the solution conductivity and help improve the E_{cell} . In the following tests, various electrolyte solutions were evaluated in terms of the resulting product selectivity. A Nafion membrane was used as a separator to prevent the crossover of species that might alter the selectivity at the

Table 3.1 Molar ionic conductivity values for common cations and anions. ^a Data from ref. 182; ^b data from ref. 183.

Ion	Ionic conductivity / S cm ² mol ⁻¹
H ⁺	350.1 ^a
Na ⁺	50.1 ^a
K ⁺	73.5 ^a
Cs ⁺	77.3 ^b
Cl ⁻	76.3 ^a
SO ₄ ²⁻	160.0 ^a
PO ₄ ³⁻	207.0 ^a
CO ₃ ²⁻	138.9 ^a
CH ₃ COO ⁻	40.9 ^b
OH ⁻	198 ^a

cathode; hence the E_{red} was used as an indicator of the solution resistance. Both catholyte and anolyte compartments employed the same electrolyte solutions to maximize conductivity. The choice for the cation is rather limited and, excluding H⁺, mono-charged ions do not provide high ionic conductivities. Despite this, potassium has proven efficient in suppressing HER and boosting CO₂R in acidic electrolytes, therefore K⁺ represents a good cation candidate for the system. Concerning the anion, chloride salts should be avoided to prevent hazardous Cl₂ evolution at the anode, but multiple other inert anions can be employed.

First, the use of acetate buffers was considered, as they can attain very high concentrations owing to the excellent miscibility of acetic acid with water and the extremely high solubility of potassium acetate (2686 g L⁻¹, 25 °C), which could potentially compensate for the sub-optimal conductivity of CH₃COO⁻ (40.9 S cm² mol⁻¹). Potassium acetate buffers with different concentrations (each with a pH around 5) were prepared and tested (Figure 3.4a). The FE distribution at 1 M shows little CO (7.7%) and a significant amount of C₂H₄ (25%) with a

reasonably low FE for H₂ production (32.6%). However, the selectivity for CO₂R was quickly lost when the buffer concentration was increased to 2 M and then 3 M. Additionally, the E_{red} did not reach values less negative than -2 V, suggesting that the low conductivity of the solution even at 3 M was a limiting factor.

Then, a phosphate buffer was tested (Figure 3.4b). The main salt used for the buffer, KH₂PO₄, is not very soluble (226 g L⁻¹, 20 °C) and despite PO₄³⁻ being very conductive due to its high charge (207.0 S cm² mol⁻¹), the E_{red} remained highly negative (-2.7 V vs. Ag/AgCl) at a buffer concentration of 1 M (pH 5). HER was predominant in this case (FE 51%), while C₂H₄ (FE 21%) was favored over CO (FE 3%).

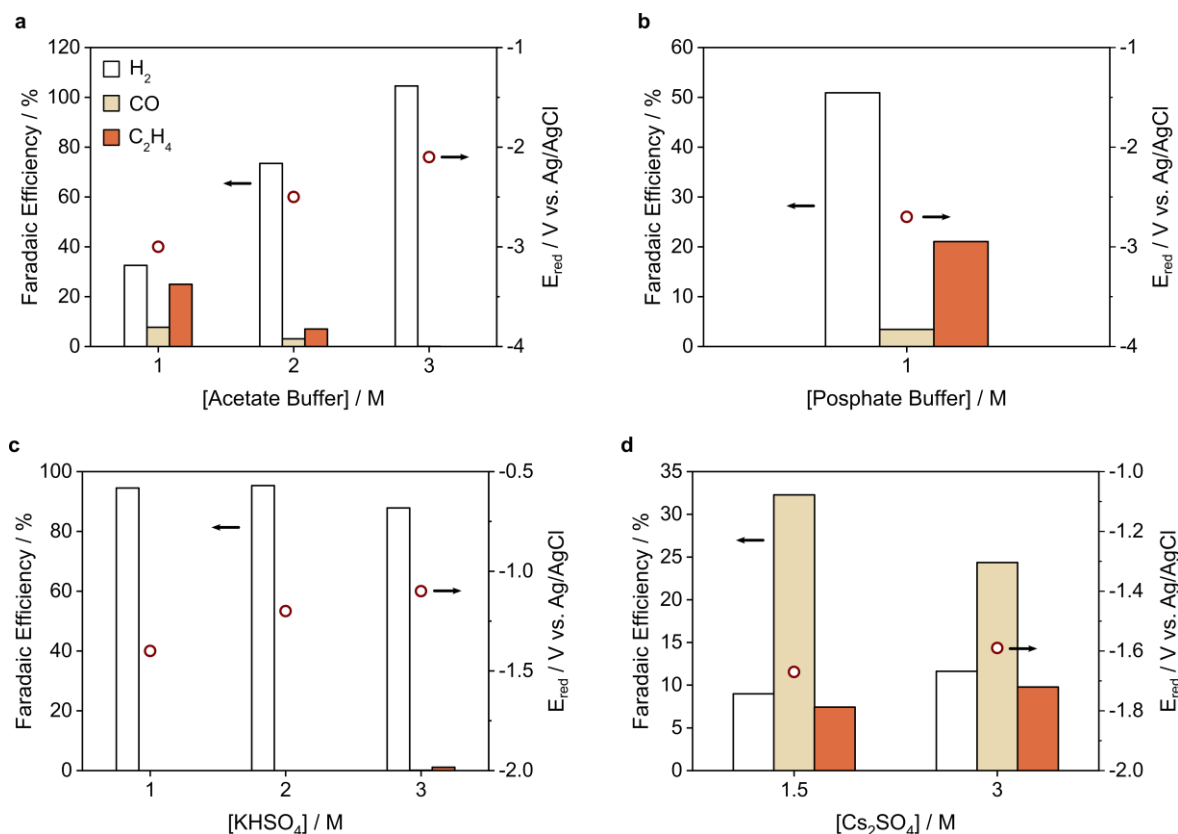


Figure 3.4 Results of the electrolyte screening tests. (a) Acetate buffer (CH₃COOH + CH₃COOK); (b) phosphate buffer (KH₂PO₄ + K₂HPO₄); (c) KHSO₄; (d) Cs₂SO₄. The electrolysis were carried out at -200 mA cm⁻² for 30 min with an inlet flow of CO₂ of 10 mL min⁻¹ in a C | 1 | CEM | 1 | A configuration.

As a final search for an appropriate potassium salt, the use of an acid salt that has a solubility similar to $\text{KCl} - \text{KHSO}_4$ – was explored (490 g L^{-1} , $20 \text{ }^\circ\text{C}$). In this case, the SO_4^{2-} anion provides high conductivity ($160.0 \text{ S cm}^2 \text{ mol}^{-1}$). Testing at different concentrations (all with a $\text{pH} < 1$) revealed that the cathodic potential could be significantly lowered (up to -1.1 V vs. Ag/AgCl with $[\text{KHSO}_4] = 3 \text{ M}$), however the only product detected at any of the concentrations tested was H_2 , which might be the reason of the less negative E_{red} , since HER requires a lower voltage to occur (Figure 3.4c). Nevertheless, sulfate salts seemed the most suitable electrolytes in terms conductivity and potential, thus they were explored further. K_2SO_4 was tested but gave poor results (E_{red} of -2.2 V vs Ag/AgCl , $[\text{K}_2\text{SO}_4] = 0.5 \text{ M}$, $\text{pH} 6$) likely because of its low solubility (111 g L^{-1} , $20 \text{ }^\circ\text{C}$). An extremely soluble sulfate-based salt can be obtained by replacing potassium with cesium: Cs_2SO_4 (Figure 3.4d). Cesium sulfate possesses a remarkably high solubility (1790 g L^{-1} , $20 \text{ }^\circ\text{C}$) and provides ions with a global good ionic conductivity ($77.3 \text{ S cm}^2 \text{ mol}^{-1}$ for Cs^+ and $160.0 \text{ S cm}^2 \text{ mol}^{-1}$ for SO_4^{2-}). It is also worth noting that every mole of Cs_2SO_4 yields two moles of Cs^+ , meaning that a high ionic strength can be attained with concentrated solutions. At a concentration of 1.5 M ($\text{pH} 5$, adjusted with H_2SO_4) CO production was favored over that of ethylene (FEs 32% and 7% , respectively), a selectivity that could be similarly maintained when the concentration was increased to 3 M ($\text{pH} 5$). The E_{red} was -1.7 V and -1.6 V vs. Ag/AgCl at 1.5 M and 3 M , respectively, indicating that a Cs_2SO_4 solution was the only electrolyte able to favor CO_2R selectivity over HER while affording a relatively high solution conductivity. Moreover, as mentioned in Section 2.1, alkali cations are essential to suppress HER in acid solutions, with larger ions being more effective due to their stronger propensity to adsorb on the negatively charged cathode ($\text{Li}^+ < \text{Na}^+ < \text{K}^+ < \text{Cs}^+$). Therefore, replacing potassium with cesium could lead to an improved system performance. From here, the CuO cathode activation is performed in a $1.5 \text{ M Cs}_2\text{SO}_4$ electrolyte ($\text{pH} 7.2$).

3.2.4 Zirfon optimization

Having established that Cs_2SO_4 was a good candidate for improving selectivity and ionic conductivity, the focus shifted to understanding how this electrolyte solution, employed on both sides of the cell, would behave in a Zirfon-based system.

The previous C | 1 | CEM | 1 | A configuration was employed to test the Zirfon diaphragm in combination with cesium sulfate (C | 1 | DIA | 1 | A configuration, where DIA = Zirfon diaphragm). Initially, Cs_2SO_4 concentration was set to 1.5 M (pH 5 adjusted by H_2SO_4 addition) to match the amount of alkali cations found in the catholyte of C | 1 | CEM | 1 | A, which contained 3 M KCl. This first test resulted in an $|E_{\text{cell}}|$ of 3.90 V. However, upon increasing the salt concentration to 3 M (pH 5), the cell voltage was reduced to 3.67 V. This decrease in $|E_{\text{cell}}|$ can be ascribed to the reduced solution resistance as a consequence of improved ionic conductivity. The C | 1 | DIA | 1 | A system can be described as a two-gap reactor, as there are two gaps filled with electrolyte separating the electrodes, with the separator in between. The cell voltage can be optimized further by switching to a one-gap setup, thereby decreasing the resistance introduced by the electrolyte as less solution is present between the electrodes. To do this, the anode was placed in direct contact with the Zirfon (MEA setup), resulting in a zero-gap anodic compartment, while the cathodic side retained the one-gap. As the anode is composed of IrO_x deposited on porous carbon paper, the anolyte can flow between the electrode and the backplate, thereby maintaining the contact between the electrolyte solution and the anode catalyst. This one-gap configuration is denoted as C | 1 | DIA | A ($d_{\text{cg}} = 0$ mm, $d_{\text{cm}} = 4$ mm, $d_{\text{am}} = 0$ mm, $d_{\text{ab}} = 4$ mm), with the electrodes separated by a distance of 4.5 mm. When C | 1 | DIA | A was implemented with a 3M Cs_2SO_4 electrolyte solution, the reduced distance between the electrodes improved the $|E_{\text{cell}}|$, which dropped to 3.20 V (potential optimization results are shown in Figure 3.5a). Furthermore, a similar product distribution could be maintained upon varying the electrolyte concentration and electrode separation distance (Figure 3.5b). Overall, the increased ionic strength given by concentrated cesium sulfate

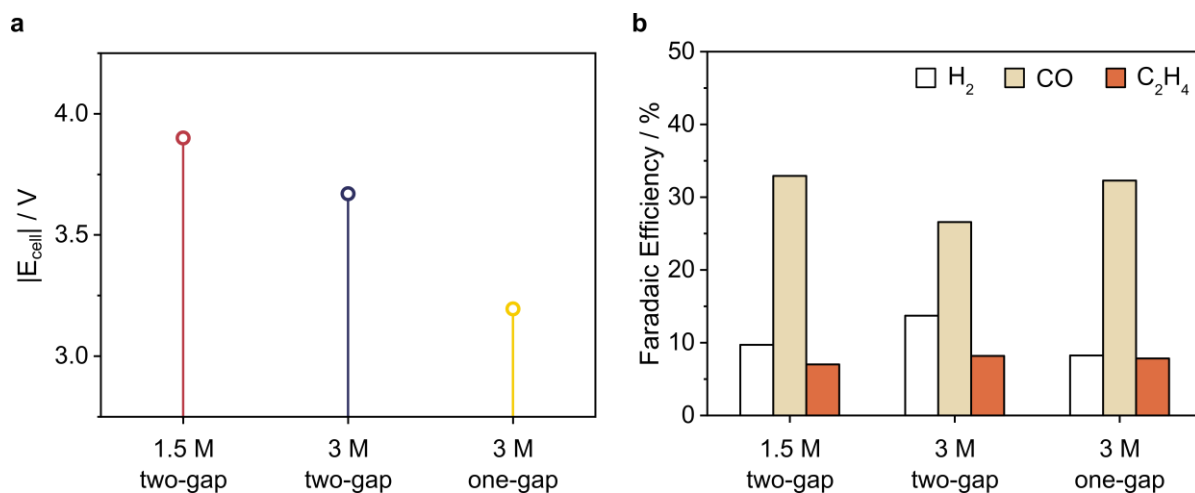


Figure 3.5 Summary of the $|E_{\text{cell}}|$ optimization of the electrolyzer in a C | 1 | DIA | 1 | A (two-gap) and a C | 1 | DIA | A (one-gap) configuration. The x axis indicates the molarity of the Cs_2SO_4 (both solution have a pH around 5) and the cell configuration. The electrolysis were carried out for 30 min each at -200 mA cm^{-2} with an inlet flow of CO_2 of 20 mL min^{-1} .

coupled with Zirfon in a C | 1 | DIA | A configuration afforded a cell potential that is 0.41 V lower than the one obtained for the C | 1 | CEM | 1 | A setup (Figure 3.2).

These results show how Zirfon and Cs_2SO_4 are a suitable combination to effectively lower the $|E_{\text{cell}}|$. However, even in this case the composition of catholyte and anolyte is not stable over time due to the lack of species selectivity at the separator. In particular, the pH of the catholyte will increase as Cs^+ electromigration towards the cathode will result in accumulation in the catholyte solution while protons will be depleted through neutralization reaction with OH^- . Simultaneously, the anolyte will become more acidic due to an increased H^+ concentration resulting from anodically-generated protons. As a result, after just 30 min of electrolysis (3 M Cs_2SO_4 , C | 1 | DIA | A setup), the catholyte pH increased from pH 5 to 11, while the anolyte pH decreased to pH 2. A way to solve this issue while also keeping the lower cell voltage afforded by the setup is to continuously mix catholyte and anolyte, allowing for equilibration of any species that might cross the Zirfon during the reaction. However, the implementation of a mixing setup requires careful consideration of all the system elements.

3.2.5 Electrolyte mixing

Mixing catholyte and anolyte together outside of the reactor could benefit the overall device stability as buildup of ionic species and altered pH in each compartment can be counteracted. Mixed electrolyte solutions have been used to equilibrate the electrolyte composition during CO_2 electrolysis to CO with silver GDEs,^{120,184,185} while there are no reported examples investigating the effects of the mixing in complex systems where several gaseous and liquid CO_2R products are formed. The mixing setup was implemented for the one-gap C | 1 | DIA | A configuration (Figure 3.6). The electrolyte was injected into both cell compartments from a main reservoir using peristaltic pumps. The solution coming out from the catholyte outlet (rich in CO_2R products, CO_2 and H_2) was directly recollected in the main reservoir, while the liquid output of the anodic half-cell passed first through a container termed degassing reservoir and was then transferred to the main reservoir with a second pump. This is needed in order to remove the oxygen from the electrolyte before it reaches the cathodic chamber, otherwise it can be reduced to water at the cathode, thereby competing with CO_2 for the available electrons.

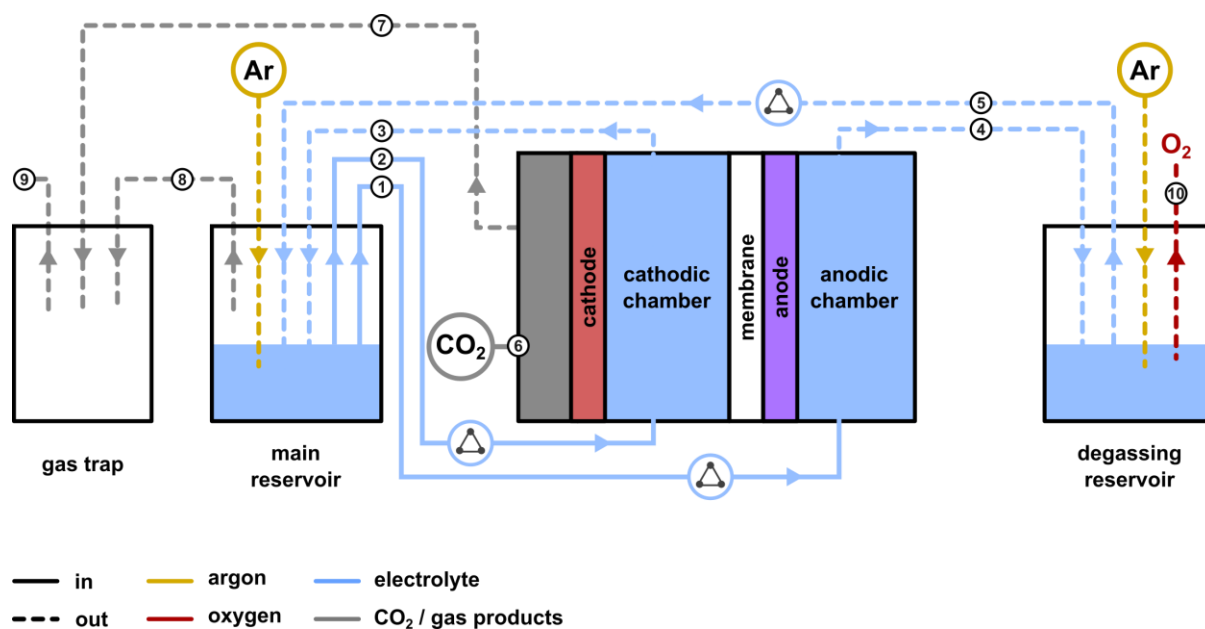


Figure 3.6 Illustration of the mixing setup with the C | 1 | DIA | A configuration. (1) catholyte inlet, (2) anolyte inlet, (3) catholyte outlet containing the indirect gas outlet, (4) anolyte outlet, (5) degassing reservoir liquid outlet, (6) CO_2 inlet, (7) direct outlet, (8) main reservoir outlet, (9) path to GC, (10) degassing reservoir gas outlet.

Hence, the degassing reservoir was installed between the anolyte outlet and the main reservoir, where purging the electrolyte solution with Ar efficiently removed O_2 . With this system in place, no oxygen could be detected in the headspace of the main reservoir, confirming that O_2 was prevented from reaching the cathode. As a consequence of the mixing setup, there is no more distinction in the composition of catholyte and anolyte. Gas reduction products and unused CO_2 are gathered in the gas trap through the direct outlet of the cell and the gas outlet of the main reservoir, where they degas from the solution brought by the catholyte outlet (for a detailed description concerning the gas transport through the different outlets refer to Chapter 2).

Constant electrolyte mixing allows to equilibrate any species that is preferentially produced at one of the electrodes and those that migrate from one side of the cell to the other. When employing a mixed 3 M Cs_2SO_4 solution in a C | 1 | DIA | A configuration, the cell performance did not vary compared with the same non-mixing setup (Figure 3.7). CO formation was still favored over that of C_2H_4 (FEs 38% and 8%, respectively) and the $|E_{cell}|$ remained practically unchanged (3.2 V). Regarding the pH of the two sides, it can be kept constant at a pH value of 4.5 over the course of a 3 h electrolysis. Therefore, a Cs_2SO_4 -based mixing electrolyte coupled with a Zirfon diaphragm enhances electrolyte stability in terms of composition and pH

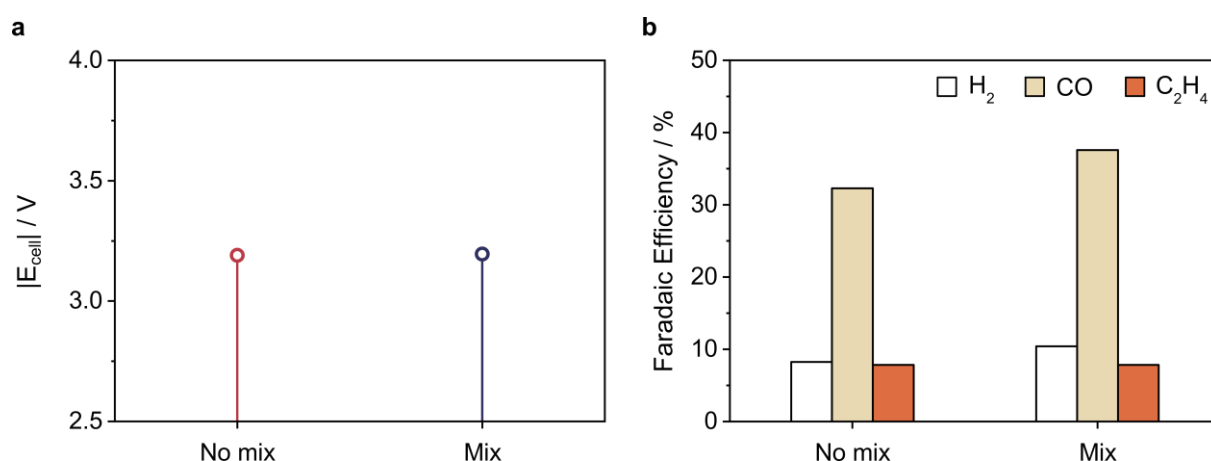


Figure 3.7 Comparison between a non-mixing and a mixing system in a C | 1 | DIA | A configuration. The electrolysis were carried out for 30 min each at -200 mA cm^{-2} with an inlet flow of CO_2 of 20 mL min^{-1} and a 3 M Cs_2SO_4 (pH 5) electrolyte.

without affecting the electrolyzer performance ($|E_{\text{cell}}|$ and gas product selectivity unchanged). However, since CO_2R products can cross compartments (either by passing through the diaphragm or by being re-injected into the opposite half-cell from the main reservoir), they are susceptible of being involved in further unwanted electrochemical reactions, such as liquid carbon products oxidation at the anode, which is an important point that must be addressed.

Liquid products

The complete selectivity of the mixing C | 1 | DIA | A configuration is shown in Figure 3.8. While CO_2R gas products (carbon monoxide and ethylene) are not affected by the mixing setup (Figure 3.7), liquid products can potentially be oxidized at the anode, which would reflect on the total FE. To evaluate this possibility, three separate oxidation tests were performed to assess the susceptibility to oxidation of formic acid, ethanol and propanol. Water electrolysis was carried out in the cell (HER at the cathode and OER at the anode, with the latter as the WE) before adding one of the products to the electrolyte and no CO_2 was injected into the reactor. In the first test, 28.7 μmol of ethanol were added to a 3 M Cs_2SO_4 solution (pH 5) after 5 minutes of water electrolysis, which caused the anodic potential to increase by 0.12 V (from 1.52 V to 1.64 V vs. Ag/AgCl). During the experiment, ethanol was gradually transformed into acetic acid, and after 160 min it was almost completely consumed (Figure 3.9a). At the end of

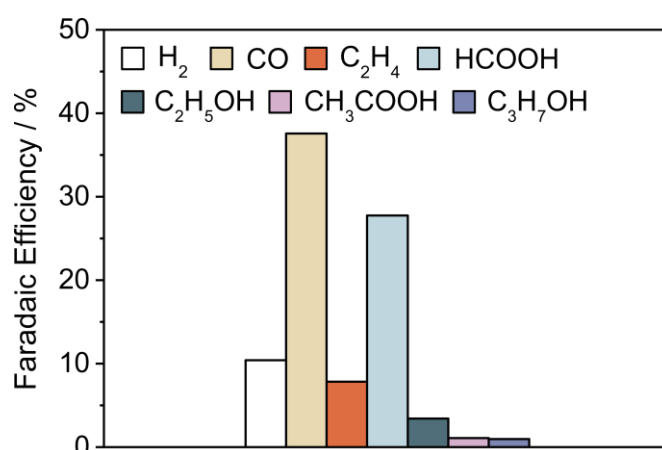


Figure 3.8 Complete product selectivity of the mixing C | 1 | DIA | A configuration. The electrolysis was carried out for 30 min at -200 mA cm^{-2} with an inlet flow of CO_2 of 20 mL min^{-1} and a 3 M Cs_2SO_4 (pH 5) electrolyte.

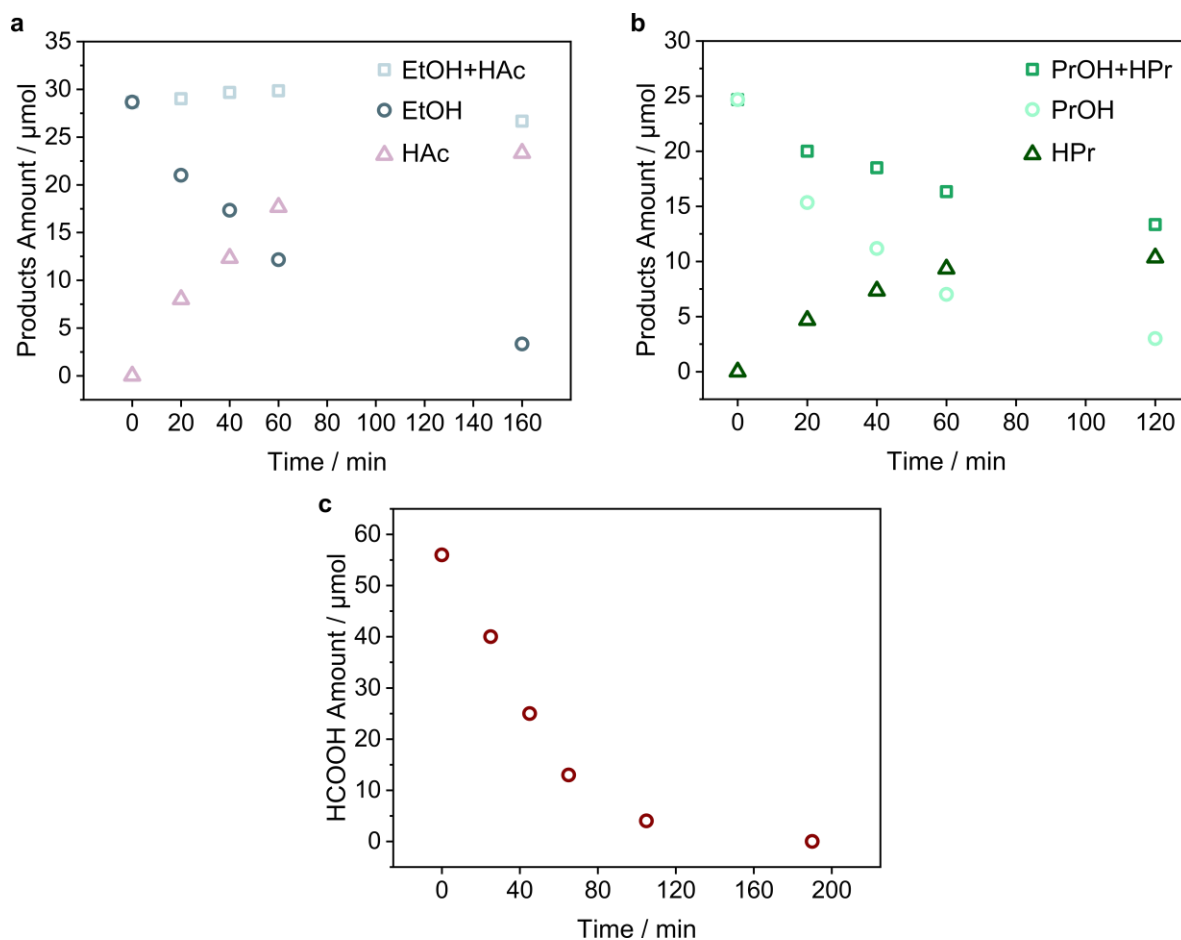


Figure 3.9 Results of the three oxidation tests: (a) ethanol; (b) propanol; (c) formic acid. The electrolysis were carried out in a mixing C | 1 | DIA | A configuration at -200 mA cm^{-2} without flowing CO_2 and a 3 M Cs_2SO_4 (pH 5) electrolyte.

the electrolysis the total amount of carbon species (residual ethanol + accumulated acetic acid) accounted for 93% of the ethanol added at the beginning ($26.7 \mu\text{mol}$). This might be the consequence of a slight ethanol evaporation or of slow acetic acid oxidation to CO_2 . To test the second hypothesis, CO_2 evolution was monitored and, during the course of the electrolysis, a total of $4 \mu\text{mol}$ of CO_2 was recorded (average molar flow of 0.41 nmol s^{-1} over 160 min), which accounts for the missing 7% considering that a molecule of ethanol would be ultimately oxidized to two molecules of CO_2 . However, since the quantities considered are very small, ethanol evaporation cannot be excluded without further testing. Propanol oxidation to propionic acid behaved similarly (Figure 3.9b) and its addition to the electrolyte resulted in a potential increase of 0.08 V (from 1.55 to 1.63 V vs. Ag/AgCl). In this case the carboxylic acid accumulated in solution more slowly and the total amount of the two species decreased

progressively over time. After 120 min, only 54% (13.3 μmol , residual propanol + accumulated propionic acid) of the initial 24.7 μmol of propanol were left. A higher flow of CO_2 (5.22 nmol s^{-1}) was recorded, accounting for a total of 37.6 μmol at the end of the electrolysis, a value that corresponds well with the missing 46%, considering that propanol complete oxidation gives 3 molecules of CO_2 per molecule of alcohol. Formic acid oxidation to CO_2 is more straightforward as there are no intermediate products (Figure 3.9c). Its addition increased the anodic voltage by 0.2 V (from 1.85 to 2.05 V vs. Ag/AgCl), and, after 190 min, it was completely oxidized to CO_2 . This evaluation evidenced that care must be taken when dealing with a mixing setup involving CO_2R liquid products, and that their oxidation can lead to a decreased total FE. It is acknowledged that the carbon paper constituting the anode might also oxidize to CO_2 and interfere with the measurement; however, no significant CO_2 evolution was recorded during a blank experiment (water electrolysis with no supplied CO_2).

Carbon mass balance

While the FE evaluation ensures that most of the available electrons are used for CO_2R , analyzing the carbon mass balance allows to keep track of all of the feed CO_2 to guarantee that it is either reduced to products or it leaves the cell unused. Ideally, all of the CO_2 that is fed to the cell should be converted to the desired CO_2R products, thereby achieving total conversion. This does not usually happen, and a certain amount of unused CO_2 is vented from the reactor outlets, as described in Chapter 2. Measuring the amount of CO_2 contained in each of these outlets is important to adopt the best strategy to recover the reactant and close the carbon mass balance. In the mixing configuration there are three possible gas exit points: the direct outlet, the indirect outlet and the degassing outlet (Figure 3.6). When the system was left to equilibrate with a CO_2 feed flow rate of 1.15 mL min^{-1} (given the low flow rate, time is required for the CO_2 to saturate the entire system) and no applied current, the feed CO_2 available for reduction was 681 nmol s^{-1} . During electrolysis at -200 mA cm^{-2} (Figure 3.10), part of the feed CO_2 was found in the combined flows of the direct and indirect outlets and in the flow of the degassing outlet (43% and 28% of the feed CO_2 , respectively). This fraction

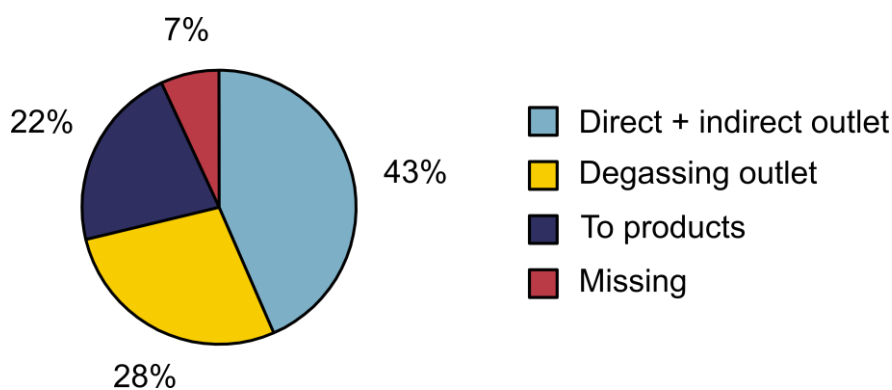


Figure 3.10 Carbon mass balance assessment. The amounts of CO_2 are expressed in molar flow values (nmol s^{-1} , averages of at least 1 h). The whole pie represents the total CO_2 available with a feed CO_2 flow rate of 1.15 mL min^{-1} (681 nmol s^{-1}). Direct + indirect outlets 296 nmol s^{-1} ; degassing outlet: 189 nmol s^{-1} ; to CO_2R products: 149 nmol s^{-1} ; missing: 47 nmol s^{-1} . The electrolysis was carried out in a mixing C | 1 | DIA | A configuration at -200 mA cm^{-2} with an inlet flow of CO_2 of 1.15 mL min^{-1} and a $3 \text{ M Cs}_2\text{SO}_4$ (pH 5) electrolyte.

represents the CO_2 that bypassed the cell without reacting and the r-CO_2 recovered from carbonate, defined together as unused CO_2 . By comparison, the remaining 29% should be reduced to CO_2R products; however, only 22% of the initial CO_2 was found converted into carbon products. The overall discrepancy of 7% between the input of CO_2 and the output (reduced + unused fractions) can be considered within error since the measurement are taken hours apart from each other to allow equilibration of the system before each measurement (condition required by the low feed CO_2 flow rate). From these data, it can be concluded that the reactor in a mixing configuration was able to maintain a closed carbon mass balance.

3.2.6 Temperature

With the mixing configuration in place, the Zirfon diaphragm can be implemented without the issues associated with electrolyte imbalances. A way to decrease the cell voltage beyond the value afforded with the mixing C | 1 | DIA | A configuration (3.2 V) is to increase the temperature of the system (Figure 3.11).

Heat is inevitably produced when current is passed through a cell with nonzero internal resistance (Joule heating).¹⁸⁶ In industrial electrolyzers, heat production results in high

operating temperatures due to the scale of the reactors. For example, common alkaline water electrolyzers run at temperatures that range between 80-150 °C.¹⁸⁷ These resistive losses lead to a reduced overall cell energy efficiency (defined as the ratio of thermodynamic potential required for products formation over the measured cell voltage)¹⁸⁸ because electric energy is converted to waste heat instead of being used for the reaction. Nevertheless, the resulting higher operating temperature can compensate the efficiency loss, since increasing the temperature leads to a reduced cell voltage by decreasing the potentials associated with kinetic and thermodynamic contributions of CO₂ reduction.¹⁸⁷ Therefore, in bench-scale tests, cells

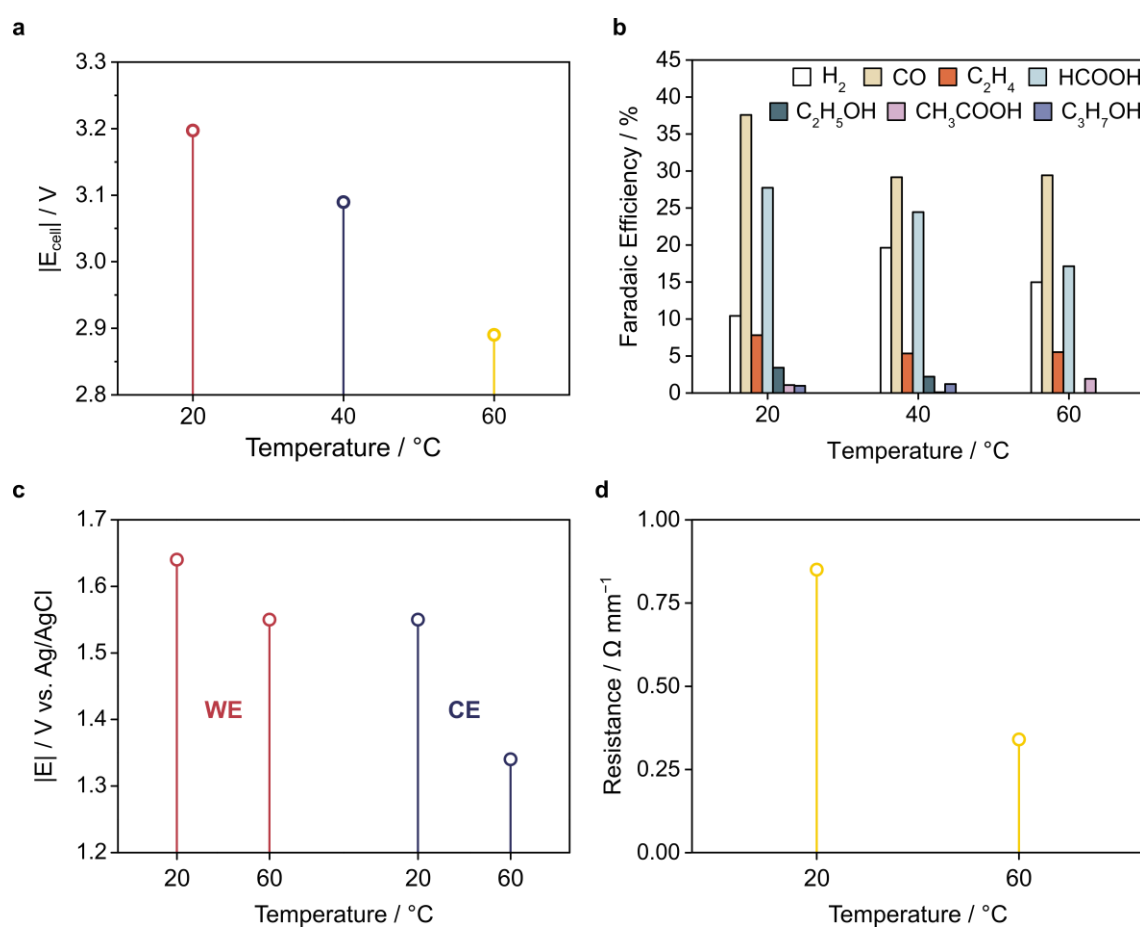


Figure 3.11 Effects of the electrolyte solution temperature. (a) Cell voltage decrease due to the increase in temperature and (b) relative product distribution for the three tests. (c) Working and counter electrode potentials and (d) solution resistance comparison at 20 °C and 60 °C, values measured between the WE (cathode) and the RE. The electrolysis were carried out for 30 min each at -200 mA cm^{-2} with a feed flow of CO₂ of 20 mL min^{-1} in a 3 M Cs₂SO₄ solution (pH 5) and a mixing C | 1 | DIA | A configuration.

can be heated to better resemble industrial working conditions and to take advantage of reduced cell voltages, keeping in mind that large-scale reactors do not need an external heat source due to their size. There are a few reported examples that investigate the temperature effects on the performance of CO₂R systems.^{96,187,189–194} However, most of these reports focus mainly on formic acid and carbon monoxide, while neglecting systems forming multicarbon products.

When the temperature of the electrolyte was increased from 20 °C (room temperature) to 40 °C, the $|E_{\text{cell}}|$ could be lowered from 3.2 V to 3.08 V. By reaching 60 °C, a remarkable cell voltage of 2.89 V could be attained, going past the threshold value of 3 V with a current density of -200 mA cm^{-2} , with an overall gain of 0.33 V with respect to the system at 20 °C (Figure 3.11a). The decrease in $|E_{\text{cell}}|$ did not come at the expense of the selectivity and a similar product distribution can be maintained from 20 °C to 60 °C (Figure 3.11b). The total FE was a little lower than expected at higher temperatures (89%, 82% and 69% for 20 °C, 40 °C and 60 °C, respectively) due to partial oxidation of formic acid, ethanol and propanol to CO₂ at the anode. Therefore, the FEs for liquid products reflect their continuous production and oxidation. Additional tests with cold traps to intercept alcohol evaporation will be needed to build a complete picture of the liquid product distribution. It is worth noting that propionic acid could be detected after 30 min, but it was only visible when the electrolysis was carried out for more than an hour.

With the increased temperature, the electrodes voltage and the electrolyte conductivity both contributed to the decrease in $|E_{\text{cell}}|$. The working electrode (cathode) voltage diminished by 0.09 V vs. Ag/AgCl when the temperature was brought from 20 °C to 60 °C, while at the same time the counter electrode (anode) potential was reduced by 0.21 V vs. Ag/AgCl (Figure 3.11c). In addition, the solution resistance values were $0.85 \text{ } \Omega \text{ mm}^{-1}$ and $0.34 \text{ } \Omega \text{ mm}^{-1}$ at 20 °C and 60 °C, respectively (Figure 3.11d), which indicated a higher conductivity of the solution at 60 °C. The CE potential experienced a larger variation than the WE potential because it also includes the contribution of the E_{m} , other than the E_{ox} and the E_{cath} . Moreover, gas bubbles

should become smaller at higher temperature, leading to an improved electrode-electrolyte contact that might also contribute to the lower $|E_{\text{cell}}|$.¹⁸⁷

Lowering the feed flow rate of CO_2 increases the selectivity for multicarbon products, as already explained in Chapter 2. This can also be applied to the C | 1 | DIA | A configuration at increased temperature and the preliminary results at 40 °C are shown in the Appendix (Figure A.3).

3.2.7 Voltage optimization summary

Figure 3.12 summarizes the voltage optimization for the Zirfon-based system described in the previous sections. The cell potential could be lowered from 3.90 V (Figure 3.12a) to 2.89 V, a remarkable gain of more than 1 V (Figure 3.12b). The main contributions for the optimization were: (1) increased cesium sulfate concentrations (from 1.5 M to 3 M, both pH 5), which

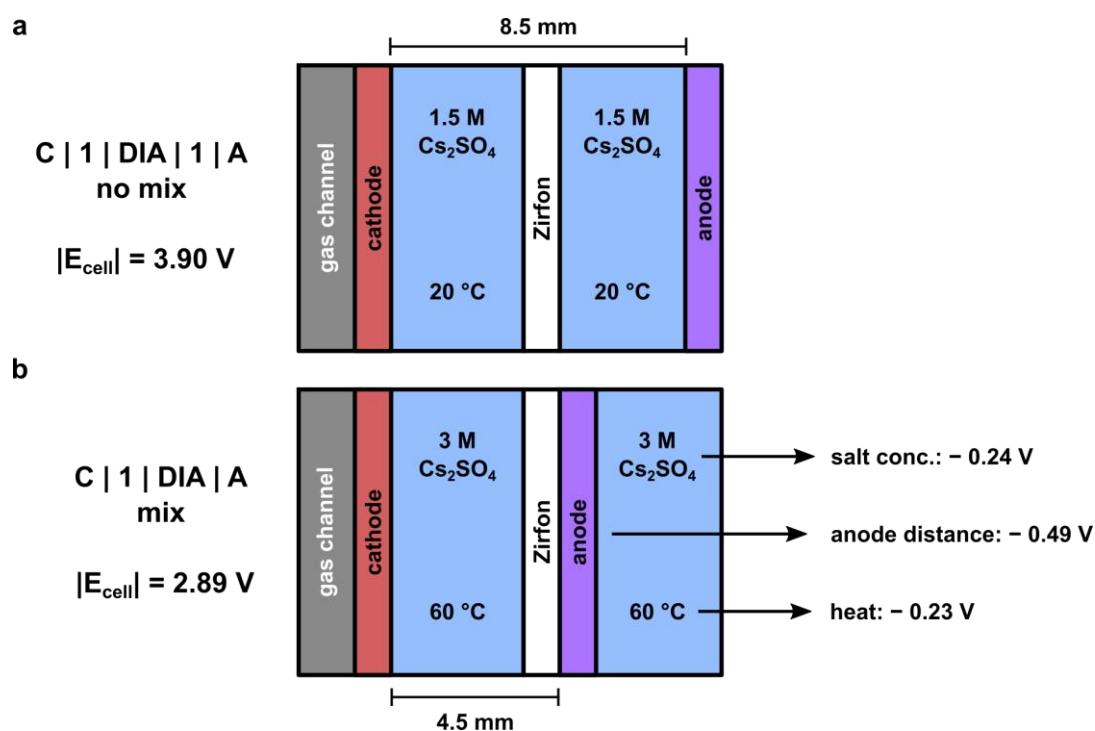


Figure 3.12 Optimization of the Zirfon-based system, from the C | 1 | DIA | 1 | A ($|E_{\text{cell}}| = 3.90 \text{ V}$) to the C | 1 | DIA | A ($|E_{\text{cell}}| = 2.89 \text{ V}$) configuration at -200 mA cm^{-2} . The three contributions shown here, accounting for an improvement of 0.96 V, were measured during three separate tests. This is way there is a slight discrepancy with the voltage gained when all three modifications were applied at the same time (1.1 V).

reduced the $|E_{\text{cell}}|$ by 0.24 V; (2) decreased electrodes distance (from 8.5 mm to 4.5 mm), resulting in a gain of 0.49 V; (3) higher temperature (from 20 °C to 60 °C), which lowered the cell voltage by 0.23 V. The mixing did not affect the voltage directly, but it allowed to establish a system with a stable electrolyte over time in terms of pH and composition. It is important to note that when applying the same modifications to the C | 1 | CEM | 1 | A setup, thereby obtaining a C | 1 | CEM | A configuration, the voltage could not be lowered to the same extent (Figure 3.13). Decreasing the electrodes distance by adopting a one-gap configuration improves the $|E_{\text{cell}}|$ by 0.16 V, while increasing the temperature to 60 °C results in a gain of 0.21 V, resulting in an overall cell voltage of 3.24 V, 0.35 V more positive than the one obtained with the optimized C | 1 | DIA | A setup. The decrease obtained by rising the temperature was similar in the two cases, but the voltage gain due to the one-gap configuration, which was the main contribution for the optimization of the C | 1 | DIA | A system, was markedly different. The reason behind this might be that the resistance at 60 °C of a 1 M H_2SO_4 anolyte ($0.06 \Omega \text{ mm}^{-1}$) is lower than the one offered by a 3 M Cs_2SO_4 solution ($0.34 \Omega \text{ mm}^{-1}$), hence removing the

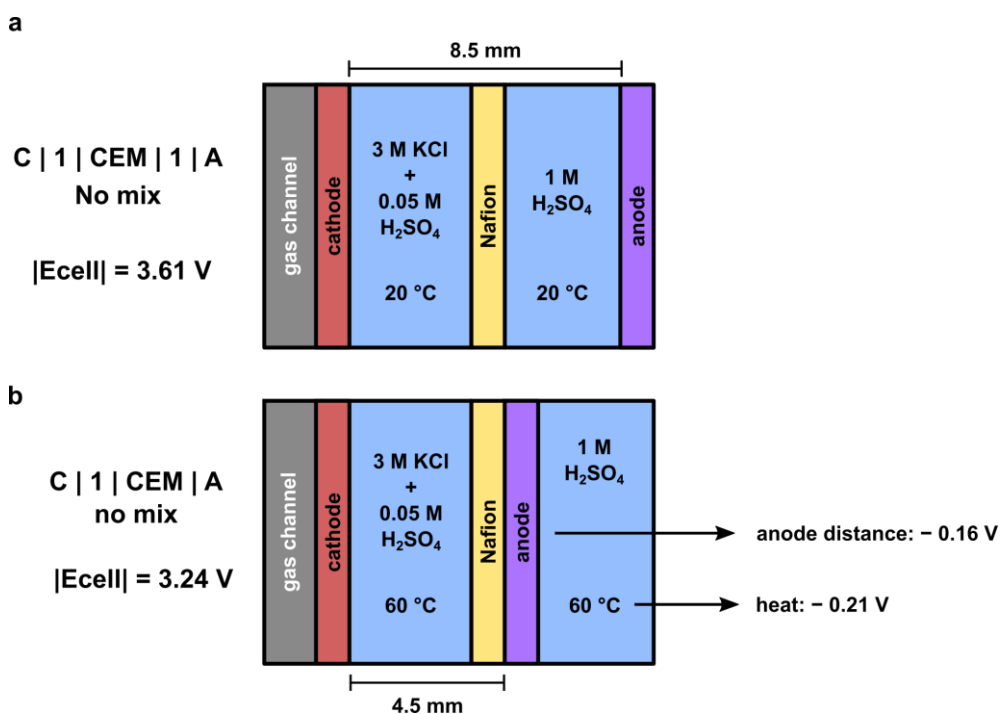


Figure 3.13 Optimization of the Nafion-based system, from the C | 1 | CEM | 1 | A ($|E_{\text{cell}}| = 3.61 \text{ V}$) to the C | 1 | CEM | A ($|E_{\text{cell}}| = 3.24 \text{ V}$) configuration -200 mA cm^{-2} .

voltage drop associated with the anolyte has a larger impact for the C | 1 | DIA | A setup. Once the one-gap setup was in place, the resistance between cathode and anode, which accounts for the voltage drops of catholyte and membrane, was lower for the DIA system ($0.81 \Omega \text{ mm}^{-1}$) compared to the CEM setup ($1.57 \Omega \text{ mm}^{-1}$). Therefore, since the resistance of the two catholytes was similar at $60 \text{ }^\circ\text{C}$ ($0.34 \Omega \text{ mm}^{-1}$ and $0.29 \Omega \text{ mm}^{-1}$ for $3 \text{ M Cs}_2\text{SO}_4$ and $3 \text{ M KCl} / 0.05 \text{ M H}_2\text{SO}_4$, respectively), it is clear that the resistance introduced by Nafion is the main impediment for the cell voltage optimization of the C | 1 | CEM | A configuration.

3.3 Discussion

In the previous sections, the $|E_{\text{cell}}|$ of a common Nafion-based gas-fed flow cell CO_2 electrolyzer was optimized by modifying parameters and components of the reactor. Because of the limits set by the Nafion membrane (resistance, electrolyte choice, stability), the cell voltage could only be lowered to a certain extent. The reason for keeping the anolyte salt-free is intrinsic to the transport mechanism through Nafion. Nafion membranes are rich in sulfonate groups ($-\text{SO}_3^-$) to selectively block anions and allow only positively charged species to cross, by hopping from a negative charge to the other under the influence of an electric potential.¹⁷⁴ Metal ions interact with the $-\text{SO}_3^-$ in a strong manner due to the ionic nature of the bond, which results in an increased resistance requiring a more intense driving force (i.e. voltage) to obtain efficient transport through the membrane.^{174,195} Several studies show a worse performance of Nafion membranes (permeability, ionic conductivity) when M^+ transport is favored over H^+ transport.^{196–198} Consequently, there is an important conductivity trade-off when using alkali electrolytes in combination with Nafion membranes: concentrated salts are usually employed to obtain high conductivity in solution, but at the same time, the conductivity of the membrane decreases due to the strong ionic interactions of M^+ with the sulfonic groups. Moreover, even when protons are the major charge carriers through the membrane, the resistance associated with Nafion prevents an effective voltage optimization, as shown in Figure 3.13. Conversely, a

Zirfon separator is better suited for the system, as it offers less resistance (no ionic interactions) to the transport of positive charges towards the cathode.

The electrolyte screening results shown in Section 3.2.3 evidenced the critical role of solubility and conductivity of salts and acids and how not many electrolytes are available beside the most common ones (KCl, K_2SO_4 , $KHCO_3$). Cs_2SO_4 was found to be most appropriate salt to couple with a Zirfon separator owing to its high ionic conductivity and ability to favor CO_2R over HER. In addition, cesium sulfate can be employed on both sides of the cell, thereby enabling a mixing configuration able to maintain the electrolyte composition and pH constant over time.

Gunter et al. have thoroughly investigated the mixing system.^{120,185,199} Their setup is focused on CO_2 conversion to CO and syngas ($CO + H_2$) while employing electrolytes such as K_2SO_4 , $KHCO_3$ and mixtures of the two, which result in near neutral pH solutions. They also employ high temperatures (up to 60 °C) but the $|E_{cell}|$ hardly goes below 4.5 V in the best case. One of the advantages of this system is that by producing only CO (and H_2), there is no liquid products oxidation at the anode, making the FE easier to manage. However, Gunter's group system suffers from CO_2 and O_2 evolution at the anode, which they partially avoid by using a membrane contactor or an anode GDE; nevertheless, since they use a high flow rate of feed CO_2 (100 mL min^{-1}), separation from CO is not straightforward while CO_2 remains distributed between the different reactor outlets.¹⁹⁹ In the system presented in Section 3.2.5, the acidity of the solution restricts CO_2 regeneration from carbonate to the cathode chamber and the main reservoir. To keep track of all of the CO_2 molecules that enter the reactor, whether they are reduced to products or leave the cell unreacted, it is useful to aim for a closed carbon mass balance. The unreacted fraction comprises the CO_2 that bypasses the cell (i.e. that never takes part in any reaction) and the CO_2 that is temporarily converted to (bi)carbonate and then regenerated owing to the acid electrolyte. The CO_2 feed flow rate selected for the mass balance experiment (1.15 mL min^{-1}) was rather low to ensure that most of the r- CO_2 was recovered at the indirect outlet as an almost pure stream, while the direct outlet yielded a flow of concentrated gas products (H_2 , CO and C_2H_4). In this case, the two gas outputs were not

quantified separately, but this is assumed given that the system is very similar to the one described in Chapter 2. As expected, part of the unreacted CO₂ was present in the combined flows of direct and indirect outlets, but a significant fraction was also found at the degassing outlet, mixed with O₂. This should be avoided for a better downstream CO₂ management that allows its recycle, as it is known that CO₂/O₂ mixtures are not easy to separate.¹⁹⁹ The CO₂ was able to exit through the degassing outlet either because of reinjection into the anode chamber from the main reservoir or CO₂ crossover through the Zirfon separator. In addition, some of this CO₂ was probably coming from CO₂R product oxidation at the anode. A test to check which of the two pathways is preferred was performed with a non-mixing C | 1 | DIA | A configuration, aiming to assess the CO₂ crossover degree through the separator and possibly exclude it. However, this system does not represent the CO₂R working conditions because without mixing the catholyte quickly loses its acidity, leading to CO₂ conversion to (bi)carbonate that can electromigrate to the anode, which does not happen under standard acidic electrolysis tests. Hence, it is not straightforward to state which pathway is followed by CO₂ before being vented from the degassing outlet.

Liquid product oxidation at the anode is the main disadvantage of the mixing system. Ethanol and propanol were converted with similar kinetics to acetic acid and propionic acid, respectively, which in turn can be completely oxidized to CO₂. Propionic acid seemed to accumulate in solution slower than acetic acid, a trend that, together with the higher CO₂ molar flow measured during the propanol test, might indicate a stronger propensity for oxidation to CO₂. With no intermediates, formic acid was completely oxidized to CO₂ at the end of the test. It is worth keeping in mind that during CO₂ electrolysis, ethanol, propanol and formic acid are simultaneously present in solution, which might lead to competition among them for oxidation at the anode. Even though liquid product oxidation lowers the total FE, this issue can be easily solved by employing catalysts that are selective for gas products like CO (Zn, Ag, Au)⁴⁹ and C₂H₄ (Cu nanodendrites,²⁰⁰ Cu/N-doped carbon²⁰¹), which do not reach the anode due to their low water solubility and efficient evacuation at the gas diffusion cathode.

Increasing the temperature of the electrolyte improved the $|E_{\text{cell}}|$. The observed decrease in cell potential can be attributed to the improved kinetics of CO_2R at the catalyst and to the better mass transport of CO_2 to the cathode. The mass transport of CO_2 depends on two parameters that have opposite trends when temperature varies.⁹⁶ The first is the CO_2 diffusion coefficient, which increases with rising temperature leading to reduced diffusion potentials and the second is CO_2 solubility, governed by the van't Hoff equation, which decreases with the temperature. Employing GDEs partially compensate for the lower solubility due to the reduced diffusion length for CO_2 , but if the temperature increases excessively this effect might be nullified by the lower solubility. Therefore, it is important to find the right temperature that keeps the two effects balanced. H_2 FE can be used as an indicator for CO_2 mass transport limitation, given that as soon as CO_2 depletion at the cathode occurs the selectivity for hydrogen evolution starts to rise.⁹⁶ Even though it was not in the scope of this work to deeply analyze how these parameters affect the system, it seems that here the transport of CO_2 is sufficient for CO_2R to be predominant at the cathode at each temperature tested. However, when going from 20 to 60 °C, H_2 production increased slightly while CO and C_2H_4 selectivity decreased, which might indicate that CO_2 mass transport limitation is approaching (Figure 3.11b).

3.4 Conclusions

The reactor optimization presented in this chapter details a strategy to lower the overall cell voltage by tackling the resistive components of a CO_2 electrolyzer. With an applied current density of -200 mA cm^{-2} , the $|E_{\text{cell}}|$ of a commonly employed Nafion-based gas-fed flow cell (3.61 V) could be decreased to reach a value (2.89 V) approaching those needed for scale-up and commercialization. This was made possible by reducing the resistance of two main components of the cell: the membrane and the electrolyte solution. The Nafion membrane was replaced by Zirfon, a non-ion selective diaphragm opposing less resistance to the passage of charges, which allows any species to cross from one side of the cell to the other. Because of

this, the electrolyte was also re-evaluated to obtain a system with the same catholyte and anolyte composition. KCl and H₂SO₄ (major cathodic and anodic species in the Nafion-based reactor) were replaced by Cs₂SO₄, a conductive and soluble salt able to provide a high ionic strength. Having the same electrolyte species in both half-cells enabled a continuous external mixing to prevent electrolyte composition and pH shift over time. The resistance introduced by the Cs₂SO₄ solution can be lowered by adopting a one-gap configuration, thereby reducing the distance separating cathode and anode. Finally, rising the temperature of the solution increased its conductivity, resulting in a low $|E_{\text{cell}}|$. Considering parameters such as the working temperature, the evolution of the electrolyte over time and the cell voltage is fundamental to build robust and efficient systems that can bring CO₂ electrolysis out of the lab and towards commercialization.

Another important aspect for the CO₂R scale-up is the product output of the reactor. Ideally, an electrolyzer should have unit selectivity towards a single carbon product to avoid separation costs and undesired side reactions. In particular, multicarbon products (ethylene, ethanol, propanol) are sought after for their high added value and wide use in the industry. The next chapter will deal with the modification of the catalyst surface to direct the selectivity of the reactor towards multicarbon products.

Chapter 4

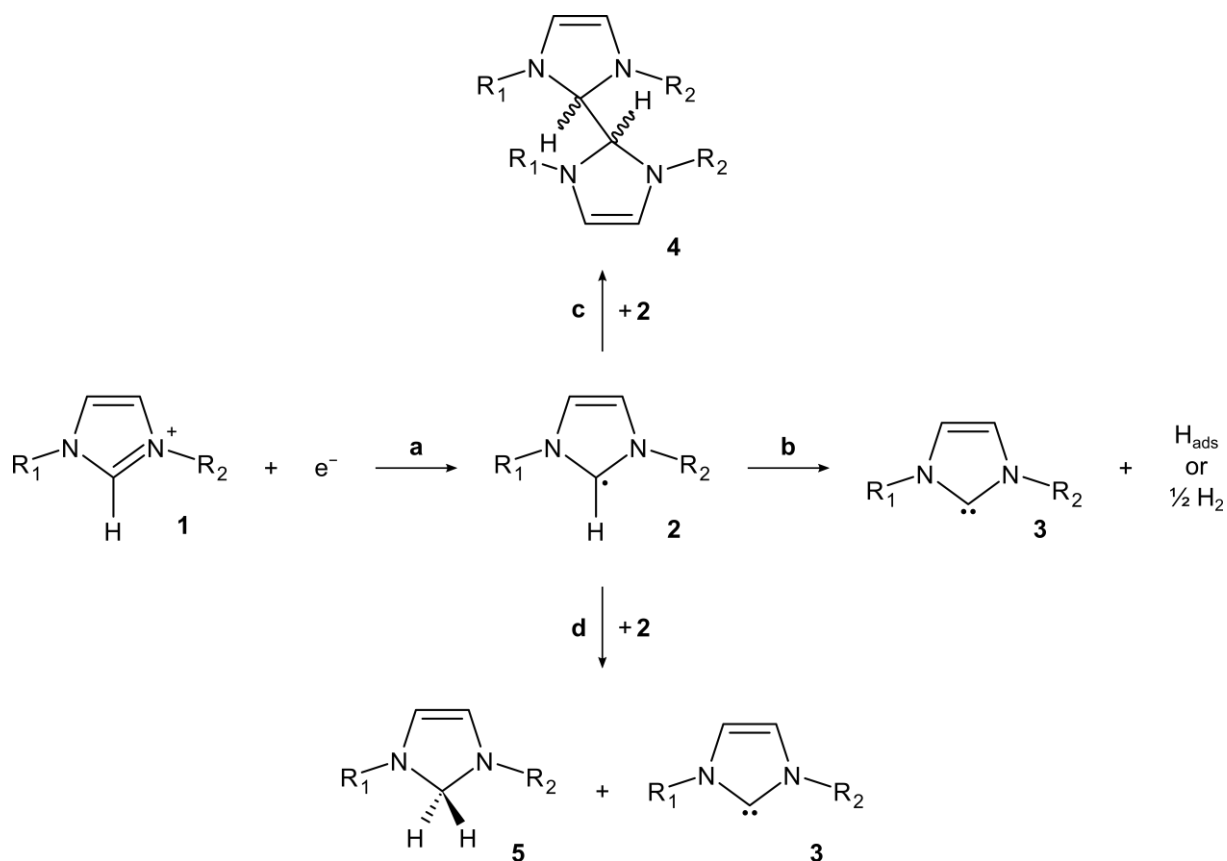
Surface Modification

Section 4.2 of this chapter was written on the basis of the following paper: *Tuning Selectivity of Acidic Carbon Dioxide Electrolysis via Surface Modification*, by Elli Vichou, Alessandro Perazio, Yanis Adjez, Maria Gomez-Mingot, Moritz Schreiber, Carlos Sanchez, and Marc Fontecave, *Chem. Mater.* **35**, 7060–7068 (2023).²⁰²

4.1 Introduction

Cu is a unique transition metal for CO₂R as it significantly catalyzes C-C bond formation and thus is able to yield multicarbon products, which are sought after for their high added value and their wide use in the industry as chemical feedstock. Despite this, CO₂R on copper is intrinsically unselective and a variety of products are simultaneously formed (CO, HCOOH, C₂H₄, C₂H₅OH, C₃H₇OH). Many strategies have been employed to steer the selectivity from C₁ towards C₂₊ products such as alloying,^{203,204} dopant introduction,²⁰⁵ crystal facet selection,^{206–208} defect engineering,²⁰⁹ surface morphology,^{59,210} oxidation states combination,^{57,211} and surface modification.^{212–214} The latter is an interesting way of tuning activity and selectivity as molecules and materials can be carefully selected and characterized to link their structure to the modified catalytic performance (structure-activity relationship).²¹⁵ In particular, the

influence that molecular species have on CO₂R has been studied by immobilization on various electrodes with promising effects on the catalyst activity, such as CO₂R enhancement by stabilization of reduced intermediates²¹⁵ and HER suppression.²¹⁶ The surface modifiers are usually small organic molecules encompassing, among others, thiols,^{216–218} amines,^{218,219} and substituted heterocycles.^{220–224} Ionic liquids (ILs) have been extensively employed in electrochemical applications,²²⁵ with special attention given to those incorporating 1,3-dialkylimidazolium cations due to their high conductivity and low viscosity.²²⁶ Rosen and coworkers were the first to report that IL addition to the electrolyte could lower the overpotential for CO₂ conversion to CO.²²⁷ Since then, ILs effects on CO₂R, especially those based on 1,3-dialkylimidazolium, were explored mostly on silver^{228–230} and gold electrodes^{231,232}. Other than employing ILs as pure electrolytes or solutes in solution, the surface of electrodes can be functionalized by immobilizing ILs through diazonium reactions,²³³ thiol groups in self-assembled monolayers²³⁴ and covalent grafting²³⁵. Investigations regarding copper electrodes functionalization for CO₂R are more recent and have been mostly restricted to neutral electrolyte H-cells^{236,237} and alkaline gas-fed flow cells,^{238,239} while exploration in acid conditions, which would favor CO₂ conversion to products, is still lacking with the exception of some recent reports^{240,241} that were published during the investigations leading to the results described below. In particular, it was reported that, upon reduction, an organic layer derived from 1-ethyl-3-methylimidazolium tetrafluoroborate (EMIMBF₄) could be deposited on a copper electrode, resulting in enhanced CO₂R and suppressed HER.²⁴² 1,3-dialkylimidazolium cations are prone to reduction when a suitable negative potential is applied (Scheme 4.1).^{243,244} Upon one electron transfer to a 1,3-dialkylimidazolium (**1**) a neutral radical centered on C2 is formed (imidazol-2-yl, **2**), with C2 being the most electron-deficient carbon atom of the ring,²⁴⁵ which can decompose to the corresponding *N*-heterocyclic carbene (NHC, imidazole-2-ylidene, **3**) and H₂ as a side product. Recombination and disproportionation of two one-electron reduced radicals (**2**) are other possible pathways, giving a neutral dimeric species (1,1',3,3'-tetraalkyl-2,2',3,3'-tetrahydro-1H,1'H-2,2'-biimidazole, **4**) and a neutral monomer (1,3-dialkyl-2,3-dihydro-1H-imidazole, **5**) plus **3** as products, respectively.^{243,244} Reduction of the initial EMIM⁺



Scheme 4.1 Reaction pathways following the one-electron reduction of a 1,3-dialkylimidazolium (**1**) molecule. (a) Reduction of **1** results in imidazol-2-yl (**2**) formation; (b) **2** decomposes into imidazole-2-ylidene (**3**) and H₂; (c) recombination reaction with **2** giving 1,1',3,3'-tetraalkyl-2,2',3,3'-tetrahydro-1H,1'H-2,2'-biimidazole (**4**); (d) disproportionation reaction with **2** forming 1,3-dialkyl-2,3-dihydro-1H-imidazole (**5**) and **3**. Adapted from ref. 243.

to obtain the radical **2** seems to be necessary to form the layer on the electrode surface. The reason for the improved CO₂R activity is not yet completely elucidated. It has been proposed that the imidazolium could stabilize negatively charged intermediates resulting from CO₂R (namely CO₂⁻) through electrostatic interactions.²⁴⁶ The ion pairing formation is thought to be driven by hydrogen bonding between the protons at the C2,²⁴⁶ C4²²⁹ and C5²²⁹ positions of the positive ring and the negatively charged oxygen atoms of CO₂⁻, which lowers the activation barrier for the first electron transfer to CO₂. Alternatively, the one-electron reduced radical **2** is reported to form adducts with CO₂ at the C2 position, thereby facilitating reactant activation.^{226,242,243} DFT calculations concerning CO₂R with EMIM⁺ on Cu showed that the

reduction potential to form the radical coincides with the onset of CO₂ reduction, suggesting an IL-initiated catalysis.²⁴²

As described before, electrolytes containing alkali metal cations are needed in acid solutions to efficiently suppress HER during CO₂R. However, high salt concentrations used in combination with CEMs lead to additional voltage drops, as the cations quickly saturate the negatively charged groups of the membrane increasing its resistance. In addition, M⁺ salts can form precipitates on the cathode and the membrane, which negatively impact the performance.²⁴⁷ The key element for suppressing HER is the positive charge that the cations provide close to the electrode, which role could be mimicked by other charged species. Once reduced and deposited on the electrode surface, it is possible that the imidazolium re-gains its positive charge and acts as a promoter for CO₂ reduction, avoiding the need for metal cations.

A different strategy to suppress HER and boost CO₂R consists in deliberately making the surface of the catalyst highly hydrophobic. By making the electrode less wettable, water and protons are partially prevented from reaching the catalyst, resulting in H₂ evolution limitation. In addition, the hydrophobicity enhances CO₂ permeation through the GDE, allowing the formation of an extended gas network around the Cu nanoparticles, which favors CO₂R.²¹⁶ Long alkyl chains bearing an anchoring group are well suited to increase the hydrophobicity of metal electrodes. Surface modification of copper has been reported using organothiols,^{248–250} organoselenols^{251,252} and phosphonic acids.^{253,254} As a notable example, modification of copper dendrites with 1-octadecanethiol was reported to suppress HER and favor multicarbon products selectivity as a result of the highly hydrophobic catalyst surface.²¹⁶ When considering the stability of these molecular anchors, phosphonic acids have a lower tendency to be protonated in acid conditions (pK_{a1} ~ 2-3, pK_{a2} ~ 8-9)²⁵⁵ compared to thiols and selenols (pK_a ~ 10-11 and pK_a ~ 7, respectively). In addition, the binding of phosphonic acids on the surface occurs in a tridentate mode,²⁵⁶ which should impart a stronger stability compared to the monodentate fashion of thiols and selenols. Despite this, a study investigating the interaction of tetradecylphosphonic acids with Ag nanoparticles indicated that a cathodic potential sweep

results in dissociation of the molecules from the surface.^{257,258} Nevertheless, the phosphonic acids remained in the proximity of the surface in virtue of weak hydrophobic interactions between the long alkyl chains. Therefore, long alkyl chains attached to phosphonic acid groups seem suitable to tune the wettability of copper electrodes.

In this chapter, the results obtained by the surface modification of commercial copper nanoparticles with 1-ethyl-3-methylimidazolium tetrafluoroborate (EMIMBF₄) and tetradecylphosphonic acid (TDPA) will be described (Figure 4.1), representing one of the first studies dealing with copper surface modification for acidic CO₂R. The results shown in Section 4.2 have been collected in collaboration with Dr. Elli Vichou.

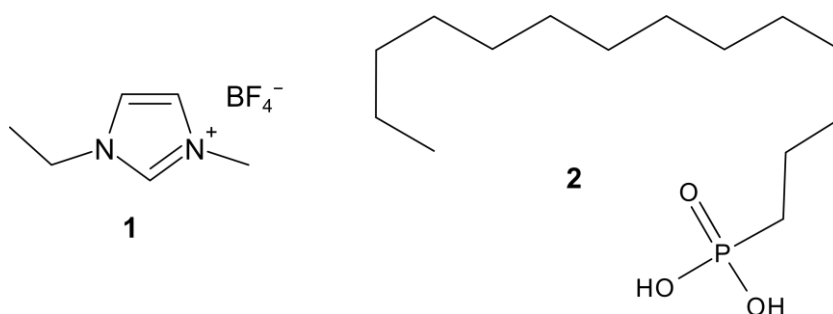


Figure 4.1 Illustration of 1-ethyl-3-methylimidazolium tetrafluoroborate (EMIMBF₄, **1**) and tetradecylphosphonic acid (TDPA, **2**).

4.2 Results: ionic liquid modification

The gas-fed flow cell setup used for the following experiments is described in Chapter 2 (Figure 2.15). CO₂ reduction was achieved on a GDE composed of a layer of commercial Cu NPs (size around 40-60 nm) deposited on a porous PTFE membrane. The cathode was interfaced with the optimized catholyte from Section 2.2.2 (3 M KCl / 0.5 M H₂SO₄, pH 0.9), while the Ni-foam anode was in contact with an alkaline anolyte (2.5 M KOH, pH 14). A bipolar membrane was used as a compartment separator. The focus here is on the cathode surface modification, thus the effects of the BPM, pH and CO₂ regeneration will not be discussed, as they are already detailed in Chapter 2.

4.2.1 Cathode modification with EMIMBF₄

First, the activity of a 0.5 M EMIMBF₄ aqueous solution on the Cu GDE was assessed by LSV under inert atmosphere. When the cathodic potential is swept towards negative values, a reduction curve appears with an onset at ca. -1.2 V vs. Ag/AgCl, corresponding to the one-electron reduction of EMIM⁺ (Figure 4.2). Previous results obtained on a glassy carbon electrode showed that around a potential of -1.2 V vs. Ag/AgCl EMIM⁺ can receive an electron from the cathode and form a radical species that could establish a covalent bond with the electrode surface (Figure A.4). As described below, the presence of discrete imidazolium molecules grafted on the Cu surface cannot be unequivocally confirmed. Nevertheless, upon electroreduction, an EMIM-derived organic layer could be deposited on the catalyst.

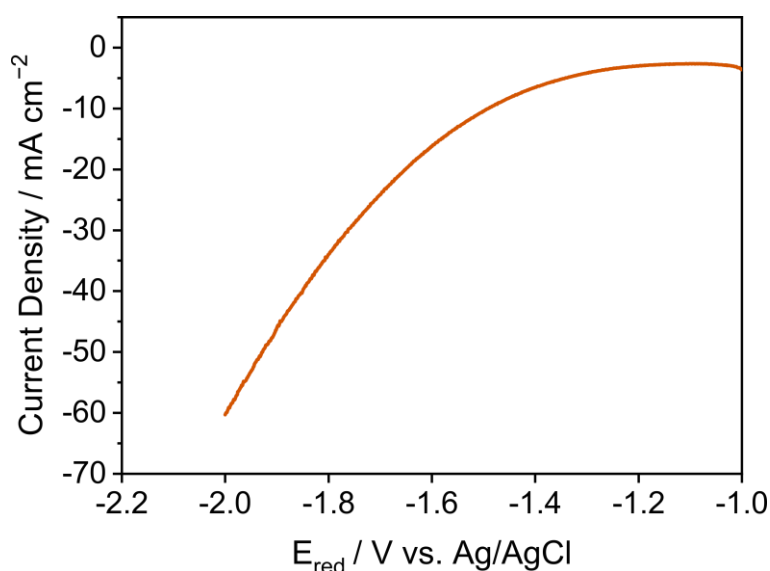


Figure 4.2 EMIM⁺ reduction during a negative LSV scan of a 0.5 M EMIMBF₄ solution. Scan rate: 25 mV s⁻¹.

EMIMBF₄ deposition can be achieved with two different methods: static deposition and flow deposition. The static method involves a separate container dedicated to the formation of the IL organic layer. The Cu GDE is placed in a 0.5 EMIMBF₄ solution under inert atmosphere and current is applied to allow EMIM⁺ reduction. Then, after rinsing, the modified electrode can be placed in the flow cell for testing. Instead, the flow deposition is already carried out in the flow cell, where the EMIMBF₄ solution is flown in the catholyte compartment and the IL deposition

is achieved once again by applying constant current. Among the two, the flow method proved to be superior in terms of performance of the resulting electrode. The GDE needs to be manipulated more for the static deposition and might experience mechanical stress, while for the flow method the GDE is placed in the reactor and it is not moved until the end of the experiments. Therefore, only the flow deposition will be discussed.

Optimization of the EMIMBF₄ deposition (Figure 4.3) was performed by varying the applied current density (from -10 to -50 mA cm⁻², 10 min for each test) and the duration of the

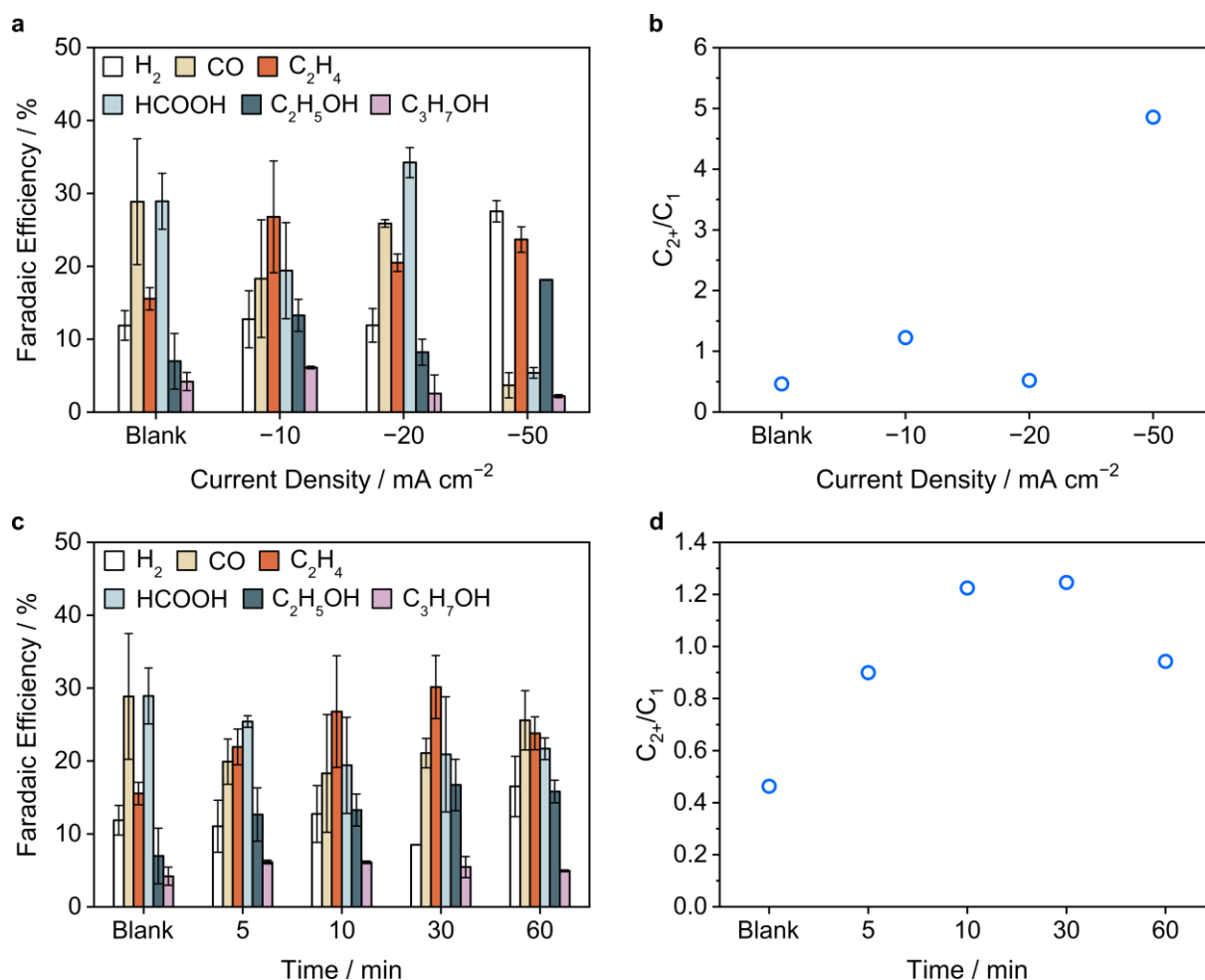


Figure 4.3 Effects on the modified electrodes performance as a consequence of applying different current densities for 10 min during the deposition (a, b) and varying the deposition time with a constant current density of -10 mA cm⁻² (c, d). (a, c) show the product selectivity, while (b, d) show the multicarbon to monocarbon product ratio. The IL deposition is performed under Ar, while the FEs are recorded after 30 min electrolysis at -200 mA cm⁻² with a 3 M KCl / 0.05 M H₂SO₄ catholyte (pH 0.9) and a CO₂ feed flow rate of 10 mL min⁻¹. Blanks are added for reference.

deposition time (from 5 to 60 min, constant current density of -10 mA cm^{-2}); the performance of the resulting electrodes was then assessed via CO_2R product selectivity during acidic electrolysis. There seemed to be a non-linear trend concerning the selectivity when changing the deposition current density (Figure 4.3a), as the FEs for multicarbon products (ethylene, ethanol and propanol) increased at -10 mA cm^{-2} from that of the blank (unmodified electrode), decreased at -20 mA cm^{-2} and then increased again at -50 mA cm^{-2} . Even though a very high multicarbon (C_{2+}) to monocarbon (C_1) product ratio was obtained at -50 mA cm^{-2} (Figure 4.3b), here H_2 formation was more pronounced. At -10 mA cm^{-2} , C_{2+} products were still favored ($\text{C}_{2+}/\text{C}_1 > 1$) while H_2 evolution could be limited, giving an overall better performance. Therefore, -10 mA cm^{-2} was the current density value chosen for the following tests. Varying the deposition time at constant current density (Figure 4.3c) gave a volcano plot, with the highest FEs for C_{2+} products obtained after 30 min, which is also the point with the highest C_{2+}/C_1 ratio (Figure 4.3d). H_2 evolution was not significantly affected, except after a long deposition time (60 min). In general, Cu nanoparticles modification with EMIMBF_4 favored C_{2+} product formation, with the best performance found when the deposition was carried out with a current density of -10 mA cm^{-2} applied for 30 min.

4.2.2 CO_2R with the IL-modified electrode

The effect of the EMIM-modification was assessed by comparing the product selectivities of the blank with those of the modified GDE at different current densities (Figure 4.4). The IL deposition conditions were the ones optimized in the previous section (flow deposition, -10 mA cm^{-2} applied for 30 min, 0.05 M EMIMBF_4 solution). The blank presented a general higher FE for monocarbon products (CO and HCOOH , Figure 4.4a), while the modification favored the production of ethylene, ethanol and propanol at all current densities tested (Figure 4.4b). In addition, the selectivity for multicarbon products increased with increasing current in both cases. Comparison of the cathodic potential values of the blank and of the modified electrodes allowed to exclude that the difference in catalytic activity between the two stems from an altered potential of the cathode resulting from the deposition. Figure 4.4c helps to better

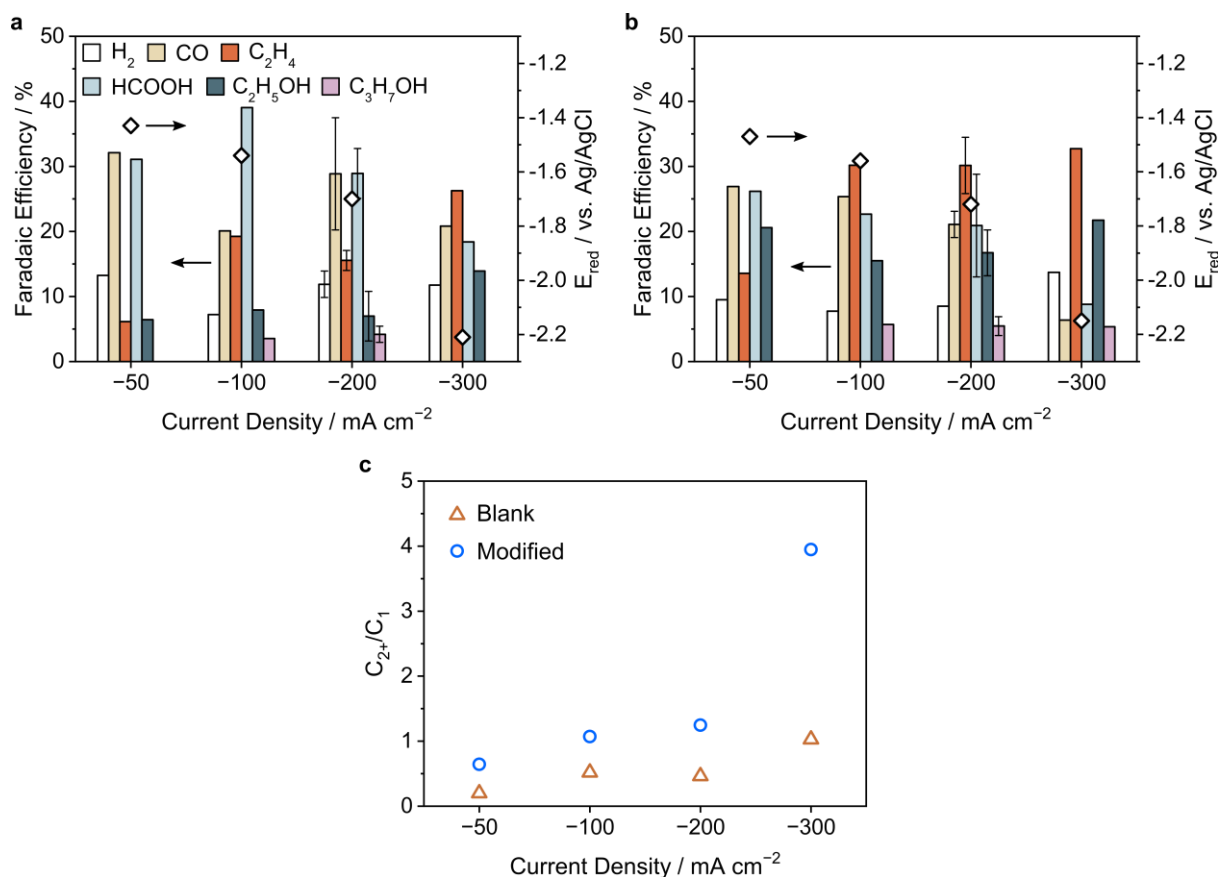


Figure 4.4 Product selectivity of the blank (a) and EMIM-modified (b) GDEs. (c) Comparison of multicarbon to monocarbon product ratio for the blank (triangles) and the modified electrode (circles). The electrolysis were performed for 30 min in a 3 M KCl / 0.05 H_2SO_4 catholyte with a feed flow rate of CO_2 of 10 mL min^{-1} .

visualize the change in selectivity thanks to the C_{2+}/C_1 product ratio, which was higher for the IL-modified electrode at each current density tested. In particular, the ratio found at -300 mA cm^{-2} for the modified electrode reached a remarkable value of 4, meaning that multicarbon products selectivity can be efficiently boosted at the expenses of monocarbon products.

The long term stability of the system was tested during a 5 h electrolysis at -200 mA cm^{-2} (Figure 4.5). Both the blank (Figure 4.5a) and the modified electrode (Figure 4.5b) displayed a good stability in terms of cathodic potential and product selectivity over the course of the experiment, which might indicate no or limited loss of the organic layer from the surface. As already seen previously, the unmodified copper catalyst yields higher FEs for CO and HCOOH, while the presence of the layer increases the long term selectivity for ethylene, ethanol and propanol. In addition, the potential could be maintained at a similar value for the two cases

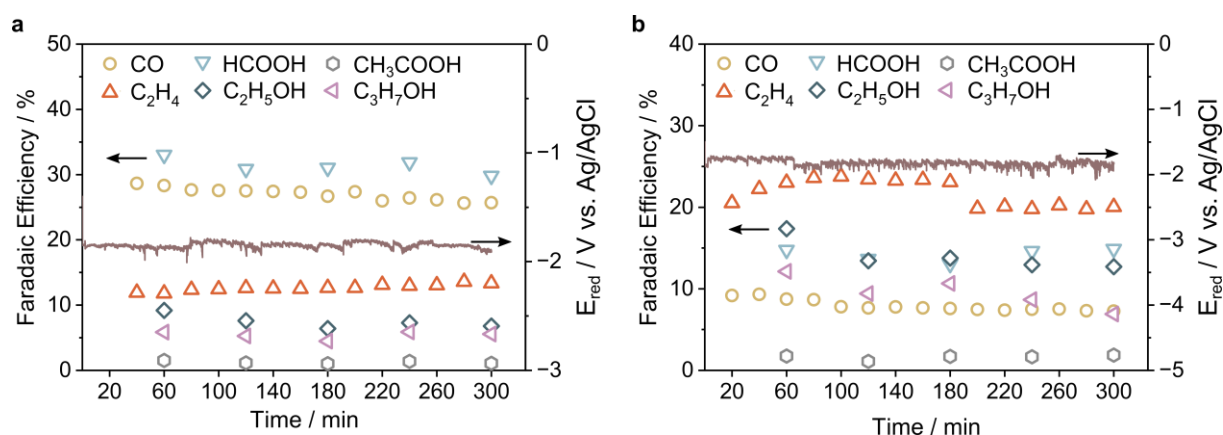


Figure 4.5 Evolution of CO_2R product selectivity and E_{cath} over the course of a 5 h electrolysis for the blank (a) and the EMIM-modified electrode (b). Test performed in a 3 M KCl/0.05 H_2SO_4 catholyte with a feed flow rate of CO_2 of 10 mL min^{-1} and a current density of -200 mA cm^{-2} .

(1.85 V for the blank and 1.82 V for the modified electrode vs. Ag/AgCl), highlighting once again that the modified selectivity is not due to a difference in potential introduced by the organic layer.

4.2.3 Characterization of the EMIM-modified electrode

Scanning electron microscopy (SEM) analysis of the modified electrode surface was used to characterize the nature of the EMIM-derived layer and to assess the effect of electrolysis on the modified electrode. SEM images (Figure 4.6) showed the formation of a thin layer uniformly covering the Cu nanoparticles after deposition (Figure 4.6a and b), and that the total thickness of the GDE catalyst layer (organic layer + nanoparticles) was around $8 \mu\text{m}$ (Figure A.5). After 30 min of electrolysis, the presence of the layer could not be visually confirmed by looking at

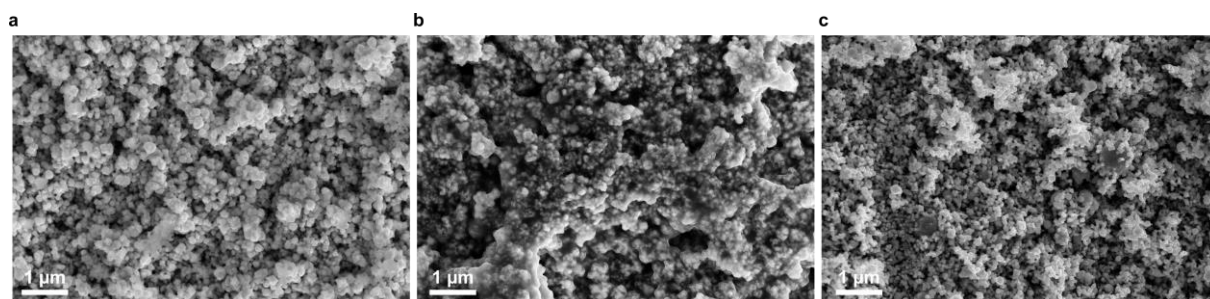


Figure 4.6 SEM images of the blank (a), EMIM-modified electrode (b), and EMIM-modified electrode after electrolysis (c) carried out for 30 min at -200 mA cm^{-2} with a feed CO_2 flow rate of 10 mL min^{-1} .

SEM pictures (Figure 4.6c), but its permanence can be argued according to other kinds of analysis, shown below. Energy dispersive x-ray spectroscopy (EDX) clearly showed the introduction of nitrogen after EMIMBF₄ deposition and boron could also be seen, albeit with a small peak (Figure 4.7a and b). Copper, oxygen, carbon and fluorine can be linked to the catalyst, the IL and the supporting PTFE membrane (Cu from the nanoparticles; O from CuO formation due to a slight catalyst oxidation between the deposition and the EDX measurement; C and F from the PTFE and EMIMBF₄). All of the peaks corresponding to the mentioned elements could be retained after electrolysis, except N, with the addition of K and Cl peaks, likely due to the KCl electrolyte (Figure 4.7c). The absence of nitrogen post-electrolysis might be just a detection error, because further characterization and analysis proved that the layer and its imidazolium features are retained even after performing CO₂R. EDX elemental mapping

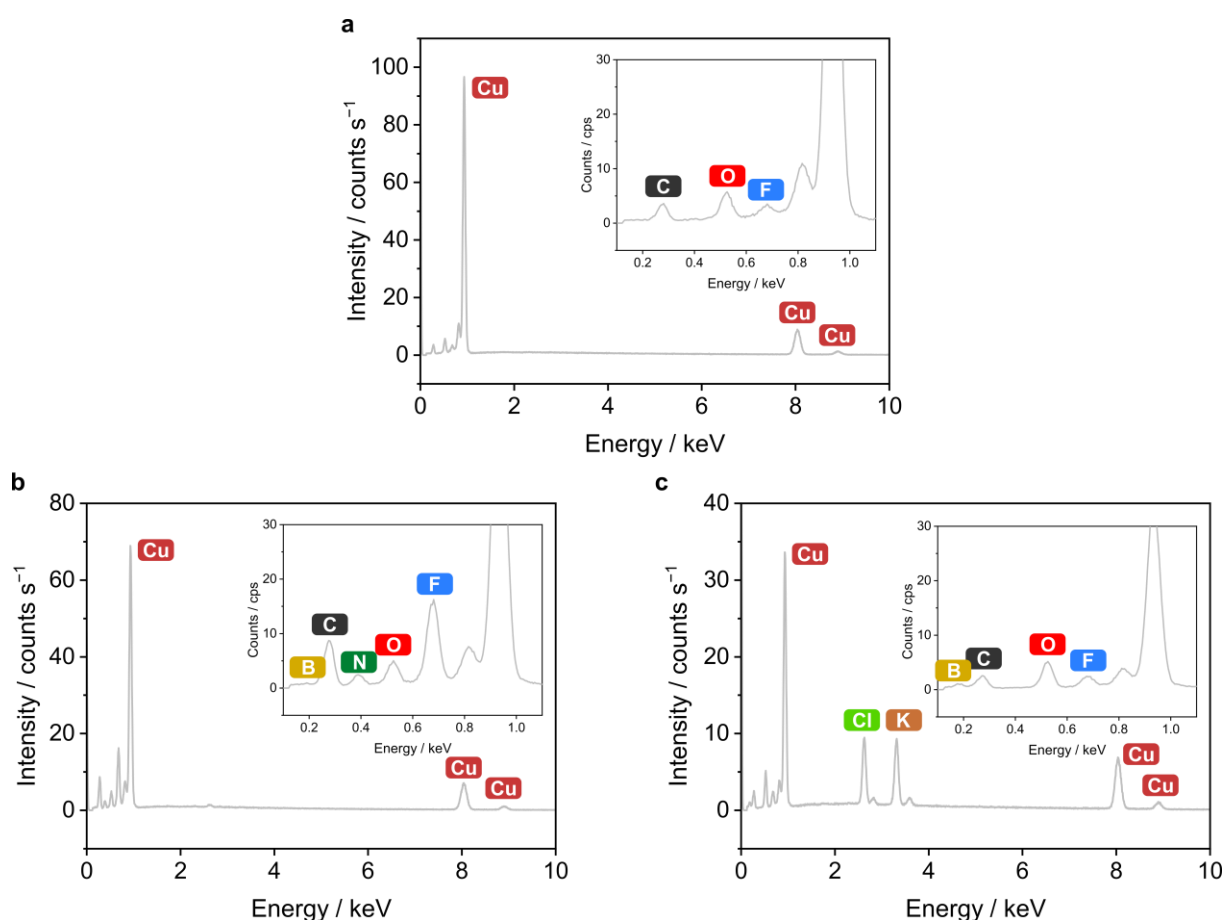


Figure 4.7 EDX analysis of the blank (a), modified electrode (b) and modified electrode after electrolysis performed for 30 min in a 3 M KCl / 0.05 M H₂SO₄ catholyte at -200 mA cm^{-2} with a feed CO₂ flow rate of 10 mL min^{-1} (c). The inserts show a zoom of the zone from 0 to 1 keV.

showed how N and B, clear signatures of the EMIM species, were homogeneously distributed on the Cu surface after deposition (Figure 4.8). In addition, F was also evenly distributed on the surface. X-ray photoelectron spectrometry (XPS) was used to identify the nature of the nitrogen present on the surface, and whether it was consistent with an imidazolium structure. Once more, N and B were found only in on samples that had undergone deposition (Figure 4.9a, b and c). In addition, the deconvolution of the N 1s portion of the spectrum (Figure 4.9d and e) revealed three peaks with a binding energy of 398.9 eV (Cu-pyrrolic N, purple), 400.5 eV (free pyrrolic N, yellow) and 401.7 (pyridinic N, orange), which match with previously reported data concerning imidazolium species immobilized on metallic surfaces.^{237,259–261} XPS results also indicated that the copper was not affected by the EMIM deposition nor by the electrolysis, presenting the same unchanged peaks (Figure 4.9f). The attenuated total reflectance-Fourier transform infrared (ATR-FTIR) spectrum (Figure 4.10a and b) of the modified electrode displayed bands that are absent from that of the blank. Comparison with the reference spectrum of a EMIMBF₄ solution confirmed that an EMIM-like structure is present on the surface of the catalyst: band at 1165 cm⁻¹, corresponding to methyl-N and ethyl-N stretching; band at 1564 cm⁻¹, characteristic of C=C stretching; bands at 3118 cm⁻¹ and 3158

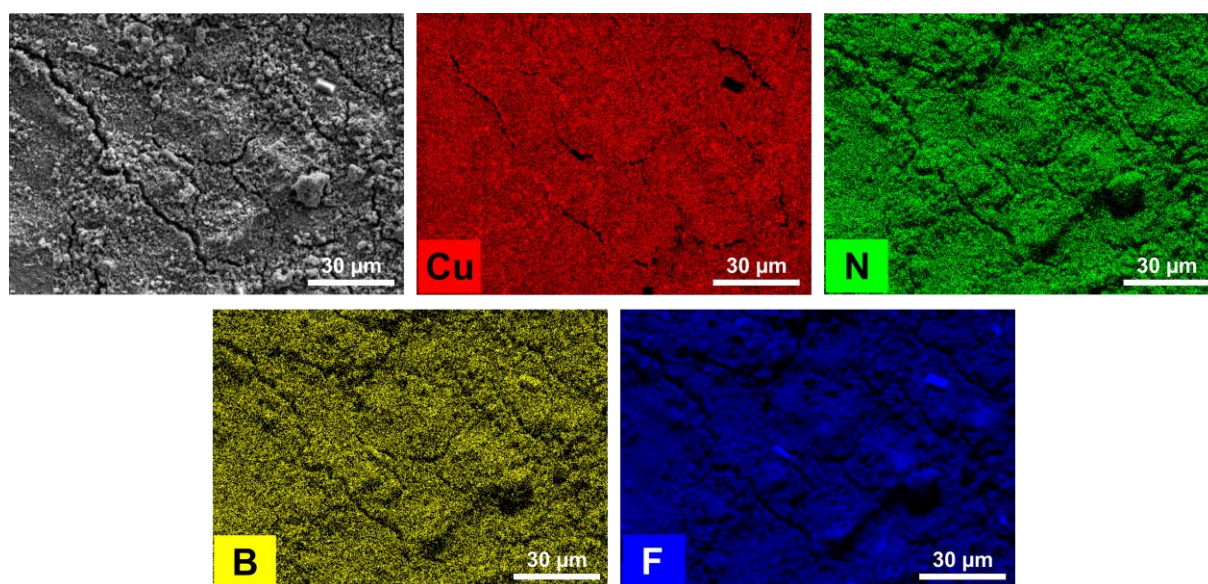


Figure 4.8 EDX elemental mapping of the catalyst surface after deposition. Bare SEM image (grey), copper (red), nitrogen (green), boron (yellow) and fluorine (blue).

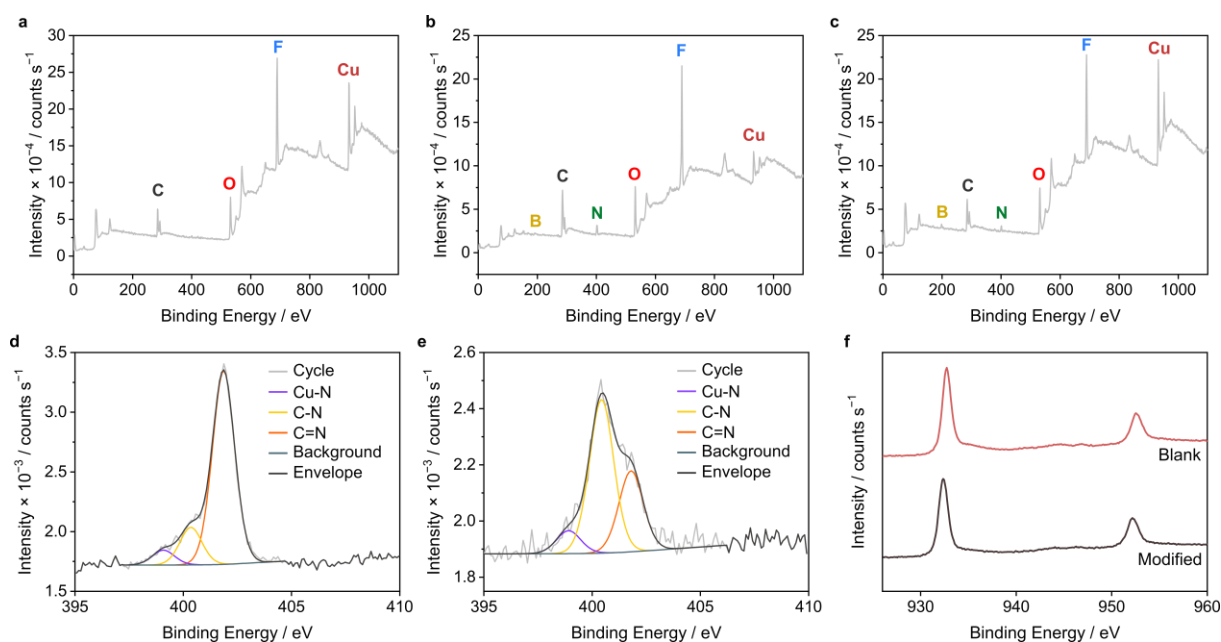


Figure 4.9 XPS survey: blank (a); EMIM-modified electrode (b); EMIM-modified electrode after electrolysis (c). XPS high-resolution spectra of N (1s): EMIM-modified electrode (d), Cu-pyrrolic N (purple), free pyrrolic N (yellow), pyridinic N (orange); EMIM-modified electrode after electrolysis (e). XPS high-resolution spectra of Cu (2p): blank (f, red); modified electrode after electrolysis (f, brown). Electrolysis performed for 30 min in a 3 M KCl / 0.05 M H₂SO₄ catholyte at -200 mA cm^{-2} with a feed CO₂ flow rate of 10 mL min^{-1} .

cm^{-1} associated with C2-H stretching and C4-H/C5-H stretching of the imidazolium ring, respectively.^{262,263} Finally, the band at 1010 cm^{-1} corresponds to the counter anion BF_4^- . Notably, the characteristic signals (C-H stretching around 2800 cm^{-1}) corresponding to the recombination dimer (**4**, Scheme 4.1) were absent in the yellow trace, excluding the possibility of having an organic layer consisting of dimeric structures.²⁶⁴ Further proof of the fact that radical **2** dimerization was not predominant is the presence of aromatic signals (C-H stretching at 3118 cm^{-1} and 3158 cm^{-1}) associated with the EMIM ring, which would be absent with the non-aromatic dimer. The hydrophobicity of the surface was analyzed by water contact angle (WCA) measurements (Figure 4.11) that showed how the WCA decreased from a value of 156° in the blank to 107° after IL deposition, reflecting more hydrophilic electrode compared to the blank, which is hydrophobic due to the Nafion used as a binder during the GDE preparation. Electrochemical surface area (ECSA) of the different electrodes was determined through double layer capacitance values. The ECSAs of the unmodified and modified electrode were

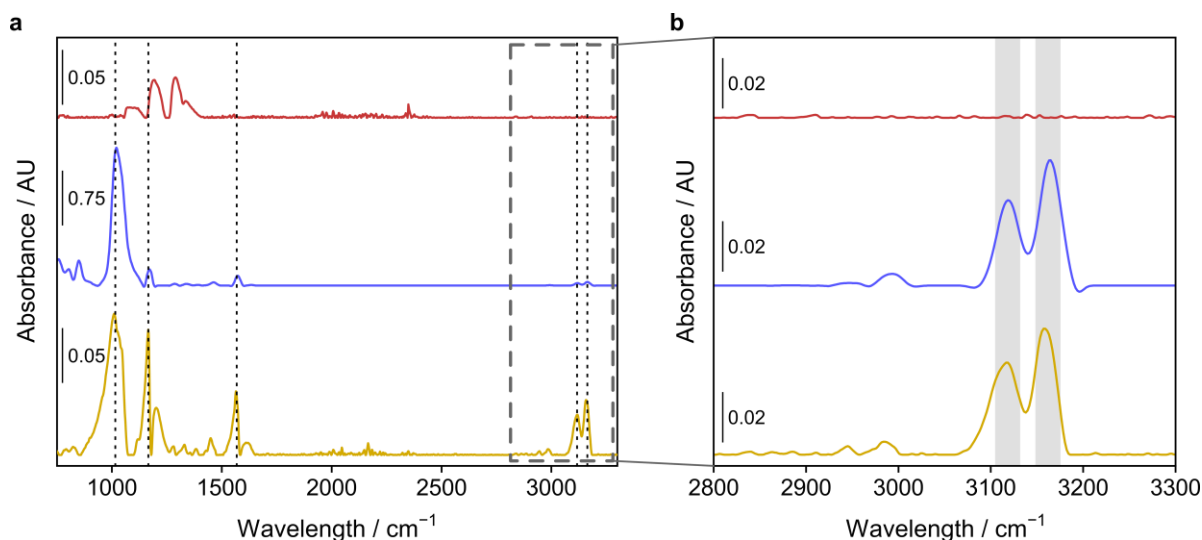


Figure 4.10 ATR-FTIR spectra of the blank in red, EMIMBF₄ solution in blue and EMIM-modified Cu in yellow (a); zoom of the region around 3000 cm⁻¹ (b).

57.2 and 50.3 cm² cm⁻², respectively, indicating that the large area given by the Cu nanoparticles was not significantly influenced by the presence of the IL layer. In addition, the ECSA remains similar even after electrolysis, with a value of 54.9 cm² cm⁻².

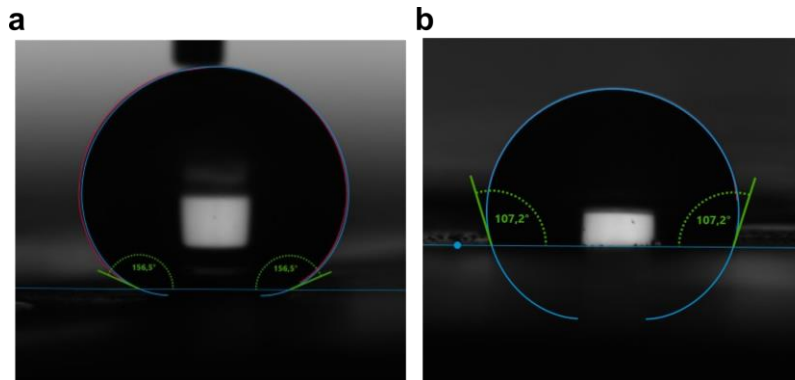


Figure 4.11 Images from the WCA measurement for the (a) blank and (b) IL-modified electrode.

4.2.4 Potassium-free CO₂R

Employing electrolytes with high salt concentrations is important to obtain highly conductive solutions. In addition, the critical role that alkali metal cations play in favoring CO₂R over HER in acidic environments has been detailed in previous sections. However, concentrated solutions may lead to salt deposition on the cathode²⁴⁷ and when a CEM such as Nafion is

used as a separator, M^+ accumulation in the membrane increases its voltage drop, negatively affecting the cell potential (see Section 3.3). Therefore, achieving the same degree of conductivity and CO_2R selectivity without metallic salts in solution is an attractive perspective. Here, CO_2R selectivity with the IL-modified electrode was tested in absence of potassium in solution. First, the HER suppressing effect of K^+ was evaluated and, as expected, absence of K^+ in a 0.1 M H_2SO_4 solution (pH 0.7) resulted in almost 100% FE for H_2 with the unmodified electrode, and addition of KCl gradually increased the selectivity towards CO_2R (up to 60% with 3 M KCl, Figure 4.12). Surprisingly, when the modified electrode was tested in the K^+ -free electrolyte, a total FE for CO_2R products of $(11 \pm 3)\%$ could be obtained, which is roughly comparable to a blank electrode tested in 0.8 M KCl solution. This is remarkable because it indicates HER suppression in a strongly acidic electrolyte solution with no alkali metal cations, an effect that could be ascribed to the positive charge possibly carried by the EMIM-layer exerting a similar effect as K^+ ions.

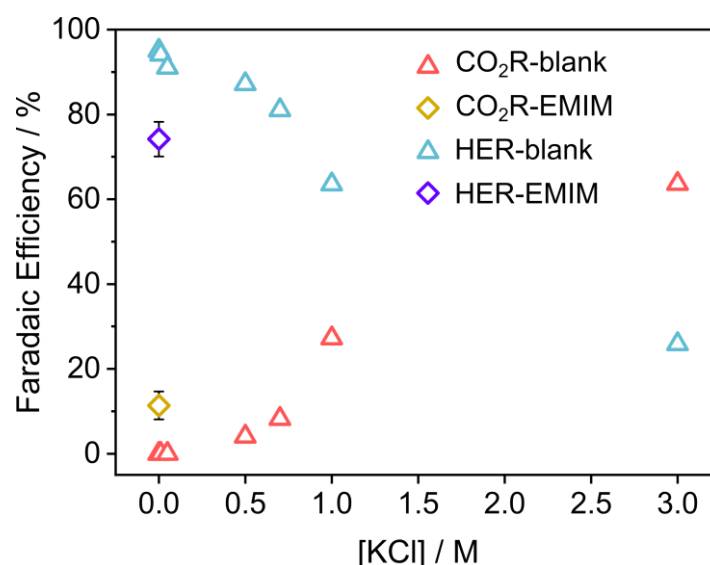


Figure 4.12 Selectivities for CO_2R (cumulative carbon products) and HER. The blank was tested in a 0.1 M H_2SO_4 electrolyte with increasing KCl concentration (0-3 M, pH 0.7-0.9 red and blue triangles); the modified electrode was tested in a 0.1 M H_2SO_4 solution without KCl (pH 0.7, yellow and purple diamonds). Electrolysis performed for 30 min each at -100 mA cm^{-2} with a CO_2 feed flow rate of 10 mL min^{-1} .

4.3 Results: phosphonic acid modification

The results presented in this section were obtained in a gas-fed flow cell featuring an acidic catholyte and an acidic anolyte (3 M KCl / 0.05 M H₂SO₄ and 1 M H₂SO₄, respectively) separated by a Nafion membrane. Commercial copper nanoparticles (size around 40-60 nm) modified with TDPA were used as the cathode, while IrO_x was used as the anode. As this project is still in the exploratory phase, limited data is available and no physical characterization is provided.

4.3.1 Influence of TDPA on CO₂R selectivity

The deposition of TDPA on copper was achieved by a self-assembly method. In brief, different amounts of TDPA were dispersed in methanol by sonication. Then, a standard amount of CuO nanoparticles was added (around 45 mg) to the different dispersions to obtain several TDPA/CuO ratios, and the immobilization on the surface was attained after a second sonication step at controlled temperature ($42 \pm 1^\circ \text{C}$). Four different ratios ($\mu\text{mol TDPA/mg CuO}$) were obtained: 0.5, 1, 2.5 and 5. The modified CuO nanoparticles were tested and evaluated according to the relative product selectivity and cathodic potential (Figure 4.13). Before electrolysis, all GDEs were activated according to the procedure described in Section 2.2.1, thereby reducing CuO to metallic Cu. Electrolysis was performed using electrodes modified with different amounts of TDPA at various current densities (from -50 to -400 mA cm^{-2}). At -50 mA cm^{-2} the blank produced mainly CO and HCOOH, and modifying the surface with a 0.5 ratio did not affect the product distribution (Figure 4.13a). However, when the amount of phosphonic acid increased (2.5 ratio), there was a clear preference for C₂H₄ and C₂H₅OH formation, increasing from a FE of 4% to 25% and from 0% to 8%, respectively, while C₁ products were suppressed. When the ratio was pushed further to a value of 5, HER became predominant, but the higher C₂₊ selectivity over C₁ products could be maintained. With a current density of -200 mA cm^{-2} a similar trend can be found, with the highest selectivity for C₂₊ products (23% and 10% for C₂H₄ and C₂H₅OH, respectively) obtained when a TDPA/CuO

ratio of 1 was employed, even if HER already started to become predominant (Figure 4.13b). Finally, the highest selectivity for C_{2+} products (31% and 14% for C_2H_4 and C_2H_5OH , respectively) shifted to a TDPA/CuO ratio of 0.5 when the current was increased to -400 mA cm^{-2} (Figure 4.13c). In this case, an efficient C_1 products suppression cannot be achieved without a concomitant increase in HER activity. However, the modification with TDPA leads to an increase in the C_{2+}/C_1 products ratio at all current densities and TDPA/CuO ratios tested (Figure 4.13d), showing the positive effect of the modification on the selectivity. The cathodic potential (E_{cath}) relative to each run is shown and it is clear that the modification with phosphonic acid induced a progressive cathodic voltage shift at all current densities tested, evidencing the significant influence that the modification had on the electrode performance.

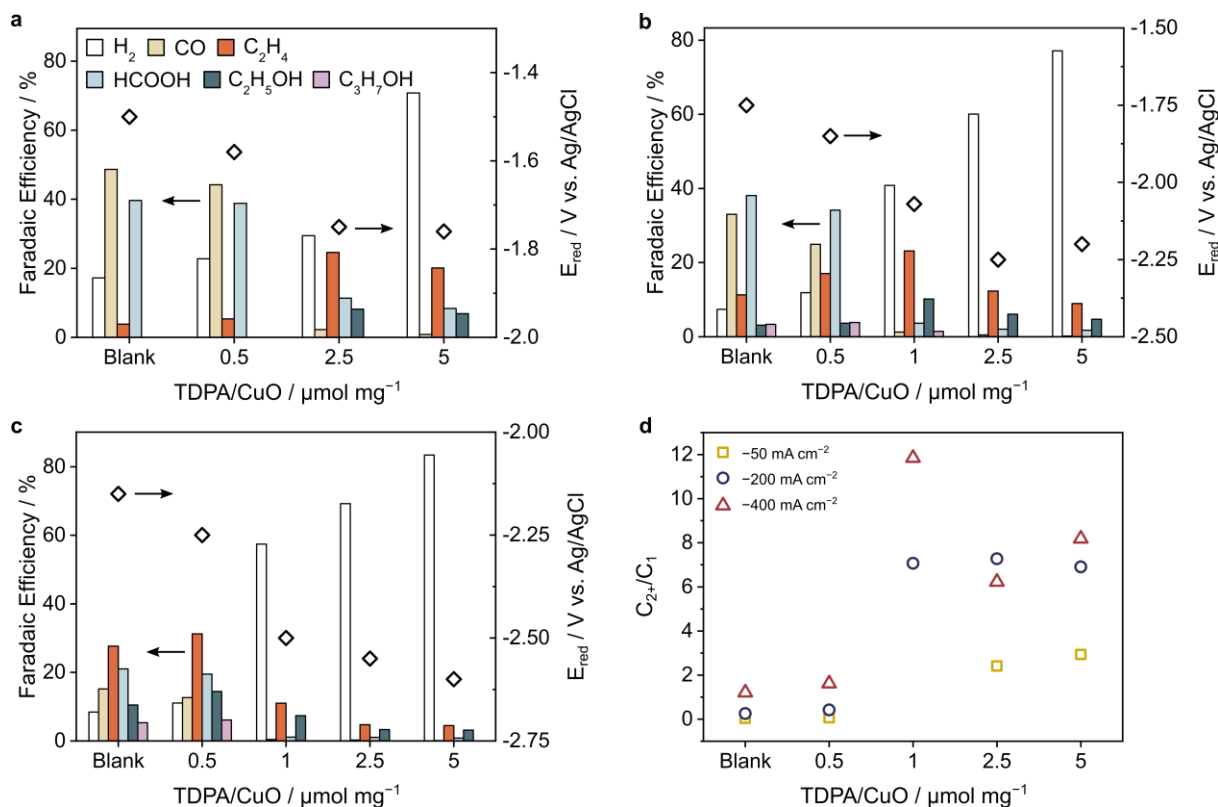


Figure 4.13 Selectivity of the TDPA-modified electrodes at different current densities: (a) -50 mA cm^{-2} , (b) -200 mA cm^{-2} , (c) -400 mA cm^{-2} . (d) Multicarbon over monocarbon products ratios for the three current densities tested. Electrolysis conditions: 3 M KCl / 0.05 M H_2SO_4 (pH 0.9) catholyte, CO_2 feed flow rate 20 mL min^{-1} , 30 min duration.

4.4 Discussion

Characterization data gave interesting insights on the nature of the EMIM-derived layer. SEM images present a porous Cu surface uniformly covered by a thin film, while EDX measurements showed that this layer contains homogeneously dispersed N and B atoms, which very likely come from the EMIMBF₄. The environment around the surface-confined nitrogen atoms was studied in detail via high-resolution XPS (N 1s). The deconvolution of the peak around 400 eV hints towards the presence of three different kinds of N in the layer: (i) pyrrolic N interacting with Cu, (ii) free pyrrolic N and (iii) pyridinic N (Figure 4.14). (i) The lower energy peak (398.9 eV) could suggest a bond or synergy between the pyrrolic N of the imidazolium and the Cu atoms of the electrode (Cu-N);^{237,259} however, another report assigned this peak to a free pyrrolic N, associating the Cu-N interaction to a band lower in energy.²⁶⁰ (ii) The second peak (400.5 eV) was attributed to the same pyrrolic N of the EMIM (C-N)^{237,259,260} that has no interaction with Cu. (iii) Finally, the highest energy peak (401.7 eV) could be linked to pyridinic N (C=N)^{237,259,260} and could also hint to the permanence of the positive charge on the ring.²⁶¹ IR spectra analysis also confirmed that the imidazole structure remains intact after deposition. Moreover, recombination of two radicals to form the dimer **4** (pathway c, Scheme 4.1) can confidently be excluded since the characteristic IR bands associated with the dimeric form were absent. These considerations point towards a modification that involves the formation of an organic layer on the copper surface consisting of discrete EMIM-like structures, which retain the characteristic signatures of imidazolium. In addition, the presence of evenly distributed boron might suggest that BF₄⁻ still acts as a counteranion for a charged imidazolium

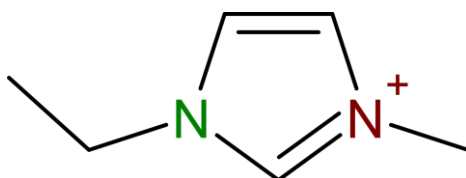


Figure 4.14 Scheme illustrating the two types of nitrogen atoms in EMIM⁺: pyrrolic N (green) and pyridinic N (red).

structure on the surface, supporting the hypothesis that the ring might keep its positive charge even after deposition.

Introducing the organic layer did not modify the potential of the cathode, which means that the selectivity change stems from something inherent to the organic layer more than to a potential difference (a lower potential would result in higher multicarbon products formation as seen in Figure 4.4). However, the exact reason for the IL improved C_{2+} selectivity is not elucidated at present. It is possible that the layer enhances CO_2 concentration at the electrode surface and also stabilizes the adsorbed *CO and other intermediates, hence favoring C-C coupling and increasing multicarbon products formation.^{237,240,265,266} EMIMBF₄ deposition increased C_2H_4 and C_2H_5OH FEs by a factor of 2 at -200 mA cm^{-2} (from 16% to 30%, and from 7% to 17%, respectively, Figure 4.4), while C_3H_7OH FE remained constant around 5%. These values were also retained during long term electrolysis, with the total FE for C_{2+} products increasing from 25% to 45% when the organic modification was present.

HER partial suppression in a K^+ -free electrolyte is an extremely promising outcome of the present work and was only reported once²⁴¹ in concomitance with the publication of the results presented here. Albeit limited for the moment, this effect offers a direct and simple strategy to start reducing, and eventually eliminating, the need for concentrated alkali metal cations in acid solutions to favor CO_2R over HER. Commonly used CEMs like Nafion suffer from a higher resistance when they are employed together with electrolytes containing M^+ species. When the charge is carried mainly by charged alkali metals in solution, an additional voltage penalty is needed to drive them across the membrane, due to their high affinity for the Nafion sulfonic groups (see Section 3.3 for more details). Even if the reactor presented here features a BPM, it is easy to see how this is applicable to an electrolyzer equipped with a Nafion membrane. Concerning the HER suppression, it is possible that the EMIM-derived layer might mimic the effect that metal cations exert on CO_2R . When potassium is present, the polarization of the electrodes attracts positive charges towards the cathode so K^+ can readily adsorb on the Cu surface in virtue of its low hydration number, effectively repelling other positive charges like H^+

and stabilizing negatively charged CO₂R intermediates.¹⁴¹ The IL layer could act in a similar manner, following the hypothesis that the imidazolium ring retains its positive charge after deposition. Nevertheless, this effect is nothing more than speculation for now, and further experiments are needed to confirm the cationic nature of the EMIM-layer. HER inhibition could also stem from an increased hydrophobicity introduced by the organic layer, which would expand the gas network around the Cu nanoparticles, increasing CO₂ concentration at the electrode surface, thereby increasing CO₂R selectivity.²¹⁶ However, WCA tests indicated that after deposition the electrode becomes more hydrophilic, meaning that the alkyl chains are probably too short to introduce a significant degree of hydrophobicity. In addition, the hydrophilicity could suggest the presence of charged species within the layer. It is worth noting that removing metallic salts from solution might reduce the ohmic loss brought by the membrane, but this also lowers the conductivity of the solution, possibly resulting in an overall increase in cell voltage. This could be avoided by, for example, increasing the acid concentration to compensate the decreased ionic strength, given that CO₂R is still favored in even more acidic environments. The reason behind IL modification-induced HER suppression remains unclear for the moment, however this first example has the potential to be optimized further. For instance, when the deposition was performed during three consecutive steps of 10 minutes at -10 mA cm^{-2} , the selectivity for CO₂R in a K⁺-free electrolyte slightly increased from 11% to 15% (mean of three different experiments), indicating that the deposition technique has room for improvement concerning this effect.

Phosphonic acid deposition on commercial Cu NPs has varying effects on the products FE and on the selectivity of CO₂R and HER, depending on the amount used. The immobilization of the phosphonate species on the surface can be argued from the different selectivity obtained by comparison with the blank. It is likely that TDPA interacts with the surface via its polar side, the negatively charged phosphonic acid group. Previous reports describe that phosphonic groups can be anchored on the surface of metal oxides.²⁶⁷ It is worth noting that in the present case, TDPA is attached to the surface of CuO, which is then reduced to metallic Cu. Kim et al.

report how in these conditions the phosphonic acids detach from the metallic surface, but are not subsequently lost in solution. Instead they remain in close proximity of the surface due to the weak interaction between the hydrophobic chains, which keep the layers together.²⁵⁷ The goal of the modification was to increase the surface hydrophobicity. This would lead to an increased gas network around the Cu NPs and thus to an improved selectivity towards CO₂R.²¹⁶ The cathodic shift of the cathode potential seen with an increasing amount of TDPA on the Cu surface could indicate that the difference in product selectivity with the various TDPA/CuO ratios originates in part from the different potential (more negative potentials result in more C₂₊) and in part from TDPA interactions with the surface and/or CO₂ intermediates. This is different from the EMIM deposition case, where the cathode potential was not influenced by the modification. Given the length of the alkyl chain used, the Cu surface becomes highly hydrophobic, to a degree that depends on the ratio chosen, which may explain the more negative potential needed to drive the reaction at a certain current. Increased hydrophobicity should result in HER suppression,²¹⁶ but it was not the case in this study. The cause might be the negative charge of the phosphonate that attracts K⁺ and H⁺, in which case the TDPA layer would act as a proton relay to the surface, thereby favoring HER. Further experiments are needed to confirm this speculation. Nevertheless, the enhancement of selectivity towards C₂₊ products over C₁ products as a result of the modification is promising and the overall FE for CO₂R could be improved by using phosphonic acids with shorter carbon chains, which would give a lower degree of hydrophobicity to the surface, or by adopting different head groups, such as ammonium ions.

4.5 Conclusions

Copper is a unique CO₂R catalyst, able to form multicarbon products at industrially relevant performances, but achieving an optimal selectivity remains a challenge due to the wide variety of products that are obtained at the same time. To solve this problem, electrode

functionalization with small molecules has been explored to try and direct the selectivity towards a single product. In particular, ionic liquids have been used to modify electrodes in neutral and alkaline conditions. Here, EMIMBF₄ was deposited as a layer on Cu NPs via electroreduction. This functionalization resulted in a drastic change in selectivity that favored C₂₊ product formation at the expense of CO and HCOOH, which could be maintained even in a long term tests, indicating the stability of the IL-derived deposit. Various characterization methods were employed to confirm that the layer contains organic species that retain the features of imidazolium rings, thus excluding the dimerization or decomposition of EMIM⁺ after reduction. In addition, XPS analysis suggested close interactions between the nitrogen atoms of the ring and the copper surface. Interestingly, the EMIM-modified electrode was able to carry out CO₂R even in absence of alkali cations in solution, one of the first reported examples of this phenomenon. It is possible that this is the proof of the permanence of a positive charge on the deposited imidazolium, which would act by repelling H⁺ and stabilizing CO₂R intermediates, similarly to metal cations. However, more mechanistic studies are needed to prove this as well as to uncover the reason for the increased multicarbon selectivity.

The preliminary results concerning Cu NPs modification with TDPA were also shown. The selectivity for multicarbon products could be enhanced owing to the modification of the catalyst at all current densities tested, reaching high C₂₊/C₁ ratios. However, this effect was often accompanied by a concomitant increase in H₂ evolution. Even though the selectivity change might be more due to a different cathodic potential rather than to interaction between copper, CO₂ and the phosphonic acid, it might provide useful insights for further molecular modifications. In addition, by altering the chain length and type of charged anchoring group, a strategy to favor multicarbon products while suppressing HER might be found.

Chapter 5

Conclusions and Perspectives

5.1 General conclusions

The aims of this work were to provide strategies to optimize CO₂R electrolyzers for industrial conditions with a view to future commercialization. Through the data presented, crucial parameters including reactant utilization, cell voltage and selectivity were evaluated and improved to advance research towards making CO₂-derived carbon products economically competitive. As a result, some significant findings are reported in the present thesis. Acting as a thread connecting all of the tests performed is the use of a copper catalyst in combination with an acid electrolyte for the reduction reaction. Many reports provide insights and optimization in neutral and alkaline environments, and while they are valuable to obtain a better understanding of the CO₂R process, these conditions are not considered suitable for commercial applications, mainly due to (bi)carbonate formation upon CO₂ reaction with hydroxide ions. Recently, several groups have explored the feasibility of carrying out the reaction in acidic media, which had previously been avoided due to the absence of selectivity towards CO₂R and predominance of HER, with promising results that inspired this research.

The pathways and reactions involving CO₂ within the cell were first evaluated through single-pass conversion and utilization values. The results highlighted how (bi)carbonate formation could not be avoided even in acid (pH < 1) catholytes due to rapid OH⁻ production at high

current densities, which established an alkaline local environment at the electrode surface. However, since the bulk remained acidic, when the (bi)carbonate species diffused away from the cathode they were readily converted back to CO_2 , making the reactant available for reduction. Despite the presence of dissolved CO_2 in the electrolyte, r- CO_2 was not expected to re-react at the cathode, as the alkaline local environment prevents CO_2 from approaching the electrode without reacting with OH^- once again. Instead, the regenerated CO_2 was vented from the reactor as a high purity stream suitable for reinjection in the cell, while the gas products were obtained at a different gas outlet. Recycling the r- CO_2 allowed to achieve high utilization values ($> 85\%$), which diminishes costs for downstream separation from products and reactant recovery. This remarkable result was achieved even with a relatively low single-pass conversion (29%), a parameter that is usually maximized in the literature. Achieving a high SPC is not always the best option as it comes at the expenses of other important parameters like the reactor productivity. Therefore, being able to react the majority of the CO_2 while having an intermediate SPC value is beneficial for the overall performance of the system. In order to obtain this outcome, the electrolysis reactions were carried out at low CO_2 flow rates (1.25 mL min^{-1}) and high current densities (-200 mA cm^{-2}). These conditions were shown to favor the formation of multicarbon products such as ethylene and ethanol ($\text{FE}_{\text{C}_{2+}} > 60\%$). In addition, the electrolyzer stability over time was addressed by employing a bipolar membrane, which maintained a constant composition and pH of the electrolyte over several hours. The drawback of this approach was the very high cell voltage ($|\text{E}_{\text{cell}}| = 4.7 \text{ V}$) arising predominantly from the BPM used in reverse bias (water dissociation at the interlayer) and also from voltage drops due to inefficiencies in the setup. This issue prompted an investigation into methods for reducing the overall $|\text{E}_{\text{cell}}|$ by assessing and optimizing the main sources of resistance within the reactor.

Carrying out CO_2R at low cell voltages reduces the operational cost of the electrolyzer by minimizing the electricity input. This is why E_{cell} optimization has been a central part of the project. To lower the E_{cell} , a critical assessment of the cell components introducing the major

voltage drops was conducted. First, CEMs (namely Nafion), commonly used for acidic CO₂R, were found to be not entirely suitable for the system, as they induce electrolyte imbalances over time and add a significant resistance to the current flow in solution. Thus, the CEM was replaced by a non-ion selective diaphragm (Zirfon), which opposes very little resistance to charge transport. As a non-selective separator, any species was able to cross from one cell compartments to the other, leading again to electrolyte solution imbalances over time due to products and charged species migration. A single electrolyte for both the cathodic and anodic half-cells with external mixing was then adopted as a solution to the problem. Various salts were evaluated as candidates to replace KCl (which cannot be used at the anode due to chlorine gas evolution) and the only one deemed suitable was Cs₂SO₄, owing to its good ionic conductivity and high solubility. The combination of the diaphragm, concentrated Cs₂SO₄ solution and electrolyte mixing, afforded a stable system with a significantly low cell voltage. To further decrease the internal resistance of the electrolyzer, the distance between the electrodes was decreased (from 8.5 mm to 4.5 mm) and the temperature of the electrolyte was increased (from 20 °C to 60 °C). Placing the anode against the diaphragm removed the resistance introduced by the electrolyte in the anode compartment, while the temperature increase offered better ionic conductivity and more favorable reaction conditions. Collectively, these reactor modifications achieved a notably low cell voltage of 2.89 V at industrially relevant current densities (-200 mA cm^{-2}). The favorable $|E_{\text{cell}}|$ could be maintained during electrolysis along with stable electrolyte composition and pH owing to the mixing setup, and although the liquid products can potentially reach the anode and oxidize to CO₂, directing the catalyst selectivity towards gas products can effectively address this issue.

Copper is unique as it can form multicarbon products alongside monocarbon ones. However, the limited selectivity towards a single product is considered a disadvantage. Through modification of the catalyst, it is possible to improve the selectivity and target specific products. Among various modification techniques, molecular surface modification is a promising strategy, despite the almost complete absence of investigations of this approach in acid

conditions. In the conclusive phase of the project, surface modification effects in acid were studied with 1-ethyl-3-methylimidazolium tetrafluoroborate (EMIMBF₄) and tetradecylphosphonic acid (TDPA). The deposition of an organic EMIMBF₄-derived layer was achieved via the one-electron reduction of the EMIM⁺ cation. Several characterization techniques (electron microscopy, XPS, ATR-FTIR) were used to elucidate the nature of the electrodeposited film, which retained the signatures of the imidazolium structure with no evidence of dimerization. The presence of the IL-layer favored the formation of C₂₊ products at all current densities tested (from -50 mA cm⁻² to -300 mA cm⁻²), while showing a stability in terms of selectivity and cathodic voltage over several hours, an indication of the robustness of the modification. In addition, the organic film resulted in a partial selectivity towards CO₂R even in an alkali-metal-free acidic electrolyte, which usually leads to complete selectivity towards HER. The TDPA evaluation reported here is limited to preliminary tests. In this case, the deposition on copper was achieved through a self-assembly method with different TDPA/catalyst ratios, thus modified nanoparticles with varying amount of TDPA were obtained. The effect on the selectivity was dependent on the current density and the ratio chosen. In almost all of the tests, despite an increase in H₂ formation, the modification enhanced the selectivity for C₂₊ products at the expenses of C₁ species, yielding remarkably high C₂₊/C₁ ratios.

5.2 Future perspectives

Much work is still needed to develop CO₂ electrolyzers that meet all the requirements to form cheap renewable carbon products. From the results gathered in this work, further advancements improving and building on the previously described setups can be envisaged to reach the goal of commercial CO₂ reduction.

Considering the recycling system shown in Chapter 2, the high cell voltage of the reactor can be lowered by employing more efficient BPMs, without sacrificing the long term electrolyte

stability that they provide. For example, catalyst-loaded BPMs decrease the potential of the water dissociation at the interlayer and could soon be ready for evaluation in long term CO₂R tests.^{161,162}

As for the results presented in Chapter 3, additional modifications can contribute to further reduce the cell voltage. A full MEA configuration could be adopted, meaning that the cathode would be also pressed against the cell separator, thus implementing a zero-gap configuration for the reactor which would eliminate the resistance introduced by the flowing catholyte.¹⁰² Alternatively, in membraneless configurations the compartment separator is removed, avoiding any associated voltage drop, and could maintain the separation of cathodic and anodic products through the use of a laminar electrolyte flow.²⁶⁸ The oxidation reaction at the anode can also be switched from OER to one with a lower energy requirement, such as glycerol oxidation²⁶⁹ and chloride oxidation (despite the health hazards of the latter).²⁷⁰ Regarding the cathode itself, catalysts with lower overpotentials for CO₂R could be employed, by changing either the morphology or the composition of the catalyst. In addition, choosing a catalyst selective for gas products (CO and C₂H₄)^{49,200,201} provides a straightforward solution to the problem of the liquid products oxidation at the anode. Finally, more uniform heating of the entire setup, achieved with an oven, would provide a stable and consistent temperature to all the reactor components.¹⁷⁰

Regarding the deposition of molecular species on the catalyst surface discussed in Chapter 4, several other molecules can be considered to suppress HER and/or direct the selectivity towards the target products. Electrodeposition can be applied to a wide range of molecules encompassing other ionic liquids,²⁴⁰ iodonium²⁷¹ and sulfonium²⁷² ions. On the other hand, depositions that do not involve prior reduction of the species could concern quaternary ammonium groups, like dodecyltrimethylammonium,²⁷³ cetyltrimethylammonium²⁷⁴, and similar positively charged molecules.

The findings outlined in this thesis positively contributed to advancements in the field of CO₂ electrochemical conversion by providing an array of strategies to improve the reactor performance. Through combination and development of the insights gathered on reactant utilization, cell voltage, and selectivity, CO₂ reduction is on the way to transition from a lab-scale reaction to a process converting gigatonnes of a harmful greenhouse gas into valuable feedstock.

Chapter 6

Experimental Procedures

6.1 Materials

All chemicals employed were of reagent grade or better. CH_3COOCu , CH_3COOK , CH_3COOH , KCl , H_2SO_4 , KHSO_4 , KOH , HCOOH , ethanol (96% v/v), 1-propanol, terephthalic acid, Cu nanopowder (40-60 nm size), Nafion 117 (5 wt% in lower aliphatic alcohols and water), and TDPA were purchased from Sigma Aldrich. Cs_2SO_4 was bought from Fisher. KH_2PO_4 and K_2HPO_4 were purchased from Roth. Methanol was ordered from Carlo Erba. D_2O was bought from Eurisotop. EMIMBF_4 was ordered from IoLiTec. Nickel foam was purchased from Goodfellow. IrO_x -coated carbon paper was bought from Dioxide Materials. Polytetrafluoroethylene (PTFE) membrane (0.45 μm pore size) was ordered from Sartorius. Nafion membrane (Nafion 115) was purchased from Sigma. Bipolar membrane (Fumasep) was bought from Fuel Cell Store. Zirfon diaphragm (UTP 220) was bought from Agfa.

Ultrapure Milli-Q H_2O was employed for preparations and washing.

6.2 Synthesis and preparations

Nanoparticle synthesis

Copper acetate (0.74 g) was dissolved in ethanol (80 mL, 96%) and sonicated for 2-3 h until complete dissolution.¹⁵¹ The blue solution was placed in the PTFE liner of an autoclave (125 mL, Parr Instrument Company) and then heated at 200 °C for 20 h in a Carbolite Gero CWF1213 furnace. After this time, a clear solution was obtained with the dark-brown CuO nanoparticles deposited at the bottom of the liner. The product was then washed twice with distilled water, three times with ethanol and dried under vacuum for 24 h before use (yield ~ 80%).

Electrode preparation

The gas diffusion electrodes (GDEs) were prepared using a methanolic ink containing the nanoparticles (Cu, CuO, or modified TDPA-modified CuO, 10 mg mL⁻¹) and Nafion 117 as a binder (1:1 ratio NPs(mg)/Nafion(μ L)). The suspension was sonicated for 1 h to allow good dispersion of the particles. The ink was then spray-coated onto a PTFE membrane confined to a circular diameter of 2 cm² to obtain a total mass loading of approximately 2.25 mg cm⁻² after drying under vacuum.

Phosphonic acid deposition

Different amounts of TDPA were dispersed in methanol by sonicating for 1 h, forming white turbid suspensions. Then, commercial Cu NPs were added to the suspensions and the resulting mixture was sonicated for 20 min at (42 \pm 1 °C). Afterwards, the modified nanoparticles were washed 5 times with methanol and then placed in a desiccator for at least 24 h before testing.

6.3 Physical characterization

Microscopy

Transmission electron microscopy (TEM) images were obtained using a Jeol 2100F microscope and a gold grid as the sample support.

Scanning electron microscopy (SEM) analysis was conducted using a SU-70 Hitachi FEG-SEM equipped with an X-Max 50 mm² Oxford spectrometer for energy dispersive X-Ray spectroscopy (EDX) measurements. Before the analysis the GDEs were washed with Milli-Q water, dried overnight in a desiccator. A carbon coating was applied to ensure conductivity before the analysis.

XRD

X-ray diffraction (XRD) data were obtained from a D8 ADVANCE diffractometer (Bruker) using a Cu K α X-ray source (1.5406Å). Peaks were attributed using the PDF-2/release 2013 RDB database.

XPS

X-Ray Photoelectron Spectroscopy (XPS) spectra were obtained using an Omicron Argus X-ray photoelectron spectrometer equipped with a monochromate AlK α radiation source ($h\nu = 1486.6$ eV) as well as a 280 W electron beam power. The diameter of analyzed area on the GDEs was 1 mm². The emission of photoelectrons from the GDEs was analyzed at a takeoff angle of 45° under ultra-high vacuum conditions ($\leq 10^{-9}$ mbar). Survey spectra were carried out with a 100 eV pass energy, while for the high-resolution N 1s spectra the pass energy was 20 eV. All binding energies were calibrated against the C 1s (C-C) binding energy at 284.8 eV and Scofield factors were used to correct the elements' peak intensities. The spectra were fitted using Casa XPS v.2.3.15 software (Casa Software Ltd, U.K.) and applying a Gaussian:Lorentzian ratio (G:L) equal to 70:30.

ATR-FTIR

Attenuated total reflection Fourier transform infrared spectroscopy (ATR-FTIR) measurements were obtained using a Bruker VERTEX 70 FTIR spectrometer equipped with a diamond ATR accessory (Quest™, Specac). The spectra were collected in the wavenumber range from 400 cm^{-1} to 4000 cm^{-1} , maintaining a spectral resolution of 4 cm^{-1} . Each spectrum was obtained from an aggregate of 100 scans to enhance the signal-to-noise ratio. After acquisition, the spectra were processed through a series of steps including baseline correction, atmospheric vapor compensation (water vapor and CO_2 signal subtraction) and a smoothing function for improved clarity and precision in spectral features.

WCA

Water contact angle (WCA) was measured using a Drop Shape Analyzer (DSA25) from KRÜSS. The measurements were performed at room temperature and ambient humidity on GDE samples. Each sample was measured at three different locations and the average value was reported.

6.4 Electrochemical procedures

All electrochemical experiments were conducted with a BioLogic VSP300 or VMP3 potentiostat with a 20 A current booster. Electrocatalysis was conducted in a custom-made gas-fed flow cell (Sphere Ltd.). A leak-free $\text{Ag}/\text{AgCl}/\text{KCl}_{3.4\text{M}}$ reference electrode (Innovative Instruments Ltd.) was used. The PTFE-based GDEs were electrically contacted using Cu tape and confined to a geometric area of 1 cm^2 . Electrical connection of the anode was provided by the conductive back plate in a two-gap configuration, while Cu tape was used for a one-gap setup. The required pre-activation of the GDEs involved consecutive LSVs under CO_2 flow with a sweep rate of 25 mV s^{-1} between -0.5 to -1.9 V vs. Ag/AgCl until stabilization of the current response. The voltage values given are not iR corrected, unless otherwise specified.

6.4.1 ECSA

The electrochemical surface area (ECSA) was measured through the capacitance of the GDEs in 0.05 M H₂SO₄ / 3 M KCl solution under a CO₂ flow rate of 10 mL min⁻¹. The capacitance was measured by analyzing the cyclic voltammograms of the cathodes at -0.495 V vs. Ag/AgCl using Equation 6.1:

$$C v = \frac{j_a - j_c}{2} \quad 6.1$$

where C is the capacitance (F), j_a is the anodic current density at -0.495 V vs. Ag/AgCl (A cm⁻²), j_c is the cathodic current density at -0.495 V vs. Ag/AgCl (A cm⁻²) and v is the scan rate (V s⁻¹). The value of the capacitance was found by plotting the right side of the equation against the scan rate. The ECSA was subsequently identified as the difference between the capacitance of the GDEs compared to a flat 1 cm² Cu surface.²¹⁶

6.5 Operational parameters

The CO₂ feed flow rate was varied between 20 and 0.4 mL min⁻¹ using a mass flow controller (Bronkhurst), and double checked with gas flow meters (MesaLabs Defender 530+ and Ellutia 7000). The flow meter data logging software (MesaLabs DryCalPro) was used to monitor real-time flow rates. Catholyte and anolyte were circulated using a peristaltic pump at a rate of 25 mL min⁻¹ for the results described in Chapter 2 and 4, while the rate was set to 60 mL min⁻¹ for the tests in Chapter 3. The Ar flow rate purging the electrolyte was set 35 mL min⁻¹ in all cases, except for the CO₂ recycling experiment (Chapter 2) when it was changed to 20 mL min⁻¹. The catholyte reservoir outlet (termed main reservoir outlet when a mixing configuration is employed) and the direct outlet were connected to a gas trap (together or separately) to carry the gas products to the gas chromatograph (GC) for quantification (Section 6.6.4). Additionally, calibrated flow meters (MesaLabs Defender 530+ and Ellutia 7000) were used to

verify flow rates before and after the GC inlet and outlet to ensure the correct flow value was recorded and to establish the portion of CO₂ utilized to account for mass balance. CO₂ consumption, crossover of liquid products and bubble formation in the catholyte have all been taken into account to assure the accuracy of product detection at all flow rates.²⁷⁵ The catholyte and anolyte volumes were 20 mL each for all experiments unless otherwise specified. When the electrolyte is externally mixed (Chapter 3) the total amount of solution was 30 mL. Gas products for controlled current electrolysis experiments were recorded at 20 min, while the liquid products were sampled after 30 min of electrolysis. For experiments longer than 30 min, liquid samples were extracted using a syringe every hour and the gas products were recorded every 20 min. The electrolyte temperature was increased by putting the main reservoir in a hot water bath, while the degassing reservoir is partially insulated with aluminum foil (Chapter 3). The remaining parts of the system (cell and tubes) have no mean of thermal insulation. The temperature of the electrolyte solution in the degassing reservoir is slightly lower than the one in the main reservoir, hence the values given above (40 and 60 °C) are a mean of these two temperatures.

6.5.1 IL deposition

The optimal IL deposition was performed by applying -10 mA cm^{-2} for 30 minutes to the Cu GDEs in a 0.5 M EMIMBF₄ aqueous solution under inert atmosphere and then allowing the electrode to reach open circuit potential. The electrodeposition can take place in a separate container or within the flow cell with an electrolyte flow rate of 9 mL min^{-1} by replacing the catholyte reservoir with one containing the EMIMBF₄ solution. In the first case, after deposition, the electrode is removed from the separate container, rinsed thoroughly with water, and placed in the flow cell to perform CO₂R experiments. In the second case, after deposition, water is flown for at least two minutes in the catholyte chamber to ensure that excess IL is evacuated before filling the chamber with the catholyte and running CO₂R tests.

6.6 Quantification

6.6.1 Product analysis

Gas products

Gas products were detected on-line using an SRI instruments 8610 GC with Ar as the carrier gas. The GC was fitted with a thermal conductivity detector for H₂ quantification, where the gas was separated using a HaySepD precolumn with a 3 m molecular sieve column. Carbon products were separated using a 5 m HaySepD column (CO, C₂H₄) and detected using a flame-ionization detector fitted with a methanizer. Calibration was performed using a custom standard gas mixture in CO₂.

The FE for gas products was calculated using Equation 6.2:

$$\text{FE (\%)} = \frac{n_{\text{product}} \times n_{\text{electrons}} \times F}{(Q_{t=0} - Q_{t=x})} \quad 6.2$$

Where n_{product} is the amount of product obtained (mol), $n_{\text{electrons}}$ is the number of electrons used to make the product, F is the Faraday constant (C mol⁻¹), $Q_{t=0}$ is the charge at the time of the injection, and $Q_{t=x}$ is the charge at time x seconds before the injection, representing the time taken to fill the sample loop, with x depending on the combined flow rate of Ar and CO₂ as well as the loop size (0.5 mL).

Liquid products

Liquid products were analyzed using ¹H NMR with a presaturation water suppression method on a Bruker Advance III 300 MHz spectrometer at 300 K. D₂O was used as the lock solvent and an aqueous solution of terephthalic acid was used as an internal standard for quantification. The FE for liquid products is also calculated with Equation 6.2.

6.6.2 Figures of merit

Single-Pass Conversion Calculation

The single-pass conversion to CO₂R products was calculated using Equation 6.3:

$$\text{SPC (\%)} = \sum \left\{ \left[\left(\frac{j_{\text{product}} \times 60 \text{ s}}{n_{\text{electrons}} \times F} \right) \div \left(\frac{\text{flow rate}}{24.05} \right) \right] \times \text{carbon atoms} \times 100 \right\} \quad 6.3$$

Where j_{product} is the partial current density for a particular product (mA cm⁻²), $n_{\text{electrons}}$ is the number of electrons needed for the reduction, F is the Faraday constant (C mol⁻¹), the flow rate is the one chosen for CO₂ (L min⁻¹), and 24.05 L equals to the molar volume of a gas at normal temperature and pressure. The total SPC is obtained by adding the single-pass conversion values for each carbon product.

Productivity Calculation

The productivity (P , mg of reduced CO₂ min⁻¹ cm⁻²) was calculated for each CO₂ feed flow rate value according to Equation 6.4:

$$P = \text{mm}_{\text{CO}_2} \times \frac{\text{CO}_{2 \text{ red}}}{t_{\text{GC}} \times A} \times 1000 \quad 6.4$$

Where mm_{CO_2} is the molar mass of CO₂ (g mol⁻¹), $\text{CO}_{2 \text{ red}}$ is the amount of reduced CO₂ (mol), t_{GC} is the time needed to fill the GC loop (min) with a specific CO₂ feed flow rate and A is the area of the electrode (cm²). The GC loop volume (0.5 mL) is the unit used to quantify the amounts of CO₂ and products.

Utilization calculation

The CO₂ utilization is defined as the percentage of CO₂ used for generation of products and was calculated using Equation 6.5. $\dot{n}_{\text{CO}_2 \text{ total}}$ is the sum of the molar flows of the feed CO₂ and r-CO₂ circulating in the system, and therefore represents the total amount of CO₂ available for

reaction. $\dot{n}_{\text{CO}_2\text{unused}}$ is the molar flow of CO_2 that does not go towards products and is vented from the system, which is then detected in the GC.

$$\text{utilization (\%)} = \frac{\dot{n}_{\text{CO}_2\text{total}} - \dot{n}_{\text{CO}_2\text{unused}}}{\dot{n}_{\text{CO}_2\text{total}}} \times 100 \quad 6.5$$

6.6.3 Electrolyte Analysis

The quantification of K^+ was performed with a Nexion 2000B inductively coupled plasma atomic mass spectrometer (Perkin-Elmer) using the Syngistix™ software.

6.6.4 Outlet Stream Analysis

The assessment of the gas output of the reactor was conducted through analysis of the gas stream composition of each outlet. Figure 6.1 shows a simplified version of the reactor setup valid for all the configurations tested. Only the gas outlet are shown, for a complete scheme of the setup refer to Sections 2.2.5 and 3.2.5. The gas streams can be analyzed together (up to two outlets at a time) or separately.

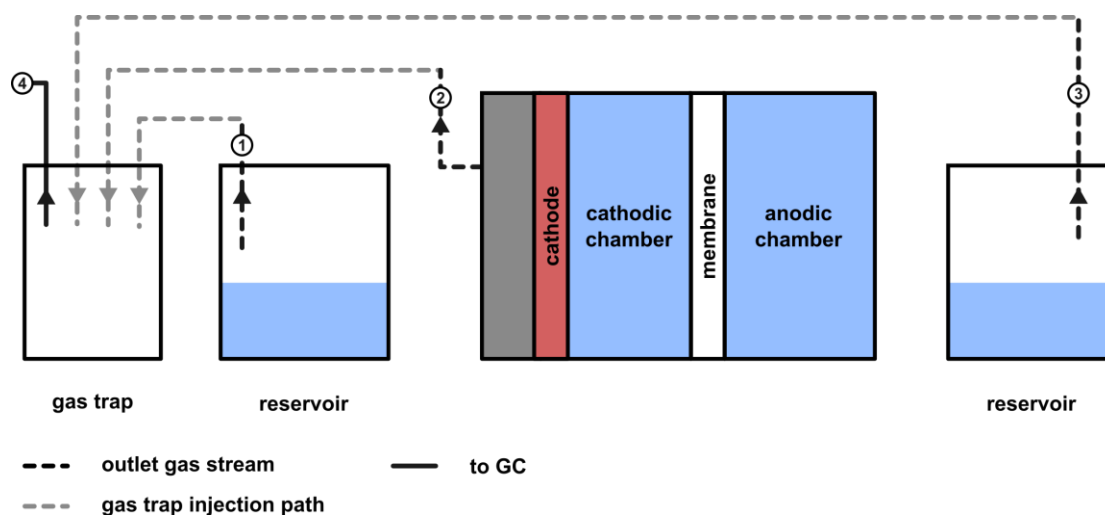


Figure 6.1 Illustration of the flow cell gas outlets (1, 2 and 3) and path to GC (4).

6.7 Physical model

A monodimensional (1D) 2-phase model of the porous catalyst in contact with the electrolyte was modelled at steady state and at isothermal conditions ($T = 298.15$ K). A schematic representation of the model with associated boundary conditions is shown in Figure 6.2. The length of the catalyst is set as experimentally determined ($6 \mu\text{m}$) and the diffuse layer thickness was set as $100 \mu\text{m}$ as in previous studies.^{276,277}

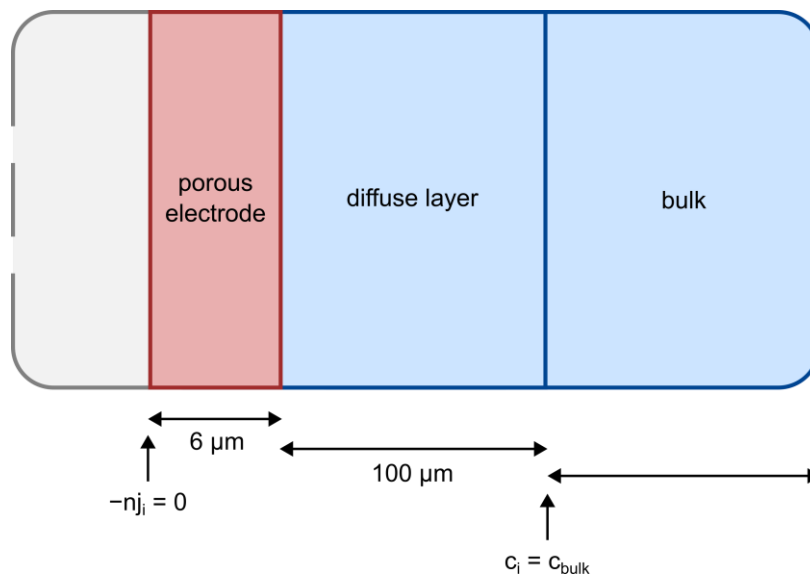


Figure 6.2 Illustration of the 1D model.

The bulk electrolyte is 3 M KCl and 0.05 M sulfuric acid ($\text{pH}=1$). The electrolyte contains 6 dissolved species: CO_2 , K^+ , H^+ , OH^- , HCO_3^- and CO_3^{2-} . To calculate the concentration of CO_2 dissolved in the bulk ($C^0_{\text{CO}_2,\text{aq}}$) the Henry's law was used assuming a fugacity equal to 1 bar (Equation 6.6):

$$C^0_{\text{CO}_2,\text{aq}} = K_H^0 p_{\text{CO}_2,\text{gas}} \quad 6.6$$

where the Henry's constant, in $\text{mol L}^{-1} \text{atm}^{-1}$ was calculated as follows (Equations 6.7 and 6.8):

$$\ln(K_H^0) = \frac{9345.17}{T} - 60.2409 + 23.3585 \ln\left(\frac{T}{100}\right) \quad 6.7$$

$$K_H^0 = 0.03 \quad 6.8$$

For CO₂ at 1 atm and 298.15 K the concentration of CO₂ in aqueous phase (C_{CO₂,aq}) amounts to 33.62 mol m⁻³. This concentration needs to be corrected, as a result of the high concentration of ions present in the electrolyte²⁷⁸ (Equations 6.9 and 6.10).

$$\log \left(\frac{C_{CO_2,aq}^0}{C_{CO_2,aq}} \right) = \sum (h_{ion} + h_G) C_i \quad 6.9$$

where

$$h_G = h_{G,0} + h_T (T - 298.15) \quad 6.10$$

The model parameters for concentration correction are reported in Table 6.1:²⁷⁸

Table 6.1 Parameters for the concentration correction.

Constant	value (m ³ kmol ⁻¹)
$h_{G_{CO_2},0}$	0.0172
$h_{T_{CO_2}}$	0.000338 (m ³ kmol ⁻¹ K)
h_{K^+}	0.0922
h_{Cl^-}	0.0318
h_{OH^-}	0.0839
h_{H^+}	0.0000
$h_{SO_4^{2-}}$	0.1117

In this case for a solution of 0.05 M H₂SO₄ and 3 M KCl, h_G and the corrected concentration of CO₂ in the electrolyte (C_{CO₂,aq}) amount to 0.017m³ kmol⁻¹ and 0.73 mol m⁻³, respectively. Different acid/base carbonate and water dissociation reactions occur in the electrolyte. None of the reactions were assumed to be in equilibrium and the kinetic expressions used to calculate the rate of reaction of the species i (r_i) are written as follows (Equation 6.11):

$$r_i = v_i (k_i^f \prod_j c_j^{v_j} - k_i^b \prod_j c_j^{v_j}) \quad 6.11$$

The following homogeneous reactions take place in the porous electrode domain, as well as in the diffuse layer domain:

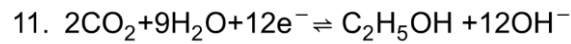
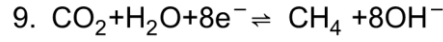
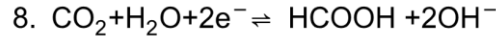
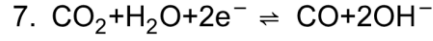
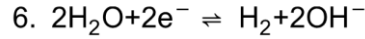
1. $\text{CO}_2 + \text{H}_2\text{O} \rightleftharpoons \text{H}^+ + \text{HCO}_3^-$
2. $\text{HCO}_3^- \rightleftharpoons \text{H}^+ + \text{CO}_3^{2-}$
3. $\text{CO}_2 + \text{OH}^- \rightleftharpoons \text{HCO}_3^-$
4. $\text{HCO}_3^- + \text{OH}^- \rightleftharpoons \text{CO}_3^{2-} + \text{H}_2\text{O}$
5. $\text{H}_2\text{O} \rightleftharpoons \text{H}^+ + \text{OH}^-$

The kinetic parameters used on the homogeneous reaction rates are reported in Table 6.2:¹³⁹

Table 6.2 Kinetic parameters for the homogeneous reaction rates.

Parameter	value	unit
k_1^f	3.71	s^{-1}
k_1^b	87.00	$\text{m}^3\text{mol}^{-1}\text{s}^{-1}$
k_2^f	9.98	s^{-1}
k_2^b	5.00×10^7	$\text{m}^3\text{mol}^{-1}\text{s}^{-1}$
k_3^f	2.23	$\text{m}^3\text{mol}^{-1}\text{s}^{-1}$
k_3^b	5.35×10^{-5}	s^{-1}
k_4^f	6.00×10^6	$\text{m}^3\text{mol}^{-1}\text{s}^{-1}$
k_4^b	3.00×10^5	s^{-1}
k_5^f	2.29×10^{-1}	$\text{mol m}^{-3}\text{s}^{-1}$
k_5^b	2.31×10^7	$\text{m}^3 \text{mol}^{-1} \text{s}^{-1}$

Concerning charge transfer reactions, they only occur in the porous electrode domain:



In this case, as a first approach, only the consumption of CO_2 and production of OH^- have been considered, since these are the only species that have a direct impact on the pH.¹³⁹ The reaction rates for these processes were calculated according to Equations 6.12 and 6.13:

$$R_{\text{CO}_2} = -\frac{i}{F} \left(\frac{F_{E_{\text{CO}}}}{2} + \frac{F_{E_{\text{HCOOH}}}}{2} + \frac{F_{E_{\text{CH}_4}}}{8} + \frac{F_{E_{\text{C}_2\text{H}_4}}}{6} + \frac{F_{E_{\text{C}_2\text{H}_5\text{OH}}}}{6} \right) \frac{\epsilon}{L_{\text{catalyst}}} \quad 6.12$$

$$R_{\text{OH}^-} = \frac{i}{F} \frac{\epsilon}{L_{\text{catalyst}}} \quad 6.13$$

where, i , ϵ , F , L_{catalyst} and F_{E_i} correspond to the current, porous fraction of the electrode, Faraday constant and faradaic efficiency of the species i , respectively. As a result, this model relies on the use of experimental information as input (faradaic efficiencies as function of the current).

6.7.1 Governing equations

A reaction-diffusion model was implemented to simulate the local pH changes using COMSOL Multiphysics 5.5 software. This model was solved at steady state, however its implementation on transient state requires minor modifications. In the case of the diffuse layer the mass balance for each species can be written as Equations 6.14 and 6.15:

$$\nabla \cdot J_i = r_i \quad 6.14$$

where

$$J_i = -D_i \nabla C_i \quad 6.15$$

The diffusion coefficients for the species i are shown in Table 6.3:¹³⁹

Table 6.3 Diffusion coefficients for the different species.

species	D_i (m^2s^{-1})
CO_2	1.910×10^{-9}
CO_3^{2-}	0.923×10^{-9}
HCO_3^-	1.185×10^{-9}
H^+	9.310×10^{-9}
OH^-	5.273×10^{-9}

The porous electrode domain was considered as an effective porous media with the following mass balance for each species. Here the porosity (ϵ) was set to 0.6 and the effective diffusion coefficients were corrected with the Bruggeman model according to the following equations:

$$\nabla \cdot J_i = R_i + r_i \quad 6.16$$

where

$$J_i = -D_{e_i} \nabla \epsilon C_i \quad 6.17$$

$$D_{e_i} = \frac{\epsilon}{T} D_i \quad 6.18$$

$$T = \epsilon^{-0.5} \quad 6.19$$

Bibliography

1. Lewis, N. S. & Nocera, D. G. Powering the planet: Chemical challenges in solar energy utilization. *Proc. Natl. Acad. Sci. U. S. A.* **103**, 15729–15735 (2006).
2. Ritchie, H., Roser, M. & Rosado, P. Energy. <https://ourworldindata.org/energy> (2022).
3. Fossil - Department of Energy. <https://www.energy.gov/fossil>.
4. *IPCC Fourth Assessment Report: Climate Change.* (2007).
5. Ritchie, H., Rosado, P. & Roser, M. Greenhouse gas emissions. <https://ourworldindata.org/greenhouse-gas-emissions> (2020).
6. Siegenthaler, U. *et al.* Stable carbon cycle-climate relationship during the late pleistocene. *Science (80-.)*. **310**, 1313–1317 (2005).
7. The Keeling Curve. <https://keelingcurve.ucsd.edu/>.
8. *I. P. on Climate Change, Climate Change 2021: The Physical Science Basis.* (2021).
9. Figueres, C. *et al.* Emissions are still rising: ramp up the cuts. *Nat.* **2021 5647734 564**, 27–30 (2018).
10. Climate Action Tracker - Temperatures. <https://climateactiontracker.org/>.
11. Ritchie, H., Rosado, P. & Roser, M. Emissions by sector. <https://ourworldindata.org/emissions-by-sector> (2020).
12. IEA. *Tracking Clean Energy Progress.* <https://www.iea.org/reports/tracking-clean-energy-progress-2023> (2023).
13. Nitopi, S. *et al.* Progress and Perspectives of Electrochemical CO₂ Reduction on Copper in Aqueous Electrolyte. *Chem. Rev.* **119**, 7610–7672 (2019).
14. Prado, A. & Mac Dowell, N. The cost of permanent carbon dioxide removal. *Joule* **7**, 700–712 (2023).
15. Keith, D. W., Holmes, G., St. Angelo, D. & Heidel, K. A Process for Capturing CO₂ from the Atmosphere. *Joule* **2**, 1573–1594 (2018).
16. *Dealing with carbon dioxide at scale | Royal Society.* [129](https://royalsociety.org/topics-</div><div data-bbox=)

- policy/publications/2018/dealing-with-carbon-dioxide-at-scale/ (2017).
17. Gutknecht, V., Snæbjörnsdóttir, S. Ó., Sigfússon, B., Aradóttir, E. S. & Charles, L. Creating a carbon dioxide removal solution by combining rapid mineralization of CO₂ with direct air capture. *Energy Procedia* **146**, 129–134 (2018).
 18. *The Global Status of CCS*. (2022).
 19. Burns, W. & Nicholson, S. Bioenergy and carbon capture with storage (BECCS): the prospects and challenges of an emerging climate policy response. *J. Environ. Stud. Sci.* **7**, 527–534 (2017).
 20. Grim, R. G. *et al.* Transforming the carbon economy: challenges and opportunities in the convergence of low-cost electricity and reductive CO₂ utilization. *Energy Environ. Sci.* **13**, 472–494 (2020).
 21. Dogutan, D. K. & Nocera, D. G. Artificial Photosynthesis at Efficiencies Greatly Exceeding That of Natural Photosynthesis. *Acc. Chem. Res.* 3143–3148 (2019) doi:10.1021/ACS.ACCOUNTS.9B00380/ASSET/IMAGES/MEDIUM/AR9B00380_0008.GIF.
 22. Seng Wong, T., Jajesniak, P. & Eldin Mohamed Omar Ali, H. Carbon Dioxide Capture and Utilization using Biological Systems: Opportunities and Challenges. *J Bioprocess Biotech.* **4**, 155 (2014).
 23. Li, K., An, X., Park, K. H., Khraisheh, M. & Tang, J. A critical review of CO₂ photoconversion: Catalysts and reactors. *Catal. Today* **224**, 3–12 (2014).
 24. Kumar, B. *et al.* Photochemical and Photoelectrochemical Reduction of CO₂. <https://doi.org/10.1146/annurev-physchem-032511-143759> **63**, 541–569 (2012).
 25. Zhang, Q., Bown, M., Pastor-Pérez, L., Duyar, M. S. & Reina, T. R. CO₂ Conversion via Reverse Water Gas Shift Reaction Using Fully Selective Mo-P Multicomponent Catalysts. *Ind. Eng. Chem. Res.* **61**, 12857–12865 (2022).
 26. Ahad, N. & de Klerk, A. Fischer–Tropsch acid water processing by Kolbe electrolysis. *Fuel* **211**, 415–419 (2018).
 27. Creissen, C. E. & Fontecave, M. Solar-Driven Electrochemical CO₂ Reduction with Heterogeneous Catalysts. *Adv. Energy Mater.* **11**, 2002652 (2021).
 28. Karapinar, D., Creissen, C. E., Rivera de la Cruz, J. G., Schreiber, M. W. & Fontecave, M. Electrochemical CO₂ Reduction to Ethanol with Copper-Based Catalysts. *ACS Energy Lett.* **6**, 694–706 (2021).
 29. Aresta, M., Dibenedetto, A. & Angelini, A. Catalysis for the valorization of exhaust carbon: From CO₂ to chemicals, materials, and fuels. technological use of CO₂. *Chemical Reviews* vol. 114 1709–1742 (2014).
 30. Hori Yoshio, Kikuchi Katsuhei & Suzuki Shin. Production of CO and CH₄ in Electrochemical Reduction of CO₂ at Metal Electrodes in Aqueous Hydrogencarbonate Solutions. *Chem. Lett.* **14**, 1695–1698 (1985).
 31. Jouny, M., Luc, W. & Jiao, F. General Techno-Economic Analysis of CO₂ Electrolysis Systems. *Ind. Eng. Chem. Res.* **57**, 2165–2177 (2018).

32. Gattrell, M., Gupta, N. & Co, A. Electrochemical reduction of CO₂ to hydrocarbons to store renewable electrical energy and upgrade biogas. *Energy Convers. Manag.* **48**, 1255–1265 (2007).
33. Eckert, M., Fleischmann, G., Jira, R., Bolt, H. M. & Golka, K. *Ullmann's Encyclopedia of Industrial Chemistry*. (Wiley-VCH Verlag, 2007).
34. Kniel, L., Stork, K. & Winter, O. *Ethylene - A Keystone to the Petrochemical Industry*. (Marcel Dekker, 1980).
35. Pimentel, D. & Patzek, T. W. Ethanol production using corn, switchgrass, and wood; Biodiesel production using soybean and sunflower. *Nat. Resour. Res.* **14**, 65–76 (2005).
36. Michel, H. The nonsense of biofuels. *Angewandte Chemie - International Edition* vol. 51 2516–2518 (2012).
37. Hori, Y. Electrochemical CO₂ Reduction on Metal Electrodes. in *Modern Aspects of Electrochemistry* 89–189 (Springer, 2008).
38. Zhang, X., Guo, S. X., Gandionco, K. A., Bond, A. M. & Zhang, J. Electrocatalytic carbon dioxide reduction: from fundamental principles to catalyst design. *Mater. Today Adv.* **7**, 100074 (2020).
39. Boutin, E. *et al.* Molecular catalysis of CO₂ reduction: recent advances and perspectives in electrochemical and light-driven processes with selected Fe, Ni and Co aza macrocyclic and polypyridine complexes. *Chem. Soc. Rev.* **49**, 5772–5809 (2020).
40. Zhang, S., Fan, Q., Xia, R. & Meyer, T. J. CO₂ Reduction: From Homogeneous to Heterogeneous Electrocatalysis. *Acc. Chem. Res.* **53**, 255–264 (2020).
41. Zhu, D. D., Liu, J. L. & Qiao, S. Z. Recent Advances in Inorganic Heterogeneous Electrocatalysts for Reduction of Carbon Dioxide. *Adv. Mater.* **28**, 3423–3452 (2016).
42. Zhang, L., Zhao, Z. J. & Gong, J. Nanostructured Materials for Heterogeneous Electrocatalytic CO₂ Reduction and their Related Reaction Mechanisms. *Angew. Chemie Int. Ed.* **56**, 11326–11353 (2017).
43. Lu, Q. & Jiao, F. Electrochemical CO₂ reduction: Electrocatalyst, reaction mechanism, and process engineering. *Nano Energy* **29**, 439–456 (2016).
44. Kuhl, K. P. *et al.* Electrocatalytic conversion of carbon dioxide to methane and methanol on transition metal surfaces. *J. Am. Chem. Soc.* **136**, 14107–14113 (2014).
45. Gao, D., Cai, F., Wang, G. & Bao, X. Nanostructured heterogeneous catalysts for electrochemical reduction of CO₂. *Curr. Opin. Green Sustain. Chem.* **3**, 39–44 (2017).
46. Ooka, H., Huang, J. & Exner, K. S. The Sabatier Principle in Electrocatalysis: Basics, Limitations, and Extensions. *Front. Energy Res.* **9**, 654460 (2021).
47. Hori, Y., Wakebe, H., Tsukamoto, T. & Koga, O. Electrocatalytic process of CO selectivity in electrochemical reduction of CO₂ at metal electrodes in aqueous media. *Electrochim. Acta* **39**, 1833–1839 (1994).
48. Hori, Y., Murata, A. & Takahashi, R. Formation of hydrocarbons in the electrochemical reduction of carbon dioxide at a copper electrode in aqueous solution. *J. Chem. Soc. Faraday Trans. 1 Phys. Chem. Condens. Phases* **85**, 2309–2326 (1989).

49. Bagger, A., Ju, W., Varela, A. S., Strasser, P. & Rossmeisl, J. Electrochemical CO₂ Reduction: A Classification Problem. *ChemPhysChem* **18**, 3266–3273 (2017).
50. Sa, Y. J. *et al.* Catalyst–electrolyte interface chemistry for electrochemical CO₂ reduction. *Chem. Soc. Rev.* **49**, 6632–6665 (2020).
51. Raab, S. J., Guschlbauer, R., Lodes, M. A. & Körner, C. Thermal and Electrical Conductivity of 99.9% Pure Copper Processed via Selective Electron Beam Melting. *Adv. Eng. Mater.* **18**, 1661–1666 (2016).
52. *The Future of Copper.* <https://commodityinsights.spglobal.com/futureofcopper.html> (2022).
53. De Gregorio, G. L. *et al.* Facet-Dependent Selectivity of Cu Catalysts in Electrochemical CO₂ Reduction at Commercially Viable Current Densities. *ACS Catal.* **10**, 4854–4862 (2020).
54. Jiang, K. *et al.* Metal ion cycling of Cu foil for selective C–C coupling in electrochemical CO₂ reduction. *Nat. Catal.* **2017 12 1**, 111–119 (2018).
55. Gu, Z. *et al.* Efficient Electrocatalytic CO₂ Reduction to C₂+ Alcohols at Defect-Site-Rich Cu Surface. *Joule* **5**, 429–440 (2021).
56. Arán-Ais, R. M., Scholten, F., Kunze, S., Rizo, R. & Roldan Cuenya, B. The role of in situ generated morphological motifs and Cu(i) species in C₂+ product selectivity during CO₂ pulsed electroreduction. *Nat. Energy* **2020 54 5**, 317–325 (2020).
57. Lee, S. Y. *et al.* Mixed Copper States in Anodized Cu Electrocatalyst for Stable and Selective Ethylene Production from CO₂ Reduction. *J. Am. Chem. Soc.* **140**, 8681–8689 (2018).
58. Chou, T. C. *et al.* Controlling the Oxidation State of the Cu Electrode and Reaction Intermediates for Electrochemical CO₂ Reduction to Ethylene. *J. Am. Chem. Soc.* **142**, 2857–2867 (2020).
59. De Luna, P. *et al.* Catalyst electro-redeposition controls morphology and oxidation state for selective carbon dioxide reduction. *Nat. Catal.* **2018 12 1**, 103–110 (2018).
60. Liang, Z. Q. *et al.* Copper-on-nitride enhances the stable electrosynthesis of multi-carbon products from CO₂. *Nat. Commun.* **2018 91 9**, 1–8 (2018).
61. Zhuang, T. T. *et al.* Steering post-C–C coupling selectivity enables high efficiency electroreduction of carbon dioxide to multi-carbon alcohols. *Nat. Catal.* **2018 16 1**, 421–428 (2018).
62. Chen, H. *et al.* Promotion of electrochemical CO₂ reduction to ethylene on phosphorus-doped copper nanocrystals with stable Cu^{δ+} sites. *Appl. Surf. Sci.* **544**, 148965 (2021).
63. Kas, R. *et al.* Manipulating the Hydrocarbon Selectivity of Copper Nanoparticles in CO₂ Electroreduction by Process Conditions. *ChemElectroChem* **2**, 354–358 (2015).
64. Ma, M., Djanashvili, K. & Smith, W. A. Controllable Hydrocarbon Formation from the Electrochemical Reduction of CO₂ over Cu Nanowire Arrays. *Angew. Chemie Int. Ed.* **55**, 6680–6684 (2016).
65. Schouten, K. J. P., Pérez Gallent, E. & Koper, M. T. M. The influence of pH on the

- reduction of CO and CO₂ to hydrocarbons on copper electrodes. *J. Electroanal. Chem.* **716**, 53–57 (2014).
66. Kuhl, K. P., Cave, E. R., Abram, D. N. & Jaramillo, T. F. New insights into the electrochemical reduction of carbon dioxide on metallic copper surfaces. *Energy Environ. Sci.* **5**, 7050–7059 (2012).
 67. Bui, J. C. *et al.* Engineering Catalyst-Electrolyte Microenvironments to Optimize the Activity and Selectivity for the Electrochemical Reduction of CO₂ on Cu and Ag. *Acc. Chem. Res.* **55**, 484–494 (2022).
 68. Todorova, T. K., Schreiber, M. W. & Fontecave, M. Mechanistic Understanding of CO₂ Reduction Reaction (CO₂RR) Toward Multicarbon Products by Heterogeneous Copper-Based Catalysts. *ACS Catal.* **10**, 1754–1768 (2020).
 69. Chernyshova, I. V., Somasundaran, P. & Ponnurangam, S. On the origin of the elusive first intermediate of CO₂ electroreduction. *Proc. Natl. Acad. Sci. U. S. A.* **115**, E9261–E9270 (2018).
 70. Wang, L., Gupta, K., Goodall, J. B. M., Darr, J. A. & Holt, K. B. In situ spectroscopic monitoring of CO₂ reduction at copper oxide electrode. *Faraday Discuss.* **197**, 517–532 (2017).
 71. Feaster, J. T. *et al.* Understanding Selectivity for the Electrochemical Reduction of Carbon Dioxide to Formic Acid and Carbon Monoxide on Metal Electrodes. *ACS Catal.* **7**, 4822–4827 (2017).
 72. Wuttig, A. *et al.* Tracking a common surface-bound intermediate during CO₂-to-fuels catalysis. *ACS Cent. Sci.* **2**, 522–528 (2016).
 73. DeWulf, D. W., Jin, T. & Bard, A. J. Electrochemical and Surface Studies of Carbon Dioxide Reduction to Methane and Ethylene at Copper Electrodes in Aqueous Solutions. *J. Electrochem. Soc.* **136**, 1686–1691 (1989).
 74. Figueiredo, M. C., Ledezma-Yanez, I. & Koper, M. T. M. In Situ Spectroscopic Study of CO₂ Electroreduction at Copper Electrodes in Acetonitrile. *ACS Catal.* **6**, 2382–2392 (2016).
 75. Jiang, S., Klingan, K., Pasquini, C. & Dau, H. New aspects of operando Raman spectroscopy applied to electrochemical CO₂ reduction on Cu foams. *J. Chem. Phys.* **150**, (2019).
 76. Huang, Y., Handoko, A. D., Hirunsit, P. & Yeo, B. S. Electrochemical Reduction of CO₂ Using Copper Single-Crystal Surfaces: Effects of CO* Coverage on the Selective Formation of Ethylene. *ACS Catal.* **7**, 1749–1756 (2017).
 77. Xiao, H., Cheng, T. & William A. Goddard, I. Atomistic Mechanisms Underlying Selectivities in C₁ and C₂ Products from Electrochemical Reduction of CO on Cu(111). *J. Am. Chem. Soc.* **139**, 130–136 (2016).
 78. Calle-Vallejo, F. & Koper, M. T. M. Theoretical Considerations on the Electroreduction of CO to C₂ Species on Cu(100) Electrodes. *Angew. Chemie Int. Ed.* **52**, 7282–7285 (2013).
 79. Montoya, J. H., Shi, C., Chan, K. & Nørskov, J. K. Theoretical insights into a CO dimerization mechanism in CO₂ electroreduction. *J. Phys. Chem. Lett.* **6**, 2032–2037

- (2015).
80. Goodpaster, J. D., Bell, A. T. & Head-Gordon, M. Identification of Possible Pathways for C-C Bond Formation during Electrochemical Reduction of CO₂: New Theoretical Insights from an Improved Electrochemical Model. *J. Phys. Chem. Lett.* **7**, 1471–1477 (2016).
 81. Garza, A. J., Bell, A. T. & Head-Gordon, M. Mechanism of CO₂ Reduction at Copper Surfaces: Pathways to C₂ Products. *ACS Catal.* **8**, 1490–1499 (2018).
 82. Luo, W., Nie, X., Janik, M. J. & Asthagiri, A. Facet Dependence of CO₂ Reduction Paths on Cu Electrodes. *ACS Catal.* **6**, 219–229 (2016).
 83. Ooka, H., Figueiredo, M. C. & Koper, M. T. M. Competition between Hydrogen Evolution and Carbon Dioxide Reduction on Copper Electrodes in Mildly Acidic Media. *Langmuir* **33**, 9307–9313 (2017).
 84. Dau, H. *et al.* The Mechanism of Water Oxidation: From Electrolysis via Homogeneous to Biological Catalysis. *ChemCatChem* **2**, 724–761 (2010).
 85. Liang, S., Altaf, N., Huang, L., Gao, Y. & Wang, Q. Electrolytic cell design for electrochemical CO₂ reduction. *J. CO₂ Util.* **35**, 90–105 (2020).
 86. Costentin, C., Robert, M. & Savéant, J. M. Catalysis of the electrochemical reduction of carbon dioxide. *Chem. Soc. Rev.* **42**, 2423–2436 (2013).
 87. Lum, Y., Yue, B., Lobaccaro, P., Bell, A. T. & Ager, J. W. Optimizing C-C Coupling on Oxide-Derived Copper Catalysts for Electrochemical CO₂ Reduction. *J. Phys. Chem. C* **121**, 14191–14203 (2017).
 88. Ren, D. *et al.* Selective Electrochemical Reduction of Carbon Dioxide to Ethylene and Ethanol on Copper(I) oxide catalysts. *ACS Catal.* **5**, 2814–2821 (2015).
 89. Zhao, C. & Wang, J. Electrochemical reduction of CO₂ to formate in aqueous solution using electro-deposited Sn catalysts. *Chem. Eng. J.* **293**, 161–170 (2016).
 90. Weekes, D. M., Salvatore, D. A., Reyes, A., Huang, A. & Berlinguette, C. P. Electrolytic CO₂ Reduction in a Flow Cell. *Acc. Chem. Res.* **51**, 910–918 (2018).
 91. Bevilacqua, M. *et al.* Energy Savings in the Conversion of CO₂ to Fuels using an Electrolytic Device. *Energy Technol.* **2**, 522–525 (2014).
 92. Salvatore, D. A. *et al.* Electrolysis of Gaseous CO₂ to CO in a Flow Cell with a Bipolar Membrane. *ACS Energy Lett.* **3**, 149–154 (2018).
 93. Merino-Garcia, I., Alvarez-Guerra, E., Albo, J. & Irabien, A. Electrochemical membrane reactors for the utilisation of carbon dioxide. *Chem. Eng. J.* **305**, 104–120 (2016).
 94. Burdyny, T. & Smith, W. A. CO₂ reduction on gas-diffusion electrodes and why catalytic performance must be assessed at commercially-relevant conditions. *Energy Environ. Sci.* **12**, 1442–1453 (2019).
 95. Rabiee, H. *et al.* Gas diffusion electrodes (GDEs) for electrochemical reduction of carbon dioxide, carbon monoxide, and dinitrogen to value-added products: a review. *Energy Environ. Sci.* **14**, 1959–2008 (2021).

96. Löwe, A. *et al.* Influence of Temperature on the Performance of Gas Diffusion Electrodes in the CO₂ Reduction Reaction. *ChemElectroChem* **6**, 4497–4506 (2019).
97. Jhong, H. R. Q., Brushett, F. R. & Kenis, P. J. A. The Effects of Catalyst Layer Deposition Methodology on Electrode Performance. *Adv. Energy Mater.* **3**, 589–599 (2013).
98. Saha, M. S., Gullá, A. F., Allen, R. J. & Mukerjee, S. High performance polymer electrolyte fuel cells with ultra-low Pt loading electrodes prepared by dual ion-beam assisted deposition. *Electrochim. Acta* **51**, 4680–4692 (2006).
99. Sievers, G. *et al.* Ultra-low loading Pt-sputtered gas diffusion electrodes for oxygen reduction reaction. *J. Appl. Electrochem.* **48**, 221–232 (2018).
100. An, X. *et al.* Electrodeposition of Tin-Based Electrocatalysts with Different Surface Tin Species Distributions for Electrochemical Reduction of CO₂ to HCOOH. *ACS Sustain. Chem. Eng.* **7**, 9360–9368 (2019).
101. Weng, L. C., Bell, A. T. & Weber, A. Z. Towards membrane-electrode assembly systems for CO₂ reduction: a modeling study. *Energy Environ. Sci.* **12**, 1950–1968 (2019).
102. Ge, L. *et al.* Electrochemical CO₂ reduction in membrane-electrode assemblies. *Chem* **8**, 663–692 (2022).
103. Habibzadeh, F. *et al.* Ion Exchange Membranes in Electrochemical CO₂ Reduction Processes. *Electrochemical Energy Reviews* vol. 6 1–35 (2023).
104. Bard, A. J. & Faulkner, L. R. *Electrochemical methods: fundamentals and applications*. (Wiley, 2001).
105. Dunwell, M., Yan, Y. & Xu, B. Understanding the influence of the electrochemical double-layer on heterogeneous electrochemical reactions. *Curr. Opin. Chem. Eng.* **20**, 151–158 (2018).
106. Bard, A. J. Inner-sphere heterogeneous electrode reactions. Electrocatalysis and photocatalysis: The challenge. *J. Am. Chem. Soc.* **132**, 7559–7567 (2010).
107. Kas, R., Kortlever, R., Yilmaz, H., Koper, M. T. M. & Mul, G. Manipulating the Hydrocarbon Selectivity of Copper Nanoparticles in CO₂ Electroreduction by Process Conditions. *ChemElectroChem* **2**, 354–358 (2015).
108. Pang, Y. *et al.* Joint tuning of nanostructured Cu-oxide morphology and local electrolyte programs high-rate CO₂ reduction to C₂H₄. *Green Chem.* **19**, 4023–4030 (2017).
109. Auinger, M. *et al.* Near-surface ion distribution and buffer effects during electrochemical reactions. *Phys. Chem. Chem. Phys.* **13**, 16384–16394 (2011).
110. Gupta, N., Gattrell, M. & MacDougall, B. Calculation for the cathode surface concentrations in the electrochemical reduction of CO₂ in KHCO₃ solutions. *J. Appl. Electrochem.* **36**, 161–172 (2006).
111. Ghobadi, M. H., Firuzi, M. & Asghari-Kaljahi, E. Relationships between geological formations and groundwater chemistry and their effects on the concrete lining of tunnels (case study: Tabriz metro line 2). *Environ. Earth Sci.* **75**, 1–14 (2016).
112. Akhade, S. A., McCrum, I. T. & Janik, M. J. The Impact of Specifically Adsorbed Ions

- on the Copper-Catalyzed Electroreduction of CO₂. *J. Electrochem. Soc.* **163**, F477–F484 (2016).
113. Chen, L. D., Urushihara, M., Chan, K. & Nørskov, J. K. Electric Field Effects in Electrochemical CO₂ Reduction. *ACS Catal.* **6**, 7133–7139 (2016).
114. Resasco, J. *et al.* Promoter Effects of Alkali Metal Cations on the Electrochemical Reduction of Carbon Dioxide. *J. Am. Chem. Soc.* **139**, 11277–11287 (2017).
115. Lamaison, S. *et al.* Designing a Zn–Ag Catalyst Matrix and Electrolyzer System for CO₂ Conversion to CO and Beyond. *Adv. Mater.* **34**, 2103963 (2022).
116. Gabardo, C. M. *et al.* Combined high alkalinity and pressurization enable efficient CO₂ electroreduction to CO. *Energy Environ. Sci.* **11**, 2531–2539 (2018).
117. Welch, A. J., Dunn, E., Duchene, J. S. & Atwater, H. A. Bicarbonate or Carbonate Processes for Coupling Carbon Dioxide Capture and Electrochemical Conversion. *ACS Energy Lett.* **5**, 940–945 (2020).
118. Dioxide Materials: Electrolyzer to convert carbon dioxide to carbon monoxide. <https://dioxidematerials.com/%0Atechnology/co2-electrolysis/>.
119. Dioxide Materials: Electrolyzer to transform carbon dioxide into formic acid. <https://dioxidematerials.com/%0Atechnology/formic-acid/>.
120. Haas, T., Krause, R., Weber, R., Demler, M. & Schmid, G. Technical photosynthesis involving CO₂ electrolysis and fermentation. *Nat. Catal.* **2017 11 1**, 32–39 (2018).
121. Masel, R. I. *et al.* An industrial perspective on catalysts for low-temperature CO₂ electrolysis. *Nat. Nanotechnol.* **2021 162 16**, 118–128 (2021).
122. Perazio, A., Creissen, C. E., Rivera de la Cruz, J. G., Schreiber, M. W. & Fontecave, M. Acidic Electroreduction of CO₂ to Multi-Carbon Products with CO₂ Recovery and Recycling from Carbonate. *ACS Energy Lett.* **8**, 2979–2985 (2023).
123. Wang, Q., Dong, H., Yu, H. & Yu, H. Enhanced performance of gas diffusion electrode for electrochemical reduction of carbon dioxide to formate by adding polytetrafluoroethylene into catalyst layer. *J. Power Sources* **279**, 1–5 (2015).
124. Karapinar, D., Creissen, C. E., Rivera De La Cruz, J. G., Schreiber, M. W. & Fontecave, M. Electrochemical CO₂ Reduction to Ethanol with Copper-Based Catalysts. *ACS Energy Letters* vol. 6 694–706 (2021).
125. García de Arquer, F. P. *et al.* CO₂ electrolysis to multicarbon products at activities greater than 1 A cm⁻². *Science* **367**, 661–666 (2020).
126. Creissen, C. E. *et al.* Molecular Inhibition for Selective CO₂ Conversion. *Angew. Chem. Int. Ed.* **61**, e202206279 (2022).
127. Lv, J.-J. *et al.* A Highly Porous Copper Electrocatalyst for Carbon Dioxide Reduction. *Adv. Mater.* **30**, 1803111 (2018).
128. Wang, R. *et al.* Maximizing Ag Utilization in High-Rate CO₂ Electrochemical Reduction with a Coordination Polymer-Mediated Gas Diffusion Electrode. *ACS Energy Lett.* **4**, 2024–2031 (2019).

129. Ma, S. *et al.* One-step electrosynthesis of ethylene and ethanol from CO₂ in an alkaline electrolyzer. *J. Power Sources* **301**, 219–228 (2016).
130. Dinh, C. T. *et al.* CO₂ electroreduction to ethylene via hydroxide-mediated copper catalysis at an abrupt interface. *Science* (80-.). **360**, 783–787 (2018).
131. Rabinowitz, J. A. & Kanan, M. W. The future of low-temperature carbon dioxide electrolysis depends on solving one basic problem. *Nat. Commun.* **11**, 5231 (2020).
132. Ma, M. *et al.* Insights into the carbon balance for CO₂ electroreduction on Cu using gas diffusion electrode reactor designs. *Energy Environ. Sci.* **13**, 977–985 (2020).
133. Ozden, A. *et al.* Cascade CO₂ electroreduction enables efficient carbonate-free production of ethylene. *Joule* **5**, 706–719 (2021).
134. Huang, J. E. *et al.* CO₂ electrolysis to multicarbon products in strong acid. *Science* **372**, 1074–1078 (2021).
135. Xie, Y. *et al.* High carbon utilization in CO₂ reduction to multi-carbon products in acidic media. *Nat. Catal.* **5**, 564–570 (2022).
136. Gu, J. *et al.* Modulating electric field distribution by alkali cations for CO₂ electroreduction in strongly acidic medium. *Nat. Catal.* **5**, 268–276 (2022).
137. Dean, J. A. *Lange's Handbook of Chemistry*. (McGraw-Hill, 1972).
138. Yang, K., Kas, R. & Smith, W. A. In Situ Infrared Spectroscopy Reveals Persistent Alkalinity near Electrode Surfaces during CO₂ Electroreduction. *J. Am. Chem. Soc.* **141**, 2022 (2019).
139. Huang, J. E. *et al.* CO₂ electrolysis to multicarbon products in strong acid. *Science* (80-.). **372**, 1074–1078 (2021).
140. Gu, J. *et al.* *Modulating Electric Field Distribution by Alkali Cations for CO₂ Electroreduction in Strongly Acidic Medium*. <https://chemrxiv.org/engage/chemrxiv/article-details/60e7fb33b9b601c39622b4c4> (2021) doi:10.33774/CHEMRXIV-2021-ZGQ9K.
141. Thorson, M. R., Siil, K. I. & Kenis, P. J. A. Effect of Cations on the Electrochemical Conversion of CO₂ to CO. *J. Electrochem. Soc.* **160**, F69–F74 (2013).
142. Ehlers, J. C., Feidenhans'l, A. A., Kasper, #, Therkildsen, T. & Larrazábal, G. O. Affordable Green Hydrogen from Alkaline Water Electrolysis: Key Research Needs from an Industrial Perspective. *ACS Energy Lett.* 1502–1509 (2023) doi:10.1021/ACSENERGYLETT.2C02897.
143. Pärnamäe, R. *et al.* Bipolar membranes: A review on principles, latest developments, and applications. *J. Memb. Sci.* **617**, 118538 (2021).
144. Xie, K. *et al.* Bipolar membrane electrolyzers enable high single-pass CO₂ electroreduction to multicarbon products. *Nat. Commun.* **13**, 3609 (2022).
145. Ma, M., Kim, S., Chorkendorff, I. & Seger, B. Role of ion-selective membranes in the carbon balance for CO₂ electroreduction via gas diffusion electrode reactor designs. *Chem. Sci.* **11**, 8854–8861 (2020).

146. Yan, Z., Hitt, J. L., Zeng, Z., Hickner, M. A. & Mallouk, T. E. Improving the efficiency of CO₂ electrolysis by using a bipolar membrane with a weak-acid cation exchange layer. *Nat. Chem.* **13**, 33–40 (2021).
147. Yang, K. *et al.* Cation-driven increases of CO₂ utilization in a bipolar membrane electrode assembly for CO₂ electrolysis. *ACS Energy Lett.* **6**, 4291–4298 (2021).
148. Siritanaratkul, B. *et al.* Zero-Gap Bipolar Membrane Electrolyzer for Carbon Dioxide Reduction Using Acid-Tolerant Molecular Electrocatalysts. *J. Am. Chem. Soc.* **144**, 7551–7556 (2022).
149. Vass, Á. *et al.* Local Chemical Environment Governs Anode Processes in CO₂ Electrolyzers. *ACS Energy Lett.* **6**, 3801–3808 (2021).
150. Peugeot, A., Creissen, C. E., Schreiber, M. W. & Fontecave, M. Advancing the Anode Compartment for Energy Efficient CO₂ Reduction at Neutral pH. *ChemElectroChem* **8**, 2726–2736 (2021).
151. Hong, Z. shan, Cao, Y. & Deng, J. fa. A convenient alcohothermal approach for low temperature synthesis of CuO nanoparticles. *Mater. Lett.* **52**, 34–38 (2002).
152. Hashiba, H. *et al.* Effects of electrolyte buffer capacity on surface reactant species and the reaction rate of CO₂ in Electrochemical CO₂ reduction. *J. Phys. Chem. C* **122**, 3719–3726 (2018).
153. Grunder, Y., Beane, J., Kolodziej, A., Lucas, C. A. & Rodriguez, P. Potential Dependent Structure and Stability of Cu(111) in Neutral Phosphate Electrolyte. *Surfaces 2019, Vol. 2, Pages 145-158* **2**, 145–158 (2019).
154. Monteiro, M. C. O. *et al.* Absence of CO₂ electroreduction on copper, gold and silver electrodes without metal cations in solution. *Nat. Catal.* **4**, 654–662 (2021).
155. Monteiro, M. C. O., Philips, M. F., Schouten, K. J. P. & Koper, M. T. M. Efficiency and selectivity of CO₂ reduction to CO on gold gas diffusion electrodes in acidic media. *Nat. Commun.* **12**, 1–7 (2021).
156. Hawks, S. A. *et al.* Analyzing Production Rate and Carbon Utilization Trade-offs in CO₂RR Electrolyzers. *ACS Energy Lett.* **7**, 2685–2693 (2022).
157. O'Brien, C. P. *et al.* Single Pass CO₂ Conversion Exceeding 85% in the Electrosynthesis of Multicarbon Products via Local CO₂ Regeneration. *ACS Energy Lett.* **6**, 2952–2959 (2021).
158. Gabardo, C. M. *et al.* Continuous Carbon Dioxide Electroreduction to Concentrated Multi-carbon Products Using a Membrane Electrode Assembly. *Joule* **3**, 2777–2791 (2019).
159. Strathmann, H., Rapp, H. J., Bauer, B. & Bell, C. M. Theoretical and practical aspects of preparing bipolar membranes. *Desalination* **90**, 303–323 (1993).
160. Delacourt, C., Ridgway, P. L., Kerr, J. B. & Newman, J. Design of an Electrochemical Cell Making Syngas (CO + H₂) from CO₂ and H₂O Reduction at Room Temperature. *J. Electrochem. Soc.* **155**, B42 (2007).
161. Chen, L., Xu, Q., Oener, S. Z., Fabrizio, K. & Boettcher, S. W. Design principles for water dissociation catalysts in high-performance bipolar membranes. *Nat. Commun.*

- 2022 131 **13**, 1–10 (2022).
162. Oener, S. Z., Foster, M. J. & Boettcher, S. W. Accelerating water dissociation in bipolar membranes and for electrocatalysis. *Science* **369**, 1099–1103 (2020).
 163. Alerte, T. *et al.* Downstream of the CO₂ Electrolyzer: Assessing the Energy Intensity of Product Separation. *ACS Energy Lett.* **6**, 4405–4412 (2021).
 164. Bhargava, S. S. *et al.* Decreasing the Energy Consumption of the CO₂ Electrolysis Process Using a Magnetic Field. *ACS Energy Lett.* **6**, 2427–2433 (2021).
 165. Esposito, D. V. Membraneless Electrolyzers for Low-Cost Hydrogen Production in a Renewable Energy Future. *Joule* **1**, 651–658 (2017).
 166. Hori, Y. Electrochemical CO₂ Reduction on Metal Electrodes. in *Modern Aspects of Electrochemistry* 89–189 (Springer New York, 2008). doi:10.1007/978-0-387-49489-0_3.
 167. Jeon, H. S. *et al.* Selectivity Control of Cu Nanocrystals in a Gas-Fed Flow Cell through CO₂ Pulsed Electroreduction. *J. Am. Chem. Soc.* **143**, 7578–7587 (2021).
 168. Vennekötter, J. B., Scheuermann, T., Sengpiel, R. & Wessling, M. The electrolyte matters: Stable systems for high rate electrochemical CO₂ reduction. *J. CO₂ Util.* **32**, 202–213 (2019).
 169. Salvatore, D. & Berlinguette, C. P. Voltage Matters When Reducing CO₂ in an Electrochemical Flow Cell. *ACS Energy Lett.* **5**, 215–220 (2020).
 170. Hoof, L. *et al.* Hidden parameters for electrochemical carbon dioxide reduction in zero-gap electrolyzers. *Cell Reports Phys. Sci.* **3**, 100825 (2022).
 171. Zhang, Z. *et al.* Conversion of Reactive Carbon Solutions into CO at Low Voltage and High Carbon Efficiency. *ACS Cent. Sci.* **8**, 749–755 (2022).
 172. Zheng, W. iR Compensation for Electrocatalysis Studies: Considerations and Recommendations. *ACS Energy Lett.* **8**, 1952–1958 (2023).
 173. Mauritz, K. A. & Moore, R. B. State of understanding of Nafion. *Chem. Rev.* **104**, 4535–4585 (2004).
 174. Vetter, K. M. *et al.* K⁺ Transport in Perfluorosulfonic Acid Membranes and Its Influence on Membrane Resistance in CO₂ Electrolysis. *ChemElectroChem* **9**, e202101165 (2022).
 175. El-Nagar, G. A., Haun, F., Gupta, S., Stojkovic, S. & Mayer, M. T. Unintended cation crossover influences CO₂ reduction selectivity in Cu-based zero-gap electrolyzers. *Nat. Commun.* 2023 141 **14**, 1–10 (2023).
 176. Büchi, F. N. & Scherer, G. G. In-situ resistance measurements of Nafion® 117 membranes in polymer electrolyte fuel cells. *J. Electroanal. Chem.* **404**, 37–43 (1996).
 177. Vermeiren, P., Adriansens, W., Moreels, J. P. & Leysen, R. Evaluation of the Zirfon® separator for use in alkaline water electrolysis and Ni-H₂ batteries. *Int. J. Hydrogen Energy* **23**, 321–324 (1998).
 178. Schalenbach, M., Lueke, W. & Stolten, D. Hydrogen Diffusivity and Electrolyte

- Permeability of the Zirfon PERL Separator for Alkaline Water Electrolysis. *J. Electrochem. Soc.* **163**, F1480–F1488 (2016).
179. Lavorante, M. J., Reynoso, C. Y. & Franco, J. I. Water electrolysis with Zirfon® as separator and NaOH as electrolyte. *New pub Balaban* **56**, 3647–3653 (2014).
180. Vermeiren, P., Moreels, J. P. & Leysen, R. Porosity in composite Zirfon® membranes. *J. Porous Mater.* **3**, 33–40 (1996).
181. de Groot, M. T. & Vreman, A. W. Ohmic resistance in zero gap alkaline electrolysis with a Zirfon diaphragm. *Electrochim. Acta* **369**, 137684 (2021).
182. Zhong, C. *et al.* A review of electrolyte materials and compositions for electrochemical supercapacitors. *Chem. Soc. Rev.* **44**, 7484–7539 (2015).
183. Abba, P., Gongwala, J., Laminsi, S. & Brisset, J. L. The Effect of the Humid Air Plasma on the Conductivity of Distilled Water: Contribution of Ions. *Int. J. Res. Chem. Environ.* **4**, 25–30 (2014).
184. Reinisch, D. *et al.* Various CO₂-to-CO Electrolyzer Cell and Operation Mode Designs to avoid CO₂-Crossover from Cathode to Anode. *Zeitschrift fur Phys. Chemie* **234**, 1115–1131 (2020).
185. Krause, R. *et al.* Industrial Application Aspects of the Electrochemical Reduction of CO₂ to CO in Aqueous Electrolyte. *Chemie Ing. Tech.* **92**, 53–61 (2020).
186. Küngas, R. Review—Electrochemical CO₂ Reduction for CO Production: Comparison of Low- and High-Temperature Electrolysis Technologies. *J. Electrochem. Soc.* **167**, 044508 (2020).
187. Dufek, E. J., Lister, T. E. & Mcllwain, M. E. Bench-scale electrochemical system for generation of CO and syn-gas. *J. Appl. Electrochem.* **41**, 623–631 (2011).
188. Kumar, B. *et al.* Reduced SnO₂ Porous Nanowires with a High Density of Grain Boundaries as Catalysts for Efficient Electrochemical CO₂-into-HCOOH Conversion. *Angew. Chemie - Int. Ed.* **56**, 3645–3649 (2017).
189. Dufek, E. J., Lister, T. E., Stone, S. G. & Mcllwain, M. E. Operation of a Pressurized System for Continuous Reduction of CO₂. *J. Electrochem. Soc.* **159**, F514–F517 (2012).
190. Kim, H. Y. *et al.* Analysis on the effect of operating conditions on electrochemical conversion of carbon dioxide to formic acid. *Int. J. Hydrogen Energy* **39**, 16506–16512 (2014).
191. Mizuno, T. *et al.* Effect of Temperature on Electrochemical Reduction of High-Pressure CO₂ with In, Sn, and Pb Electrodes. <http://dx.doi.org/10.1080/00908319508946098> **17**, 503–508 (2010).
192. Kriescher, S. M. A., Kugler, K., Hosseiny, S. S., Gendel, Y. & Wessling, M. A membrane electrode assembly for the electrochemical synthesis of hydrocarbons from CO₂(g) and H₂O(g). *Electrochem. commun.* **50**, 64–68 (2015).
193. Kaczur, J. J., Yang, H., Liu, Z., Sajjad, S. D. & Masel, R. I. Carbon dioxide and water electrolysis using new alkaline stable anion membranes. *Front. Chem.* **6**, 377597 (2018).

194. Endrödi, B. *et al.* Multilayer Electrolyzer Stack Converts Carbon Dioxide to Gas Products at High Pressure with High Efficiency. *ACS Energy Lett.* **4**, 1770–1777 (2019).
195. Wilson, M. S., Valerio, J. A. & Gottesfeld, S. Low platinum loading electrodes for polymer electrolyte fuel cells fabricated using thermoplastic ionomers. *Electrochim. Acta* **40**, 355–363 (1995).
196. Lopes, T., Kim, D. S., Kim, Y. S. & Garzon, F. H. Ionic Transport and Water Vapor Uptake of Ammonium Exchanged Perfluorosulfonic Acid Membranes. *J. Electrochem. Soc.* **159**, B265–B269 (2012).
197. Okada, T., Møller-Holst, S., Gorseth, O. & Kjelstrup, S. Transport and equilibrium properties of Nafion® membranes with H⁺ and Na⁺ ions. *J. Electroanal. Chem.* **442**, 137–145 (1998).
198. Goodwin, J. G., Hongsirikarn, K., Greenway, S. & Creager, S. Effect of cations (Na⁺, Ca²⁺, Fe³⁺) on the conductivity of a Nafion membrane. *J. Power Sources* **195**, 7213–7220 (2010).
199. Reinisch, D. *et al.* Various CO₂-to-CO Electrolyzer Cell and Operation Mode Designs to avoid CO₂-Crossover from Cathode to Anode. *Zeitschrift für Phys. Chemie* **234**, 1115–1131 (2020).
200. Reller, C. *et al.* Selective Electroreduction of CO₂ toward Ethylene on Nano Dendritic Copper Catalysts at High Current Density. *Adv. Energy Mater.* **7**, 1602114 (2017).
201. Huo, Y., Peng, X., Liu, X., Li, H. & Luo, J. High Selectivity Toward C₂H₄ Production over Cu Particles Supported by Butterfly-Wing-Derived Carbon Frameworks. *ACS Appl. Mater. Interfaces* **10**, 12618–12625 (2018).
202. Vichou, E. *et al.* Tuning Selectivity of Acidic Carbon Dioxide Electrolysis via Surface Modification. *Chem. Mater.* **35**, 7060–7068 (2023).
203. Xiong, L. *et al.* Breaking the Linear Scaling Relationship by Compositional and Structural Crafting of Ternary Cu–Au/Ag Nanoframes for Electrocatalytic Ethylene Production. *Angew. Chemie Int. Ed.* **60**, 2508–2518 (2021).
204. Huang, J., Mensi, M., Oveisi, E., Mantella, V. & Buonsanti, R. Structural Sensitivities in Bimetallic Catalysts for Electrochemical CO₂ Reduction Revealed by Ag-Cu Nanodimers. *J. Am. Chem. Soc.* **141**, 2490–2499 (2019).
205. Zhou, Y. *et al.* Dopant-induced electron localization drives CO₂ reduction to C₂ hydrocarbons. *Nat. Chem.* **10**, 974–980 (2018).
206. Jung, H. *et al.* Electrochemical Fragmentation of Cu₂O Nanoparticles Enhancing Selective C-C Coupling from CO₂ Reduction Reaction. *J. Am. Chem. Soc.* **141**, 4624–4633 (2019).
207. Zhong, D. *et al.* Coupling of Cu(100) and (110) Facets Promotes Carbon Dioxide Conversion to Hydrocarbons and Alcohols. *Angew. Chemie* **133**, 4929–4935 (2021).
208. Hori, Y., Takahashi, I., Koga, O. & Hoshi, N. Electrochemical reduction of carbon dioxide at various series of copper single crystal electrodes. *J. Mol. Catal. A Chem.* **199**, 39–47 (2003).
209. Zhang, B. *et al.* Highly Electrocatalytic Ethylene Production from CO₂ on Nanodeficient

- Cu Nanosheets. *J. Am. Chem. Soc.* **142**, 13606–13613 (2020).
210. Nam, D. H. *et al.* Metal-Organic Frameworks Mediate Cu Coordination for Selective CO₂ Electroreduction. *J. Am. Chem. Soc.* **140**, 11378–11386 (2018).
211. Yao, K. *et al.* Metal–organic framework derived copper catalysts for CO₂ to ethylene conversion. *J. Mater. Chem. A* **8**, 11117–11123 (2020).
212. Li, Z. *et al.* Interface-Enhanced Catalytic Selectivity on the C₂Products of CO₂Electroreduction. *ACS Catal.* **11**, 2473–2482 (2021).
213. Liang, H. Q. *et al.* Hydrophobic Copper Interfaces Boost Electroreduction of Carbon Dioxide to Ethylene in Water. *ACS Catal.* **11**, 958–966 (2021).
214. Zhang, J. *et al.* Unveiling the Synergistic Effect between Graphitic Carbon Nitride and Cu₂O toward CO₂ Electroreduction to C₂H₄. *ChemSusChem* **14**, 929–937 (2021).
215. Nam, D. H. *et al.* Molecular enhancement of heterogeneous CO₂ reduction. *Nat. Mater.* **2020** *193* **19**, 266–276 (2020).
216. Wakerley, D. *et al.* Bio-inspired hydrophobicity promotes CO₂ reduction on a Cu surface. *Nat. Mater.* **18**, 1222–1227 (2019).
217. Kim, C. *et al.* Achieving Selective and Efficient Electrocatalytic Activity for CO₂ Reduction Using Immobilized Silver Nanoparticles. *J. Am. Chem. Soc.* **137**, 13844–13850 (2015).
218. Kim, C. *et al.* Insight into Electrochemical CO₂ Reduction on Surface-Molecule-Mediated Ag Nanoparticles. *ACS Catal.* **7**, 779–785 (2017).
219. Zhao, Y., Wang, C., Liu, Y., MacFarlane, D. R. & Wallace, G. G. Engineering Surface Amine Modifiers of Ultrasmall Gold Nanoparticles Supported on Reduced Graphene Oxide for Improved Electrochemical CO₂ Reduction. *Adv. Energy Mater.* **8**, 1801400 (2018).
220. Thevenon, A., Rosas-Hernández, A., Fontani Herreros, A. M., Agapie, T. & Peters, J. C. Dramatic HER Suppression on Ag Electrodes via Molecular Films for Highly Selective CO₂to CO Reduction. *ACS Catal.* **11**, 4530–4537 (2021).
221. Li, F. *et al.* Molecular tuning of CO₂-to-ethylene conversion. *Nat.* **2019** *5777791* **577**, 509–513 (2019).
222. Han, Z., Kortlever, R., Chen, H. Y., Peters, J. C. & Agapie, T. CO₂ Reduction Selective for C₂ Products on Polycrystalline Copper with N-Substituted Pyridinium Additives. *ACS Cent. Sci.* **3**, 853–859 (2017).
223. Cao, Z. *et al.* Chelating N-Heterocyclic Carbene Ligands Enable Tuning of Electrocatalytic CO₂ Reduction to Formate and Carbon Monoxide: Surface Organometallic Chemistry. *Angew. Chemie Int. Ed.* **57**, 4981–4985 (2018).
224. Mun, Y. *et al.* A novel strategy to develop non-noble metal catalyst for CO₂ electroreduction: Hybridization of metal-organic polymer. *Appl. Catal. B Environ.* **236**, 154–161 (2018).
225. Armand, M., Endres, F., MacFarlane, D. R., Ohno, H. & Scrosati, B. Ionic-liquid materials for the electrochemical challenges of the future. *Nat. Mater.* **2009** *88* **8**, 621–

- 629 (2009).
226. Hanc-Scherer, F. A., Montiel, M. A., Montiel, V., Herrero, E. & Sánchez-Sánchez, C. M. Surface structured platinum electrodes for the electrochemical reduction of carbon dioxide in imidazolium based ionic liquids. *Phys. Chem. Chem. Phys.* **17**, 23909–23916 (2015).
227. Rosen, B. A. *et al.* Ionic liquid-mediated selective conversion of CO₂ to CO at low overpotentials. *Science (80-.)*. **334**, 643–644 (2011).
228. Zhao, S. F., Horne, M., Bond, A. M. & Zhang, J. Is the Imidazolium Cation a Unique Promoter for Electrocatalytic Reduction of Carbon Dioxide? *J. Phys. Chem. C* **120**, 23989–24001 (2016).
229. Lau, G. P. S. *et al.* New Insights into the Role of Imidazolium-Based Promoters for the Electroreduction of CO₂ on a Silver Electrode. *J. Am. Chem. Soc.* **138**, 7820–7823 (2016).
230. Koshy, D. M. *et al.* Chemical Modifications of Ag Catalyst Surfaces with Imidazolium Ionomers Modulate H₂Evolution Rates during Electrochemical CO₂Reduction. *J. Am. Chem. Soc.* **143**, 14712–14725 (2021).
231. Iijima, G. *et al.* CO₂ Reduction Promoted by Imidazole Supported on a Phosphonium-Type Ionic-Liquid-Modified Au Electrode at a Low Overpotential. *ACS Catal.* **8**, 1990–2000 (2018).
232. Neyrizi, S., Kiewiet, J., Hempenius, M. A. & Mul, G. What It Takes for Imidazolium Cations to Promote Electrochemical Reduction of CO₂. *ACS Energy Lett.* **7**, 3439–3446 (2022).
233. Fontaine, O., Ghilane, J., Martin, P., Lacroix, J. C. & Randriamahazaka, H. Ionic liquid viscosity effects on the functionalization of electrode material through the electroreduction of diazonium. *Langmuir* **26**, 18542–18549 (2010).
234. Chi, Y. S. *et al.* Anion exchange-promoted Ru^{3+/2+} redox switch in self-assembled monolayers of imidazolium ions on a gold electrode. *Langmuir* **21**, 4268–4271 (2005).
235. Bouden, S., Gómez-Mingot, M., Randriamahazaka, H. & Ghilane, J. Surface Initiated Immobilization of Molecules Contained in an Ionic Liquid Framework. *Anal. Chem.* **88**, 1017–1021 (2016).
236. Cheng, B. *et al.* Selective CO₂Reduction to Ethylene Using Imidazolium-Functionalized Copper. *ACS Appl. Mater. Interfaces* **14**, 27823–27832 (2022).
237. Sha, Y. *et al.* Anchoring Ionic Liquid in Copper Electrocatalyst for Improving CO₂ Conversion to Ethylene. *Angew. Chemie Int. Ed.* **61**, e202200039 (2022).
238. Li, X. Q. *et al.* Regulating electrochemical CO₂RR selectivity at industrial current densities by structuring copper@poly(ionic liquid) interface. *Appl. Catal. B Environ.* **297**, 120471 (2021).
239. Duan, G. Y. *et al.* Highly Efficient Electrocatalytic CO₂ Reduction to C₂+ Products on a Poly(ionic liquid)-Based Cu⁰–Cu^I Tandem Catalyst. *Angew. Chemie Int. Ed.* **61**, e202110657 (2022).
240. Nie, W., Heim, G. P., Watkins, N. B., Agapie, T. & Peters, J. C. Organic Additive-derived

- Films on Cu Electrodes Promote Electrochemical CO₂ Reduction to C₂+ Products Under Strongly Acidic Conditions. *Angew. Chemie Int. Ed.* **62**, e202216102 (2023).
241. Fan, M. *et al.* Cationic-group-functionalized electrocatalysts enable stable acidic CO₂ electrolysis. *Nat. Catal.* **2023** 1–10 (2023) doi:10.1038/s41929-023-01003-5.
242. Wang, Y. *et al.* A reduced imidazolium cation layer serves as the active site for electrochemical carbon dioxide reduction. *Appl. Catal. B Environ.* **264**, 118495 (2020).
243. Michez, R., Doneux, T., Buess-Herman, C. & Luhmer, M. NMR Study of the Reductive Decomposition of [BMIm][NTf₂] at Gold Electrodes and Indirect Electrochemical Conversion of CO₂. *ChemPhysChem* **18**, 2208–2216 (2017).
244. Michez, R., Vander Steen, J., Doneux, T., Luhmer, M. & Buess-Herman, C. Electroreduction of 1-butyl-3-methylimidazolium bis(trifluoromethanesulfonyl)imide ionic liquid: Oriented product selectivity through the electrode material. *Electrochim. Acta* **270**, 434–439 (2018).
245. Lane, G. H. Electrochemical reduction mechanisms and stabilities of some cation types used in ionic liquids and other organic salts. *Electrochim. Acta* **83**, 513–528 (2012).
246. Niu, D., Wang, H., Li, H., Wu, Z. & Zhang, X. Roles of ion pairing on electroreduction of carbon dioxide based on imidazolium-based salts. *Electrochim. Acta* **158**, 138–142 (2015).
247. Qin, H. G. *et al.* Quantitative Understanding of Cation Effects on the Electrochemical Reduction of CO₂ and H⁺ in Acidic Solution. *ACS Catal.* **13**, 916–926 (2023).
248. Fonder, G., Laffineur, F., Delhalle, J. & Mekhalif, Z. Alkanethiol-oxidized copper interface: The critical influence of concentration. *J. Colloid Interface Sci.* **326**, 333–338 (2008).
249. Whelan, C. M., Kinsella, M., Carbonell, L., Ho, H. M. & Maex, K. Corrosion inhibition by self-assembled monolayers for enhanced wire bonding on Cu surfaces. *Microelectron. Eng.* **70**, 551–557 (2003).
250. Sung, M. M., Sung, K., Kim, C. G., Lee, S. S. & Kim, Y. Self-Assembled Monolayers of Alkanethiols on Oxidized Copper Surfaces. *J. Phys. Chem. B* **104**, 2273–2277 (2000).
251. Fonder, G., Volcke, C., Csoka, B., Delhalle, J. & Mekhalif, Z. Electrochemical and spectroscopic study of C₁₂H₂₅X molecules adsorption on copper sheets, X (–SH, –S–S–, –SeH and –Se–Se–). *Electrochim. Acta* **55**, 1557–1567 (2010).
252. Fonder, G., Delhalle, J. & Mekhalif, Z. Exchange versus intercalation of n-dodecanethiol monolayers on copper in the presence of n-dodecaneselenol and vice versa. *Appl. Surf. Sci.* **256**, 2968–2973 (2010).
253. Hoque, E., DeRose, J. A., Bhushan, B. & Hipps, K. W. Low adhesion, non-wetting phosphonate self-assembled monolayer films formed on copper oxide surfaces. *Ultramicroscopy* **109**, 1015–1022 (2009).
254. Keszthelyi, T. *et al.* Investigation of solid surfaces modified by Langmuir-Blodgett monolayers using sum-frequency vibrational spectroscopy and X-ray photoelectron spectroscopy. *J. Phys. Chem. B* **110**, 8701–8714 (2006).
255. Ohta, K. Prediction of pKa Values of Alkylphosphonic Acids.

- <https://doi.org/10.1246/bcsj.65.2543> **65**, 2543–2545 (2006).
256. Fonder, G. *et al.* Anchoring of alkylphosphonic derivatives molecules on copper oxide surfaces. *Appl. Surf. Sci.* **257**, 6300–6307 (2011).
 257. Kim, D. *et al.* Selective CO₂ electrocatalysis at the pseudocapacitive nanoparticle/ordered-ligand interlayer. *Nat. Energy* **2020 512 5**, 1032–1042 (2020).
 258. Yu, S. *et al.* Nanoparticle Assembly Induced Ligand Interactions for Enhanced Electrocatalytic CO₂ Conversion. *J. Am. Chem. Soc.* **143**, 19919–19927 (2021).
 259. Cheng, H. *et al.* Construction of atomically dispersed Cu-N₄ sites via engineered coordination environment for high-efficient CO₂ electroreduction. *Chem. Eng. J.* **407**, 126842 (2021).
 260. Yang, G., Yu, J., Peng, S., Sheng, K. & Zhang, H. Poly(ionic liquid)-Modified Metal Organic Framework for Carbon Dioxide Adsorption. *Polym. 2020, Vol. 12, Page 370* **12**, 370 (2020).
 261. Li, Z. *et al.* Constructing efficient ion nanochannels in alkaline anion exchange membranes by the in situ assembly of a poly(ionic liquid) in metal–organic frameworks. *J. Mater. Chem. A* **4**, 2340–2348 (2016).
 262. Katsyuba, S. A., Dyson, P. J., Vandyukova, E. E., Chernova, A. V. & Vidiš, A. Molecular Structure, Vibrational Spectra, and Hydrogen Bonding of the Ionic Liquid 1-Ethyl-3-methyl-1H-imidazolium Tetrafluoroborate. *Helv. Chim. Acta* **87**, 2556–2565 (2004).
 263. Papisizza, M. & Cuesta, A. In Situ Monitoring Using ATR-SEIRAS of the Electrocatalytic Reduction of CO₂ on Au in an Ionic Liquid/Water Mixture. *ACS Catal.* **8**, 6345–6352 (2018).
 264. Romann, T., Oll, O., Pikma, P., Tamme, H. & Lust, E. Surface chemistry of carbon electrodes in 1-ethyl-3-methylimidazolium tetrafluoroborate ionic liquid – an in situ infrared study. *Electrochim. Acta* **125**, 183–190 (2014).
 265. Wang, J. *et al.* Selective CO₂ electrochemical reduction enabled by a tricomponent copolymer modifier on a copper surface. *J. Am. Chem. Soc.* **143**, 2857–2865 (2021).
 266. Lai, Y. *et al.* Breaking Scaling Relationships in CO₂ Reduction on Copper Alloys with Organic Additives. *ACS Cent. Sci.* **7**, 1756–1762 (2021).
 267. Perkins, C. L. Molecular anchors for self-assembled monolayers on ZnO: A direct comparison of the thiol and phosphonic acid moieties. *J. Phys. Chem. C* **113**, 18276–18286 (2009).
 268. Monroe, M. M., Lobaccaro, P., Lum, Y. & Ager, J. W. Membraneless laminar flow cell for electrocatalytic CO₂ reduction with liquid product separation. *J. Phys. D. Appl. Phys.* **50**, 154006 (2017).
 269. Pei, Y., Pi, Z., Zhong, H., Cheng, J. & Jin, F. Glycerol oxidation-assisted electrochemical CO₂ reduction for the dual production of formate. *J. Mater. Chem. A* **10**, 1309–1319 (2022).
 270. Vos, J. G. *et al.* Selectivity Trends between Oxygen Evolution and Chlorine Evolution on Iridium-Based Double Perovskites in Acidic Media. *ACS Catal.* **9**, 8561–8574 (2019).

271. Watkins, N. B., Wu, Y., Nie, W., Peters, J. C. & Agapie, T. In Situ Deposited Polyaromatic Layer Generates Robust Copper Catalyst for Selective Electrochemical CO₂ Reduction at Variable pH. *ACS Energy Lett.* **8**, 189–195 (2023).
272. Kozhushkov, S. I. & Alcarazo, M. Synthetic Applications of Sulfonium Salts. *Eur. J. Inorg. Chem.* **2020**, 2486–2500 (2020).
273. Quan, F., Xiong, M., Jia, F. & Zhang, L. Efficient electroreduction of CO₂ on bulk silver electrode in aqueous solution via the inhibition of hydrogen evolution. *Appl. Surf. Sci.* **399**, 48–54 (2017).
274. Chen, L. *et al.* Electrochemical Reduction of Carbon Dioxide in a Monoethanolamine Capture Medium. *ChemSusChem* **10**, 4109–4118 (2017).
275. Niu, Z. Z., Chi, L. P., Liu, R., Chen, Z. & Gao, M. R. Rigorous assessment of CO₂ electroreduction products in a flow cell. *Energy Environ. Sci.* **14**, 4169–4176 (2021).
276. Xie, Y. *et al.* High carbon utilization in CO₂ reduction to multi-carbon products in acidic media. *Nat. Catal.* **2022** *56* **5**, 564–570 (2022).
277. Clark, E. L. *et al.* Standards and Protocols for Data Acquisition and Reporting for Studies of the Electrochemical Reduction of Carbon Dioxide. *ACS Catal.* **8**, 6560–6570 (2018).
278. Weisenberger, S. & Schumpe, A. Estimation of gas solubilities in salt solutions at temperatures from 273 K to 363 K. *AIChE J.* **42**, 298–300 (1996).

Appendix

Table A.1 Complete reaction equations for a device in which CO₂R is coupled with OER. The cell potential values ($|E^{\circ}_{\text{cell}}|$) of the complete reaction are calculated with the following equation: $|E^{\circ}_{\text{cell}}| = |E_{\text{CO}_2\text{R}} - E_{\text{OER}}|$.

Reaction	$ E^{\circ}_{\text{cell}} / \text{V}$
$2\text{CO}_2 \rightarrow 2\text{CO} + \text{O}_2$	1.33
$2\text{CO}_2 + 2\text{H}_2\text{O} \rightarrow 2\text{HCOOH} + \text{O}_2$	1.35
$2\text{CO}_2 + 4\text{H}_2\text{O} \rightarrow 2\text{CH}_3\text{OH} + 3\text{O}_2$	1.20
$\text{CO}_2 + 2\text{H}_2\text{O} \rightarrow \text{CH}_4 + 2\text{O}_2$	1.06
$2\text{CO}_2 + 2\text{H}_2\text{O} \rightarrow \text{C}_2\text{H}_4 + 3\text{O}_2$	1.15
$2\text{CO}_2 + 3\text{H}_2\text{O} \rightarrow \text{C}_2\text{H}_5\text{OH} + 3\text{O}_2$	1.14
$6\text{CO}_2 + 8\text{H}_2\text{O} \rightarrow 2\text{C}_3\text{H}_7\text{OH} + 9\text{O}_2$	1.13

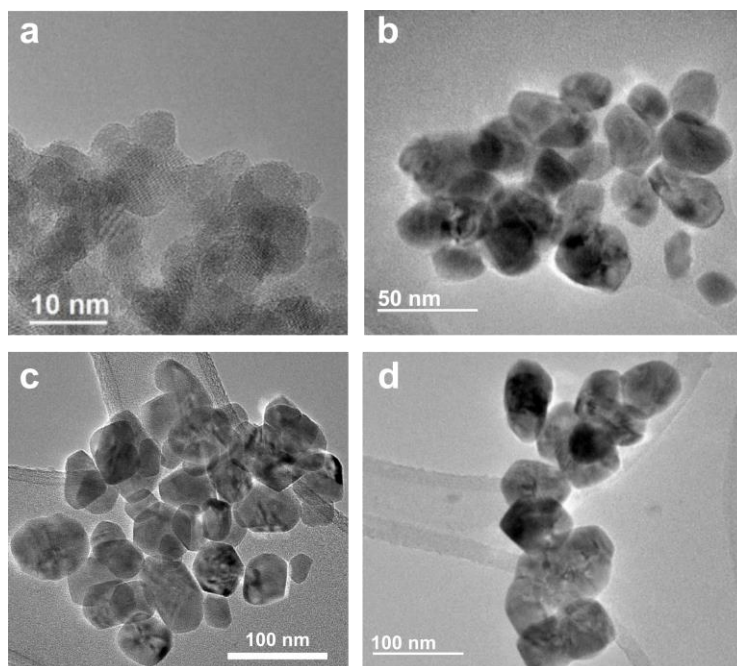


Figure A.1 TEM images of the CuO NPs synthesized at different temperatures. (a) 150 °C, 10 nm; (b) 180 °C, 35 nm; (c) 200 °C, 50 nm; (d) 210 °C, 80 nm.

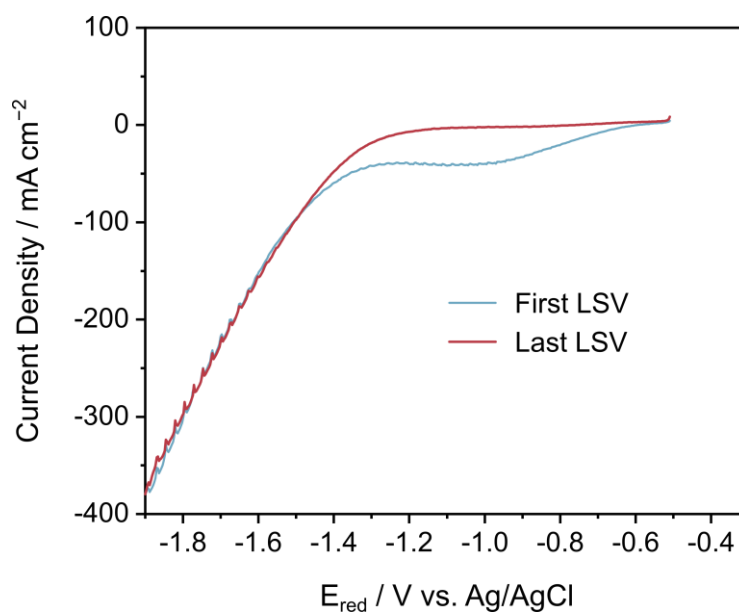


Figure A.2 Activation LSVs to obtain metallic Cu.

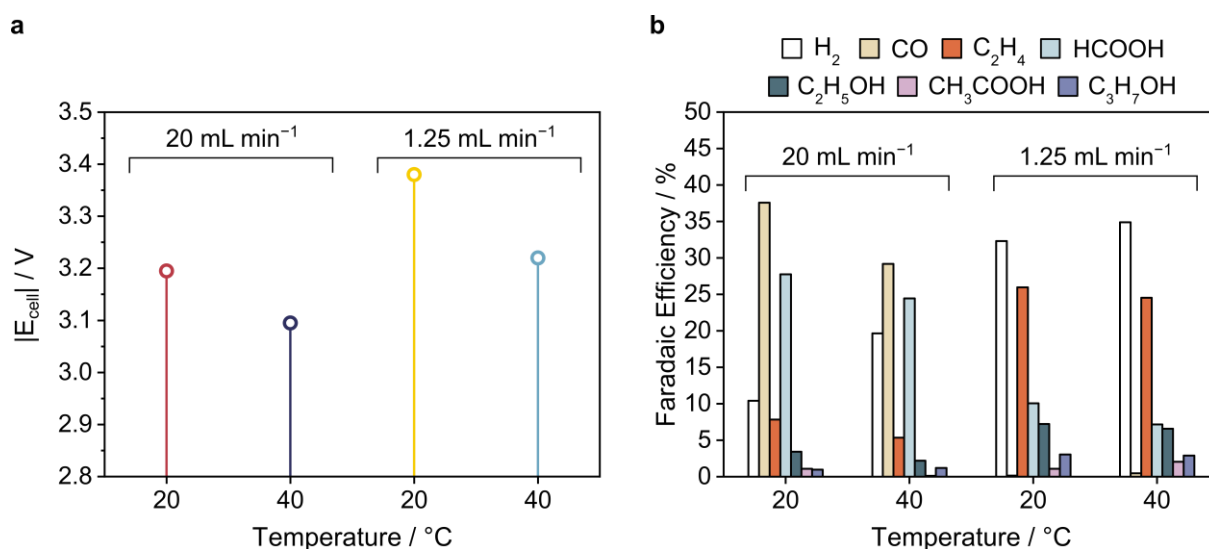


Figure A.3 CO₂ feed low rate and temperature influence on potential (a) and product selectivity (b). The electrolysis were carried out for 30 min each at -200 mA cm^{-2} in a 3 M Cs₂SO₄ solution (pH 5) and a C | 1 | DIA | A configuration. Lowering the feed flow rate of CO₂ increases the selectivity for multicarbon products.

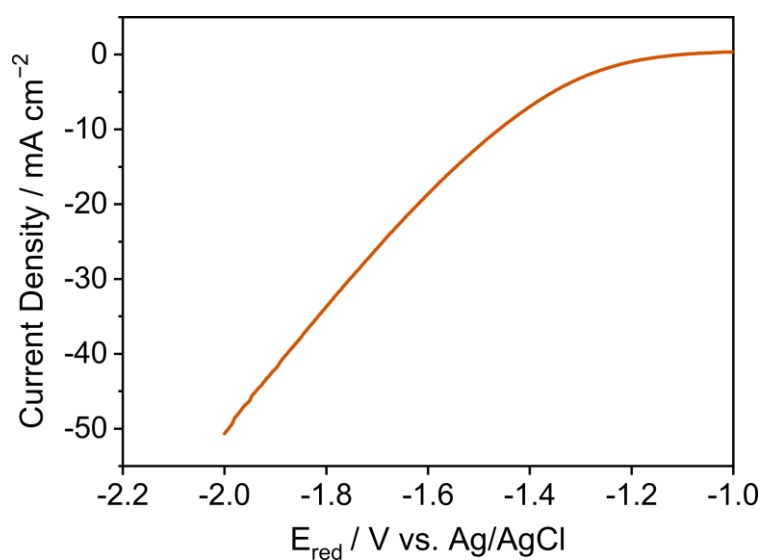


Figure A.4 LSV scan of a 0.5 M EMIMBF₄ solution under inert atmosphere with a glassy carbon electrode. Scan rate: 100 mV s^{-1} .

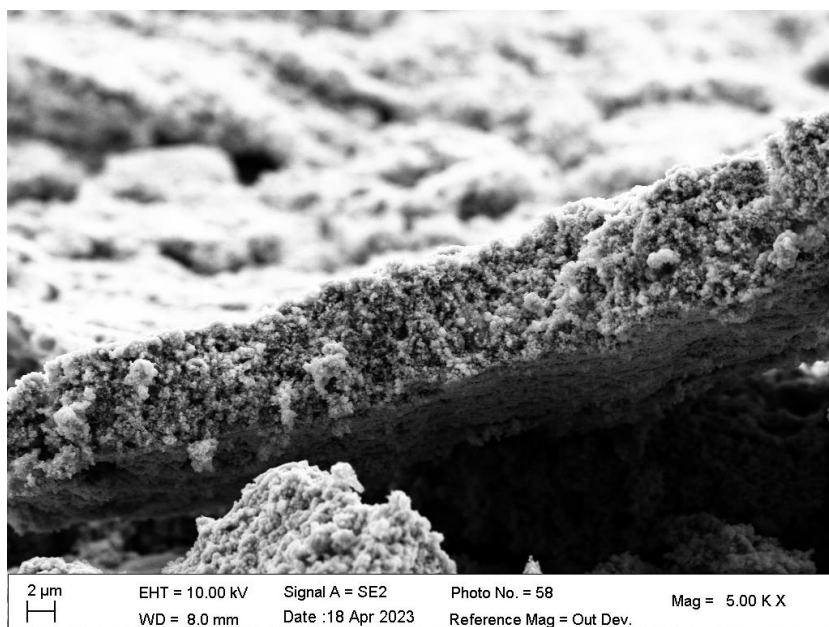


Figure A.5 Cross section of the IL-coated Cu NPs layer.